

ผลของการโดปโลหะบน La_2NiO_4 เพื่อเป็นแคโทดสำหรับเซลล์เชื้อเพลิงออกไซด์ของแข็ง

นางสาวรัตนากร อีร์ศรัณยานนท์



วิทยานิพนธ์นี้เป็นส่วนหนึ่งของการศึกษาตามหลักสูตรปริญญาวิทยาศาสตรมหาบัณฑิต

สาขาวิชาเคมี ภาควิชาเคมี

คณะวิทยาศาสตร์ จุฬาลงกรณ์มหาวิทยาลัย

ปีการศึกษา 2556

ลิขสิทธิ์ของจุฬาลงกรณ์มหาวิทยาลัย



5472076323

EFFECTS OF METAL DOPING ON La_2NiO_4 AS CATHODE FOR SOLID OXIDE FUEL CELL

Miss Ratanakorn Teerasarunyanon



A Thesis Submitted in Partial Fulfillment of the Requirements
for the Degree of Master of Science Program in Chemistry

Department of Chemistry

Faculty of Science

Chulalongkorn University

Academic Year 2013

Copyright of Chulalongkorn University

Thesis Title	EFFECTS OF METAL DOPING ON La_2NiO_4 AS CATHODE FOR SOLID OXIDE FUEL CELL
By	Miss Ratanakorn Teerasarunyanon
Field of Study	Chemistry
Thesis Advisor	Assistant Professor Soamwadee Chaianansutcharit, Ph.D.

Accepted by the Faculty of Science, Chulalongkorn University in Partial
Fulfillment of the Requirements for the Master's Degree

.....Dean of the Faculty of Science
(Professor Supot Hannongbua, Dr.rer.nat.)

THESIS COMMITTEE

.....Chairman
(Assistant Professor Warinthorn Chavasiri, Ph.D.)

.....Thesis Advisor
(Assistant Professor Soamwadee Chaianansutcharit, Ph.D.)

.....Examiner
(Assistant Professor Boosayarat Tompatanaget, Ph.D.)

.....External Examiner
(Tanawat Kanjanaboonmalert, Ph.D.)



รัตนากร จีรศรัณยานนท์ : ผลของการโดปโลหะบน La_2NiO_4 เพื่อเป็นแคโทดสำหรับ เซลล์เชื้อเพลิงออกไซด์ของแข็ง. (EFFECTS OF METAL DOPING ON La_2NiO_4 AS CATHODE FOR SOLID OXIDE FUEL CELL) อ.ที่ปรึกษาวิทยานิพนธ์หลัก: ผศ. ดร. โสภมาดี ไชยอนันต์สุจริต , 7' หน้า.

ศึกษาสมบัติของวัสดุสำหรับใช้เป็นแคโทดในเซลล์เชื้อเพลิงออกไซด์ของแข็ง $(\text{La}_{0.8}\text{Sr}_{0.2})_{2-x}\text{Ca}_x\text{NiO}_4$ (LSN- Ca_x), $(\text{La}_{0.8}\text{Sr}_{0.2})_{2-x}\text{Ca}_x\text{Ni}_{0.9}\text{Co}_{0.1}\text{O}_4$ (LSNC- Ca_x) และ $\text{La}_{2-x}\text{Ca}_x\text{Ni}_{0.9-k}\text{Co}_{0.1}(\text{Fe,Zn})_y\text{O}_4$ (LNCf- Ca_x and LNCZ- Ca_x) แสดงโครงสร้าง K_2NiF_4 แบบเตตระโกนัล และสามารถสังเคราะห์ได้จากวิธีซิงเทรตประยุกต์โดยการเผาและซินเทอร์ที่อุณหภูมิ 950 และ 1350 องศาเซลเซียสเป็นเวลา 10 ชั่วโมงตามลำดับ LSN- Ca_x and LSNC- Ca_x ($x=0-0.5$) ที่มีการแทนที่ไอออนตำแหน่ง A ด้วยไอออน Ca^{2+} สัดส่วน $x=0.2$ แสดงโครงสร้างเฟสเดียวและให้ค่าการนำไฟฟ้าสูงสุด คือ 176.9 และ 166.9 ซีเมนส์ต่อเซนติเมตรที่อุณหภูมิ 800 องศาเซลเซียสตามลำดับ พัฒนาการซึมผ่านออกซิเจนของ $\text{La}_2\text{Ni}_{0.9}\text{Co}_{0.1}\text{O}_4$ (LNC) โดยแทนที่นิกเกิลด้วยไอออน Fe^{3+} และ Zn^{2+} ได้เป็น LNC- Fe_y และ LNC- Zn_y ($y=0-0.2$) จากนั้นทำการเติมไอออน Ca^{2+} ที่ตำแหน่งแลนทานัมใน LNC- $\text{Fe}_{0.05}$ และ LNC- $\text{Zn}_{0.05}$ ที่มีค่าการซึมผ่านออกซิเจนสูงที่สุดของแต่ละระบบเพื่อเพิ่มค่าการนำไฟฟ้า พบว่า LNCf- $\text{Ca}_{0.5}$ และ LNCZ- $\text{Ca}_{0.5}$ ให้ค่าการนำไฟฟ้าสูงสุดคือ 98.4 และ 84.9 ซีเมนส์ต่อเซนติเมตรที่ 800 องศาเซลเซียสตามลำดับ นอกจากนี้ได้ทำการวัดประสิทธิภาพเซลล์เดี่ยวของ LNCf- $\text{Ca}_{0.5}$ และ LNCZ- $\text{Ca}_{0.5}$ กับอิเล็กโทรไลต์ LSGM พบว่าให้ค่ากำลังไฟฟ้าสูงสุดที่ 322 และ 312 มิลลิวัตต์ต่อตารางเซนติเมตรที่อุณหภูมิ 800 องศาเซลเซียสตามลำดับ สามารถนำไปประยุกต์ใช้ในเซลล์เชื้อเพลิงออกไซด์ของแข็งที่อุณหภูมิปานกลางได้



391.4990606

ภาควิชา เคมี

ลายมือชื่อนิสิต

สาขาวิชา เคมี

ลายมือชื่อ อ.ที่ปรึกษาวิทยานิพนธ์หลัก

ปีการศึกษา 2556

5472076323 : MAJOR CHEMISTRY

KEYWORDS: SOLID OXIDE FUEL CELL / CATHODE MATERIAL / ELECTRICAL
CONDUCTIVITY / PEROVSKITE

RATANAKORN TEERASARUNYANON: EFFECTS OF METAL DOPING ON
 La_2NiO_4 AS CATHODE FOR SOLID OXIDE FUEL CELL. ADVISOR: ASST. PROF.
SOAMWADEE CHAIANANSUTCHARIT, Ph.D., 7¹ pp.

The properties of $(\text{La}_{0.8}\text{Sr}_{0.2})_{2-x}\text{Ca}_x\text{NiO}_4$ (LSN- Ca_x), $(\text{La}_{0.8}\text{Sr}_{0.2})_{2-x}\text{Ca}_x\text{Ni}_{0.9}\text{Co}_{0.1}\text{O}_4$ (LSNC- Ca_x) and $\text{La}_{2-x}\text{Ca}_x\text{Ni}_{0.9-y}\text{Co}_{0.1}(\text{Fe}, \text{Zn})_y\text{O}_4$ (LNCF- Ca_x and LNCZ- Ca_x) as cathode materials for solid oxide fuel cell were investigated. All compounds prepared by modified citrate method exhibited K_2NiF_4 -type with tetragonal structure using calcination and sintering temperature of 900°C and 1350°C for 10 hours, respectively. LSN- Ca_x and LSNC- Ca_x ($x=0-0.5$) substituted with Ca^{2+} on the A-site in composition of $x=0.2$ showed the single phase of K_2NiF_4 -type structure and the highest electrical conductivity of 176.9 and 166.9 S/cm at 800°C, respectively. To improve oxygen permeation of $\text{La}_2\text{Ni}_{0.9}\text{Co}_{0.1}\text{O}_4$ (LNC), Ni-site was firstly substituted with Fe^{3+} or Zn^{2+} to obtain LNC- Fe_y and LNC- Zn_y ($y=0-0.2$). Then Ca^{2+} was incorporated into La-site of LNC- $\text{Fe}_{0.05}$ and LNC- $\text{Zn}_{0.05}$ which had the highest oxygen permeation rate, to improve the electrical conductivity. The highest electrical conductivity was achieved for LNCF- $\text{Ca}_{0.5}$ and LNCZ- $\text{Ca}_{0.5}$ and the values were 98.4 and 84.9 S/cm at 800°C. Additionally, the single cell performance of LNCF- $\text{Ca}_{0.5}$ and LNCZ- $\text{Ca}_{0.5}$ with LSGM electrolyte was measured and maximum power densities were 322 and 312 mW/cm^2 at 800°C, respectively. This indicated that LNCF- $\text{Ca}_{0.5}$ and LNCZ- $\text{Ca}_{0.5}$ could be potential cathode materials for IT-SOFC.



Department: Chemistry

Student's Signature

Field of Study: Chemistry

Advisor's Signature

Academic Year: 2013

ACKNOWLEDGEMENTS

The author would like to express my sincere gratitude to my advisor, Assistant Professor Dr. Soamwadee Chaianansutcharit for her guidance and encouragement. Without her advice and persistent help, this thesis would not have been possible.

The author would like to thank Assistant Professor Dr. Warinthorn Chavasiri, Assistant Professor Dr. Boosyarat Tomapatanaget, and Dr. Tanawat Kanjanaboonmalert for serving as this thesis committee.

The author gratefully acknowledge Office National Research Council of Thailand (NRCT), Department of chemistry, Faculty of science, Chulalongkorn university and Development and Promotion of Science and Technology Talents Project scholarship for financial and facility supports.

Finally, She would also like to thank her family, all her friends and co-workers for their support and love which helped her achieve her objectives.



CONTENTS

	Page
THAI ABSTRACT	iv
ENGLISH ABSTRACT	v
ACKNOWLEDGEMENTS	vi
CONTENTS	vii
1.1 Fuel Cells.....	1
1.2 Solid Oxide Fuel cells (SOFCs).....	2
1.2.1 Operation of SOFCs.....	2
1.2.2 Materials in SOFCs	3
1.2.2.1 Electrolyte.....	3
1.2.2.2 Anode.....	4
1.2.2.3 Cathode	5
1.3 Perovskite	7
1.4 Electrical conductivity.....	10
1.5 Current-Voltage characterization	12
1.7 Literature reviews	14
1.8 The objectives of this thesis.....	17
2.1 Chemicals	18
2.2 Material preparation.....	19
2.2.1 Cathode preparation.....	19
2.2.2 Anode preparation.....	21
2.2.3 Electrolyte preparation.....	21
2.3 Material characterization.....	22
2.3.1 X-ray diffractometry (XRD).....	22
2.3.2 Scanning electron microscopy (SEM).....	22
2.3.3 Density	22
2.3.4 Electrical conductivity measurement.....	22
2.3.5 Oxygen permeation measurement	23



3914990606

	Page
2.3.6 Electrochemical measurement.....	24
3.1 Tolerance factor.....	26
3.2 Synthesis and properties of $(La_{0.8}Sr_{0.2})_{2-x}Ca_xNiO_4$ (LSN- Ca_x).....	27
3.2.1 XRD analyses.....	27
3.2.2 SEM analyses	29
3.2.3 Electrical conductivity analyses.....	30
3.3 Synthesis and properties of $(La_{0.8}Sr_{0.2})_{2-x}Ca_xNi_{0.9}Co_{0.1}O_4$ (LSNC- Ca_x)	33
3.3.1 XRD analyses.....	33
3.3.2 SEM analyses	35
3.3.3 Electrical conductivity analyses.....	35
3.4 Synthesis and properties of $La_2Ni_{0.9-y}Co_{0.1}M_yO_4$ (M=Fe, Zn and $y=0-0.2$)	38
3.4.1 XRD analyses.....	38
3.4.2 SEM analyses	41
3.4.3 Oxygen permeation analyses	42
3.5 Synthesis and properties of $La_{2-x}Ca_xNi_{0.85}Co_{0.1}M_{0.05}O_4$ (M=Fe, Zn and $x=0-0.7$)... 45	45
3.5.1 XRD analyses.....	45
3.5.2 SEM analyses	48
3.5.3 Electrical conductivity analyses.....	49
3.6 Electrochemical analyses.....	51
3.6.1 Material compatibility	51
3.6.2 Impedance and single cell performance analyses	55
4.1 Conclusion.....	59
4.2 Suggestions.....	60
REFERENCES	61
APPENDICES.....	66
APPENDIX A.....	67
APPENDIX B.....	68



APPENDIX C.....	69
VITA.....	75



LIST OF FIGURES

Figure 1.1 SOFC operation scheme	2
Figure 1.2 Conductivity of YSZ, GDC and LSGM	4
Figure 1.3 Active areas for oxygen reduction reaction	6
Figure 1.4 The perovskite structure (ABX_3)	8
Figure 1.5 The A_2BO_4 structure showing the location of an interstitial oxygen atom ...	9
Figure 1.6 Derivation of the tolerance factor	10
Figure 1.7 Covalent bonds between anionic p orbital and t_{2g} orbital of B-site cation	11
Figure 1.8 The migration of the oxygen ion passes through the saddle point	12
Figure 1.9 Characteristics of a typical current-voltage curve in SOFC	13
Figure 1.10 Typical power/current relation	13
Figure 1.11 Schematic of a Nyquist plot	14
Figure 2.1 KBr die assembly.....	21
Figure 2.2 schematic diagram of specimen with four platinum (Pt) wire contacts.....	23
Figure 2.3 Cross-sectional view of the membrane reactor	24
Figure 2.4 Schematic configuration of the single cell performance test set-up	25
Figure 3.1 XRD patterns of LSN- Ca_x discs	28
Figure 3.2 SEM images of LSN- Ca_x discs.....	29
Figure 3.3 Temperature dependence of the specific conductivity of LSN- Ca_x	30
Figure 3.4 Arrhenius plot of the electrical conductivity of LSN- Ca_x	32
Figure 3.5 XRD patterns of LSNC- Ca_x discs.....	34
Figure 3.6 SEM images of LSNC- Ca_x discs.....	35
Figure 3.7 Temperature dependence of the specific conductivity of LSNC- Ca_x	36
Figure 3.8 Arrhenius plot of the electrical conductivity of LSNC- Ca_x	38
Figure 3.9 XRD patterns of LNC- Fe_y discs	39
Figure 3.10 XRD patterns of LNC- Zn_y discs	40
Figure 3.11 SEM images of LNC- Fe_y and LNC- Zn_y discs	41
Figure 3.12 Temperature dependence of oxygen permeation for LNC- Fe_y	42
Figure 3.13 Temperature dependence of oxygen permeation for LNC- Zn_y	43
Figure 3.14 Oxygen migration path in the a-b plane and c direction.....	44
Figure 3.15 XRD patterns of LNCF- Ca_x discs.....	46



Figure 3.16 XRD patterns of LNCZ-Ca _x discs.....	47
Figure 3.17 SEM images of LNCF-Ca _x and LNCZ-Ca _x discs.....	48
Figure 3.18 Temperature dependence of the specific conductivity of LNCF-Ca _x	49
Figure 3.19 Temperature dependence of the specific conductivity of LNCZ-Ca _x	50
Figure 3.20 XRD patterns of LNCF-Ca _{0.5} -LSGM and LNCZ-Ca _{0.5} -LSGM mixtures after fired at 1000°C for 10 hours.....	52
Figure 3.21 XRD patterns of LSN-Ca _{0.2} -LSGM and LSNC-Ca _{0.2} -LSGM mixtures after fired at 1000°C for 10 hours.....	53
Figure 3.22 XRD patterns of LSN-Ca _{0.2} -LSGM and LSNC-Ca _{0.2} -LSGM mixtures after fired at 950°C for 10 hours.....	54
Figure 3.23 XRD patterns of LSN-Ca _{0.2} -LSGM and LSNC-Ca _{0.2} -LSGM mixtures after fired at 900°C for 10 hours.....	55
Figure 3.24 The AC impedance spectra of LNCF-Ca _{0.5} /LSGM/Ni-Fe and LNCZ-Ca _{0.5} / LSGM/Ni-Fe.....	56
Figure 3.25 I-V curves and corresponding power density curves of LNCF-Ca _{0.5} / LSGM/Ni-Fe and LNCZ-Ca _{0.5} /LSGM/Ni-Fe.....	56



LIST OF TABLES

Table 1.1 Types of fuel cells	1
Table 1.2 Thermal expansion coefficients of various electrolytes	4
Table 1.3 Micro-structural and property of SOFC component	7
Table 2.1 Chemicals and reagents for synthesis of materials	18
Table 2.2 The composition of all prepared cathodes	19
Table 3.1 The tolerance factors of all prepared oxides.....	26
Table 3.2 Lattice parameter and unit cell volume of LSN-Ca _x	29
Table 3.3 Average grain size and relative density of LSN-Ca _x discs	30
Table 3.4 The specific conductivity of LSN-Ca _x	32
Table 3.5 Activation energy (E_a) of LSN-Ca _x at 300-800°C.....	33
Table 3.6 Lattice parameter and unit cell volume of LSNC-Ca _x	34
Table 3.7 Average grain size and relative density of LSNC-Ca _x discs.....	35
Table 3.8 The specific conductivity of LSNC-Ca _x	37
Table 3. 9 Activation energy (E_a) of LSNC-Ca _x at 300-800°C.....	37
Table 3.10 Lattice parameters and unit cell volume of LNC-Fe _y	39
Table 3.11 Lattice parameters and unit cell volume of LNC-Zn _y	40
Table 3.12 Average grain size and relative density of LNC-Fe _y and LNC-Zn _y , discs.....	42
Table 3.13 Lattice parameters and unit cell volume of LNCF-Ca _x	46
Table 3.14 Lattice parameters and unit cell volume of LNCZ-Ca _x	47
Table 3.15 Average grain size and relative density of LNCF-Ca _x and LNCZ-Ca _x discs ..	49
Table 3.16 The specific conductivity of LNCF-Ca _x	50
Table 3.17 The specific conductivity of LNCZ-Ca _x	50
Table 3.18 Polarization resistance and power density of LNCF-Ca _{0.5} /LSGM/Ni-Fe and LNCZ-Ca _{0.5} /LSGM/Ni-Fe	57



LIST OF ABBREVIATIONS

SOFCs	Solid oxide fuel cells
AFC	Alkaline fuel cell
PMEFC	Polymer electrolyte membrane fuel cell
PAFC	Phosphoric acid fuel cell
MCFC	Molten carbonate fuel cell
XRD	X-ray diffractometry
SEM	Scanning electron microscopy
T	temperature
°C	degree Celsius
K	Kelvin
g	gram
mm	millimeter
cm	centimeter
μm	micrometer
Å	angstrom
σ	specific conductivity
E_a	activation energy
%	percent
a, c	unit lattice parameter
t	tolerance factor
r	ionic radius
L	length
I	current
T	thickness
V	voltage
W	width
P	power density
R	resistance
Z	impedance



3914990606

CHAPTER I

INTRODUCTION

Because of the non-renewable nature of petroleum-based energy resources, their increasing demand has never met the realistic supply and tends to outrun the resource itself. Accompanied with the rise in greenhouse emissions caused by the combustion processes, the global warming is getting more serious. Therefore the new environmentally-friendly energy resources have been receiving much attention in order to reduce the global problems, and fuel cells turn out to be a promising solution.

1.1 Fuel Cells

Fuel cells are a device generating electricity with cleanest and high efficiency. Since there is no combustion during the operation, there are none of the pollutants. For systems planned to use hydrogen directly, they produce only electricity, water and heat.

The most common classification of fuel cells is by the type of electrolyte used in the cells. The five major types of fuel cells are alkaline fuel cell (AFC), polymer electrolyte membrane fuel cell (PEMFC), phosphoric acid fuel cell (PAFC), molten carbonate fuel cell (MCFC), and solid oxide fuel cell (SOFC). Table 1.1 provides a comparison between various fuel cells.

Table 1.1 Types of fuel cells [1]

Type	AFC	PEMFC	PAFC	MCFC	SOFC
Electrolyte	Alkaline solution	Polymer	Phosphoric acid	Molten carbonate	Oxide
Charge carrier	OH^-	H^+	H^+	CO_3^-	O^{2-}
Operating Temp. (°C)	70-90	70-200	180-200	650-700	800-1000
Fuel	H_2	H_2	H_2	H_2, CO	Hydrocarbon, H_2, CO
Efficiency (%)	30	40-50	40-50	50-60	50-60



1.2 Solid Oxide Fuel cells (SOFCs)

SOFCs are devices that electrochemically convert chemical energy into electrical energy directly without the need of combustion. They are all-solid-state system and high operating temperatures (up to 1000°C). The major advantage of SOFCs over other fuel cells is the fuel adaptability. SOFCs can be run on a variety of fuels such as hydrogen, natural gas, diesel, gasoline, methane, butane, etc, while other fuel cells operate with pure hydrogen.

1.2.1 Operation of SOFCs

The SOFC single cell is constructed with dense electrolyte which is sandwiched between a porous anode and a porous cathode, as shown in Figure 1.1. During the SOFC operation, fuel is fed to the anode, where an oxidation reaction takes place and releases electrons to the external circuit, whereas oxidant, normally oxygen or air, is fed to the cathode. Considering the electrode reactions, the cathodic reaction is the electrochemical reaction of gaseous oxygen into oxide ion while the dissociation of gaseous H_2 takes place on the anode. The resulting products include water, carbon dioxide, heat and electrons. In order to minimize voltage losses and maximize power densities, kinetics of reaction, ionic and molecular transport must be taken into account.

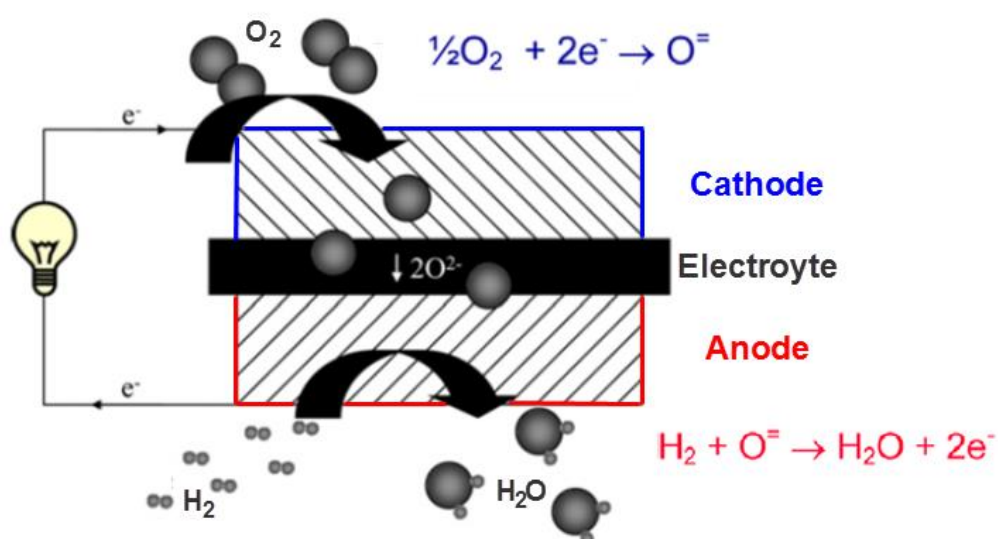


Figure 1.1 SOFC operation scheme [2]

1.2.2 Materials in SOFCs

The problem of SOFC operated at intermediate temperature (600-800°C) is the decline of performance because of low ionic conductivity of electrolyte and strong cathode polarization. To solve this problem, the alternative electrode and electrolyte materials are considerable to be used. Therefore, it is necessary to select materials which have the properties such as conducting property and thermal expansion property for the requirement of each component of SOFC.

1.2.2.1 Electrolyte

The requirements of electrolytes material are high ionic conductivity, low electronic conductivity, stable in both reducing and oxidizing atmosphere over a wide range of oxygen partial pressure, and good thermal and mechanical properties. The electrolyte materials commonly used for SOFC are yttria-stabilized zirconia (YSZ), gadolinium- or samarium-doped ceria (GDC or SDC) and strontium, magnesium-doped lanthanum gallate (LSGM).

Each electrolyte offers advantages and disadvantages. YSZ, the most popular electrolyte, is now being used at high-temperature operating condition due to its good ionic conductivity. Since, it shows poor conductivity at lower temperature, another electrolyte operates at lower temperature are considerable interest. For example, ceria doped with rare earth metals has higher ionic conductivity and lower activation energy than YSZ, but the main problem of this material is the reduction of Ce^{4+} to Ce^{3+} at low oxygen partial pressure resulting in the introduction of electronic conductivity which decreases the cell efficiency [3]. LSGM, the perovskite oxide electrolyte, is stable without electronic conductivity in a wide range of oxygen partial pressures. It also shows high ionic conductivity at intermediate temperature compared to YSZ. Nevertheless, the high cost of Ga_2O_3 becomes an obstacle for the commercialization prospects of LSGM. The comparative conductivity of YSZ, GDC and LSGM are showed in Figure 1.2.



3914990606

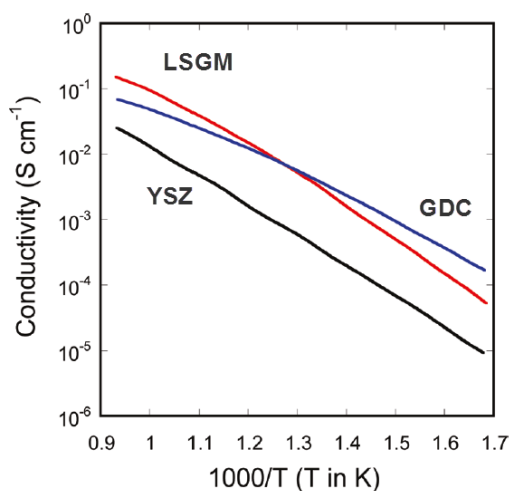


Figure 1.2 Conductivity of YSZ, GDC and LSGM [4]

Moreover the choice of electrolyte materials is also limited by thermal expansion coefficient (TEC). The TEC value of electrolyte must be matched to the electrode in order to avoid cracking. The TEC values for YSZ, GDC and LSGM are listed in Table 1.2.

Table 1.2 Thermal expansion coefficients of various electrolytes

Electrolyte	TEC ($1/^\circ\text{C}$)
YSZ	10.3×10^{-6} (30-1000 $^\circ\text{C}$) [5]
GDC	12.4×10^{-6} (30-1000 $^\circ\text{C}$) [6]
LSGM	9.78×10^{-6} (25-1000 $^\circ\text{C}$) [7]

1.2.2.2 Anode

Transition metals are good candidates as anode materials in SOFC. They may be classified with respect to H_2 oxidation rate as follows:



Among all transition metals, Ni is a popular choice of anode material because of its high catalytic activity and relatively low cost. However the high TEC value of nickel is a problem for using with YSZ electrolyte. The solution is by using the composite anode between nickel oxide and YSZ to give Ni-YSZ cermet. This composite anode provides both good ionic and electronic conductivity (from YSZ and Ni) and shows stable performance with H_2 fuel. However direct use of

hydrocarbon fuel leads to a strong adsorption of H_2S on the Ni particles resulting in the enhancement of the degree of activation polarization and performance loss [8]. Thus many alternatives have been proposed to overcome this problem such as using copper instead of nickel in the cermet and the development of novel anode materials.

Anode material requirements for SOFC can be summarized as follow:

- High catalytic activity for oxidation reaction of fuel gases
- Stability in low oxygen partial pressures
- Good chemical stability against the electrolyte and interconnect at high temperatures
- Tolerance to carbon cracking or sulfur impurities when using hydrocarbon fuels

1.2.2.3 Cathode

Generally, the main reaction occurring at the cathode is the reduction of gaseous oxygen into oxide ion. The mechanism of the reaction can be described as follow [9]:

- i) Oxygen surface adsorption and dissociation by breaking the covalent bond of O_2 molecules
- ii) Reduction of O species into oxide ions, O^{2-}
- iii) Oxide ion transfer within the bulk cathode
- iv) Oxide ion transport across the cathode/electrolyte interface

The oxygen reduction reaction plays a crucial role in the kinetics of SOFCs due to the major contribution to the activation polarization. Therefore, lots of research has gained much attention to the development of SOFC cathode material in order to reduce this polarization.

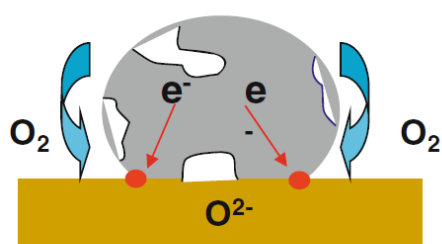
The choice of this material can be summarized as follows [10]:

- Chemical stability during cell operation
- High electronic conductivity
- Thermal expansion match with other cell components
- Minimum reactivity with electrolyte
- Sufficient porosity to facilitate transport of oxygen molecule



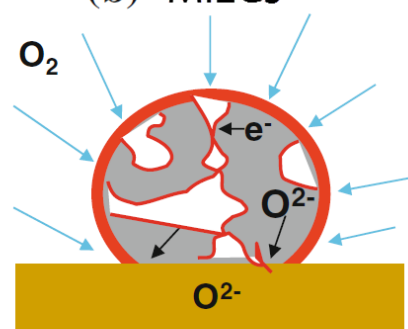
Conventional cathode materials used in SOFC are lanthanum-based perovskite materials, $\text{La}_{1-x}\text{Sr}_x\text{MnO}_3$ (LSM). They are only electronic conductors having high electronic conductivity, good stability and moderate thermal expansion coefficients (TEC) compatible to common electrolyte such as YSZ, which make LSM considered as the state-of-the-art cathode materials for SOFCs operating at high temperature (~ 1000 °C). However, the reduction of oxygen of this kind of cathode is limited to a narrow region called three-phase boundary (TPB) where air, electrode and electrolyte are in contact, as shown in Figure 1.3. Therefore, in order to extend the electrochemically active region from the limited TPB, mixed ionic and electronic conductors (MIECs) are required. Perovskite-type mixed ionic-electronic conducting oxides including simple perovskites, double ordered perovskites and Ruddlesden-Popper phases, have been widely studied as potential cathodes for IT-SOFC.

(a) Pure electronic conductor



Electrochemically active in the **TPB**, requires very high temperatures (LSM)

(b) MIECs



Great enhancement of the **active area**. Reduction of the working temperature.

Figure 1.3 Active areas for oxygen reduction reaction [11]

The desired properties and processing requirements for SOFC single cell component are summarized in Table 1.3.

Table 1.3 Micro-structural and property of SOFC component [12]

	Anode	Electrolyte	Cathode
Microstructure	Porous, many TPBs, stable to sintering.	Dense, thin, free of cracks and pinholes.	Porous, many TPBs, stable to sintering.
Electrical	Electronically and preferably ionically conductive.	Ionically but not electronically conductive.	Electronically and preferably ionically conductive.
Chemical	Stable in fuel atmosphere; preferably also stable in air for redox tolerance. Catalytic for oxidation and performing but not for carbon deposition.	Stable in both oxidizing and reducing environment. Minimal reduction and resulting electronic conductivity in reducing conditions.	Stable in air environments. Catalytic for oxygen reduction. Resistance to performance loss caused by chromium deposition.
Thermal expansion	Compatible with other layers, especially electrolyte.	Compatible with other layers, especially structural support layer.	Compatible with other layers, especially electrolyte.
Chemical compatibility	Minimal reactivity with electrolyte and interconnect.	Minimal reactivity with anode and cathode.	Minimal reactivity with electrolyte and interconnect.

1.3 Perovskite

Materials based on simple perovskite such as LaCoO_3 , BaCoO_3 or LaFeO_3 have attracted extensive attention due to the possible use as cathode materials for IT-SOFC. Their general formula is defined as ABX_3 where A (alkaline or alkaline earth metal) is a large cation in twelve fold coordination of X atoms, B (transition metal) is a smaller cation in octahedral coordination of X atoms. The Ideal perovskite structure is cubic and consists of a framework of corner-sharing BX_6 octahedral with the A cation located at the body center of the cube as shown in Figure 1.4. The

combination of perovskite (ABX_3) and rock salt (AX) framework results in a complex structural type, Ruddlesden-Popper (RP) structure.

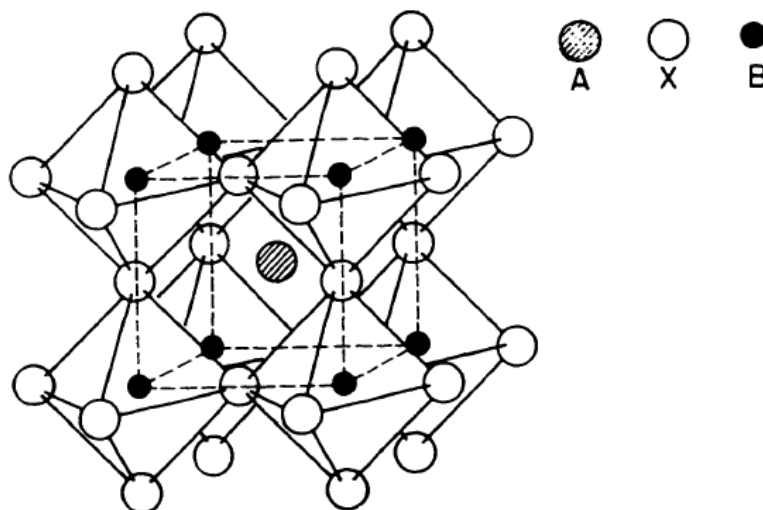


Figure 1.4 The perovskite structure (ABX_3) [13]

The K_2NiF_4 structure having the chemical formula A_2BX_4 is the first member of the RP series $(AX)(ABX_3)_n$ for $n \geq 1$. This structure has a cubic perovskite (ABX_3)_n layer alternating with an insulating rock salt AX layer along the c axis [14], as depicted in Figure 1.5. A repeat distance in layers leads to an ideal tetragonal structure with the space group $I4/mmm$. When the K_2NiF_4 structure tends to stoichiometric, the octahedra can be tilted to relieve structural stresses in the system. However, the oxygen interstitials occurred on the rock salt layer prevent the tilting of octahedra leading to the various phases of the K_2NiF_4 structure.

Several recent studies have highlighted A_2BO_4 oxides because these oxides can accommodate oxygen excess by the incorporation of interstitial oxygen (mainly in the rock salt layer) or generate lots of oxygen vacancy (mainly in the perovskite layer). This seems to improve the oxygen transport properties compared to simple perovskite.

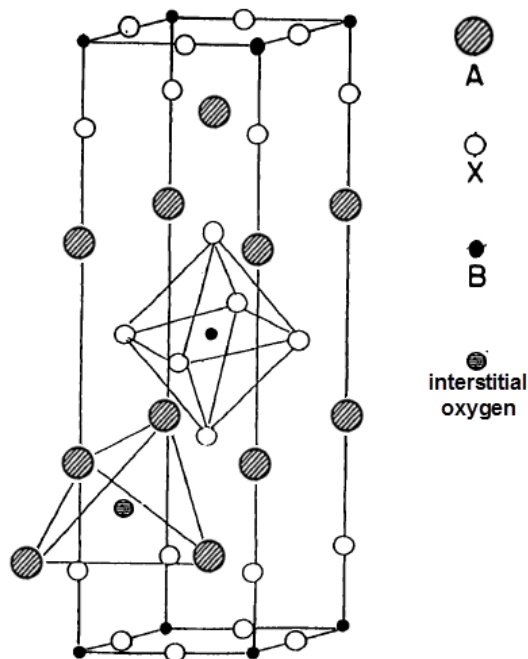


Figure 1.5 The A_2BO_4 structure showing the location of an interstitial oxygen atom [15]

Perovskites exhibit a wide range of magnetic and electrical behavior because many different ions can be combined into the structure so long as electrical neutrality is preserved. The Goldschmidt's tolerance factor (t) [16] as expressed in equation 1.1 is used to determine the degree of a combination of cations and anions which are feasible based on bond distances.

$$t = \frac{(r_A + r_O)}{\sqrt{2} x (r_B + r_O)} \quad (1.1)$$

Where r_A , r_B and r_O represent the ionic crystal radii of A-site cation, B-site cation and oxygen ion, respectively. The derivation of the tolerance factor is presented in Figure 1.6.

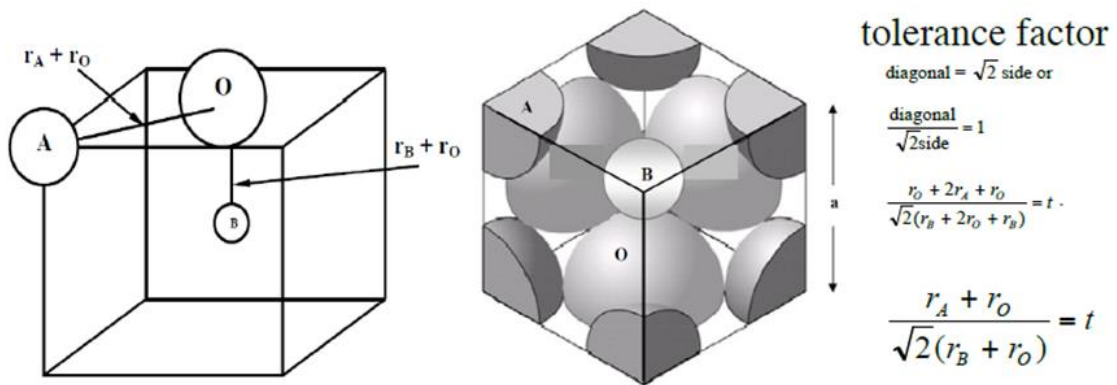


Figure 1.6 Derivation of the tolerance factor [17]

If $0.75 < t < 1.0$, the ions selected should be able to form a perovskite structure. When $t=1$, there are no stresses in the system, the perovskite is an ideal cubic. The cubic structure can be maintained with $0.95 < t < 1.04$, while $0.75 < t < 0.9$ low-symmetry orthorhombic or tetragonal structure will be obtained.

1.4 Electrical conductivity

The electrical conductivity (σ) [18] is one significant factor in the cathode performance. It can be calculated from the equation:

$$\sigma = nq\mu \quad (1.2)$$

Where n is the charge carrier concentration (cm^{-3}), q is the charge (in coulombs), and μ is the mobility of the charge carrier ($\text{cm}^2 \text{s}^{-1} \text{V}^{-1}$). The unit of σ is normally expressed in $\text{S} \cdot \text{cm}^{-1}$.

For perovskite oxides, their electrical conductivity is composed of two mechanisms, electronic and ionic conduction, because there are both electronic holes and oxygen vacancies appeared in the crystal structure. Generally, the electronic conduction is much higher than ionic conduction, thus the electrical conductivity values obtained are used to determine the electronic conductivity.

The electronic conductivity in perovskite oxides related to mobile charge carriers (excess electrons/electron holes) along the B–O–B chains. The electron/hole exchange causes by the overlapping of the orbitals of oxide ion and adjacent B-site cation as displayed in Figure 1.7. The higher the concentration of the mobile charge

carriers is, the higher the conductivity obtains. Generally, the generation of mobile charge carrier is by the replacement of trivalent cations with divalent cations at the A site. This leads to the reduction of total positive charge in the structure. Thus the increase in valence of the B cation (electronic compensation) or the generation of oxygen vacancies (ionic compensation) is occurred. However, the appearance of each type of charge compensation is undesirable because it is related to many factors including the temperature, the oxygen partial pressure, the type and concentration of dopants, the microstructure, etc.

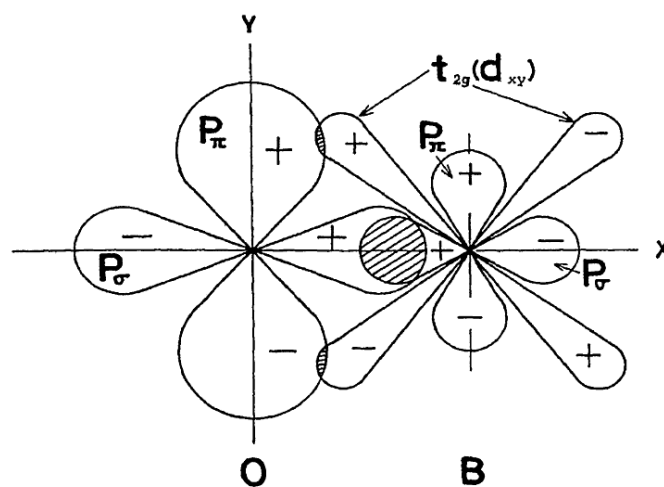


Figure 1.7 Covalent bonds between anionic p orbital and t_{2g} orbital of B-site cation [19]

For ionic conductivity, it is not only affected by the formation of oxygen vacancies and interstitial oxygen, it is also dependent on the critical radius (r_{cr}) [16], as expressed in equation 1.3. This factor corresponds to the maximum ionic radius of mobile ion to pass through the saddle point.

$$r_{cr} = \frac{a_0 \left(\frac{3}{4} a_0 - \sqrt{2} r_B \right) + r_B^2 - r_A^2}{2(r_A - r_B) + \sqrt{2} a_0} \quad (1.3)$$

Where r_A and r_B are the ionic radius of the A ion and B ion, respectively, and a_0 is the crystal parameter. The critical radius is normally less than 1.10 Å which is smaller than the ionic radius of oxygen ion.

The saddle point for oxygen ion migration is formed by two A-site cations and one B-site cation. The migration of the oxygen ion is by jumping from one site to the adjacent vacancy along the anion octahedral edge (Figure 1.8).

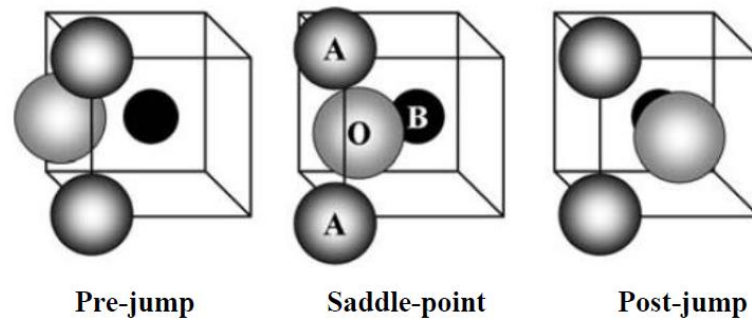


Figure 1.8 The migration of the oxygen ion passes through the saddle point [19]

1.5 Current-Voltage characterization

Figure 1.9 shows a current-voltage (I-V) curve in SOFC. Normally, the actual cell voltage is less than theoretical reversible voltage. The decrease of the cell voltage under current load depends on current density and many factors such as electrode or electrolyte materials, microstructure of the electrodes, temperature, etc. The difference between the theoretical reversible voltage and the actual cell voltage gives a polarization loss or over-potential (η) [20]. In the fuel system, there are three polarization losses:

- Activation polarization (η_{Act})
- Ohmic polarization (η_{Ohm})
- Concentration polarization (η_{Con})

The output power density, P is expressed as the product of cell voltage and current density:

$$P = iE \quad (1.4)$$

It can be seen from this equation that the power density equals zero at very low and very high current densities. Therefore the maximum power density is obtained between these two extremes (Figure 1.10).

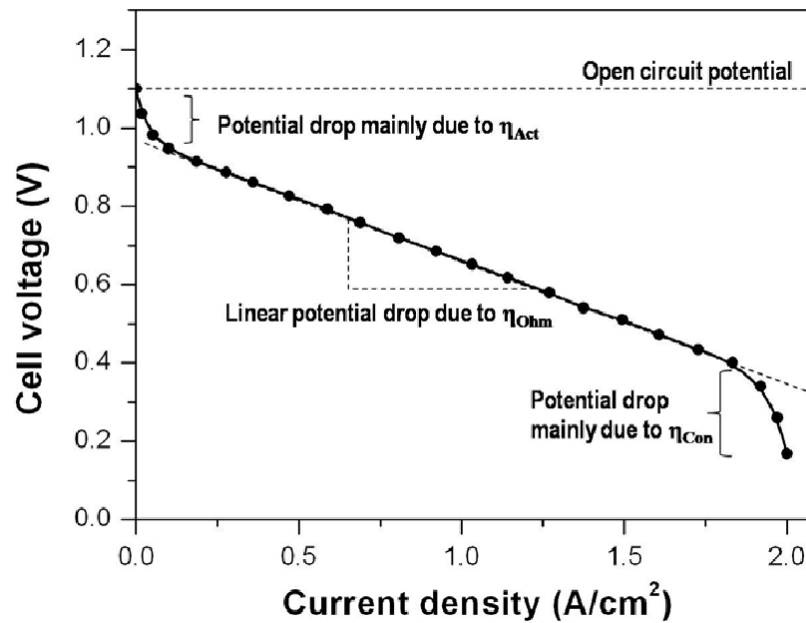


Figure 1.9 Characteristics of a typical current-voltage curve in SOFC [21]

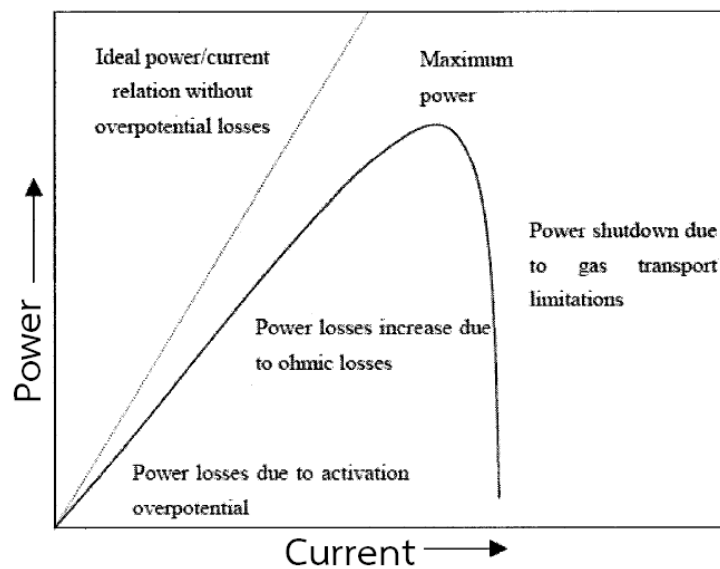


Figure 1.10 Typical power/current relation [21]

1.6 Electrochemical Impedance Spectroscopy (EIS) characterization

EIS is used to determine the polarization resistance in this study. It is measured by applying a small signal AC voltage over a wide frequency range and collecting the output current. The impedance (Z) is the ratio of the applied sinusoidal voltage and the resulting sinusoidal current, as related to Ohm's Law [22] in equation 1.5.

$$z = \frac{E(\omega)}{I(\omega)} = \frac{E_0 \cos(\omega t)}{I_0 \cos(\omega t - \varphi)} = Z_0 (\cos \varphi + j \sin \varphi) \quad (1.5)$$

Data obtained from the experiment are displayed in the form of Nyquist plot as shown in Figure 1.11. The x and y axes of this plot are the real and the imaginary parts of impedance, respectively. Moreover the circuit elements consisting of capacitor, resistor and inductance are used to describe some physical aspects of the system.

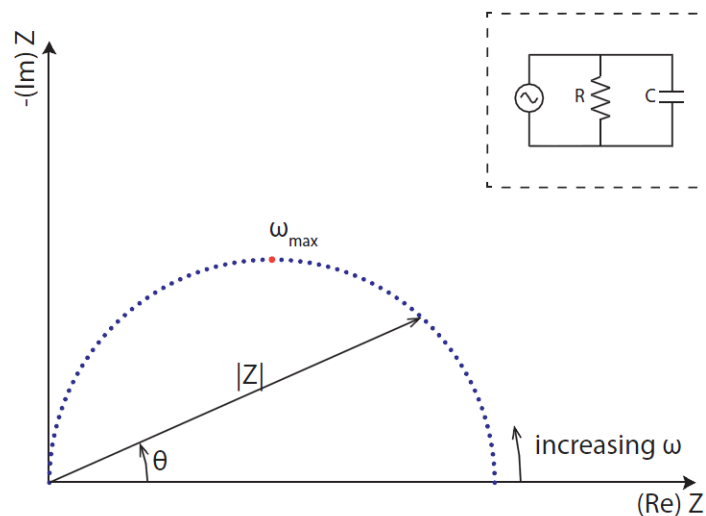


Figure 1.11 Schematic of a Nyquist plot [23]

1.7 Literature reviews

Solid oxide fuel cells (SOFCs) are the energy sources of current interest because they offer high power efficiency and low production of pollutants. To reduce its drawback in high temperature operation (800-1000°C), new cathode

materials with high electro-catalytic activity for IT-SOFC (600-800°C) have been developed.

The K_2NiF_4 -type or A_2BO_4 oxides, a two dimensional layered structure of insulating rock-salt (AO) separated by cubic perovskite (ABO_3) layers, have been widely studied because of their excellent mixed conductivity and catalytic activity. There are a lot of publications concerning the properties of this kind of cathode. La_2NiO_4 , one of the K_2NiF_4 -type oxides, is an interesting material which exhibits high mixed oxide ionic and electronic conductivity. It has high thermal stability and good catalytic activity. However there are many researchers trying to improve its properties. The partial substitution of metal ions on La_2NiO_4 shows a positive effect on the cathode performance, for example, substitution with Co ions 10 mole percent at the B-site and Sr ions 40 mole percent at the A-site can improve ionic and electronic conductivity [24, 25], respectively. Therefore, the development of $La_{1.6}Sr_{0.4}NiO_4$ (LSN), $La_{1.6}Sr_{0.4}Ni_{0.9}Co_{0.1}O_4$ (LSNC) and $La_2Ni_{0.9}Co_{0.1}O_4$ (LNC) is of interest in this work.

Cherry et al. [26] studied on $La_{1-x}(AE)_xCoO_3$ (AE =Ca, Mg, Sr, Ba). They found that substitution of $LaCoO_3$ with Ca and Sr, the oxygen vacancies were easy generated compared to substitution with Mg and Ba. These vacancies facilitated ionic conductivity.

Yang et al. [27] reported that substitution with Sr had an influence on the sintering densification and electrical conductivity of Pr_2NiO_4 . As Sr content increased, the compounds became denser and their electrical conductivity increased. However, the limitation of Sr addition in $Pr_{2-x}Sr_xNiO_4$ was less than $x=0.8$.

Zhao et al. [28] studied the polarization resistance (R_p) of $La_{2-x}Sr_xCo_{0.8}Ni_{0.2}O_4$ -GDC composite. The results showed that the introduction of Sr at the A-site had an effect on the reduction of R_p . Doping with Sr 80 mole percent, the R_p was 26 times lower than the R_p of the undoped one which implied to the increasing of electron hole when Sr-doping level was increased.

Shen et al. [29] studied the electrical conductivity of Ca-doped La_2NiO_4 . They found that Ca doping promoted the elongation of La-O bond length providing more space in La_2O_2 rock salt layers which facilitate the migration of oxide ion. Moreover, the activation energy of oxide ion migration and the amount of excess oxygen decreased with increasing Ca content. These lead to the high ionic conductivity. In case of electronic conductivity, it increased with Ca-doping level by charge compensation of the oxidation of Ni^{2+} to Ni^{3+} .

Ding et al. [30] investigated the thermal expansion and electrochemical performance of $\text{La}_{0.7}\text{AE}_{0.3}\text{CuO}_3$ (AE=Ca, Sr, Ba). It was found that Ca-containing composition had the highest electrical conductivity and the lowest thermal expansion coefficient (TEC). Moreover, the electrochemical activity was also enhanced.

Chen et al. [31] reported that the oxygen permeation flux of $\text{Ba}_{0.4}\text{Co}_{0.4}\text{Fe}_{0.4}\text{Zn}_{0.2}\text{O}_3$ did not decrease during the experimental operation of 100 hours. The reason was doping with zinc, which had a constant oxidation state of +2, avoided the reduction of $\text{Co}^{3+}/\text{Co}^{2+}$ or $\text{Fe}^{3+}/\text{Fe}^{2+}$.

Park et al. [32] studied the electrochemical behavior of $\text{Ba}_{0.5}\text{Sr}_{0.5}\text{Co}_{0.2-x}\text{Zn}_x\text{Fe}_{0.8}\text{O}_3$. They found that substitution with zinc improved the thermal stability and minimized the Co^{4+} loss in the structure. These resulted in the decrease of R_p value and high performance.

Kostogloudis et al. [33] examined the oxygen nonstoichiometry of $\text{Pr}_{1-x}\text{Sr}_x\text{Co}_{0.2}\text{B}_{0.8}\text{O}_3$ (PSC, B= Mn, Fe) by thermogravimetric analyses. They found that the loss of lattice oxygen in Fe-doped PSC was easily created, indicating the resistivity of the oxidation of Fe from Fe^{3+} to Fe^{4+} . Moreover, the magnitude of oxygen loss also increased with increasing the Sr content.

Petitjean et al. [34] investigated the oxygen transport properties of $(\text{La}_{0.8}\text{Sr}_{0.2})(\text{Mn}_{1-y}\text{Fe}_y)\text{O}_3$. They found that the oxygen diffusion via oxygen vacancy was enhanced by iron substitution because of the increase in oxygen vacancy concentration. On the other hand, the electronic conductivity was decreased resulting from the decrease in the concentration of available hopping site which limited the electrical conduction.

Miyoshi et al. [35] studied on Fe-doped $\text{Pr}_2\text{Ni}_{0.8}\text{Cu}_{0.2}\text{O}_4$ for oxygen-permeating membranes. They found that replacing Ni with Fe led to the increase in excess amount of oxygen, resulting in the enhancement of oxygen permeation rate, especially at low temperature. The highest oxygen permeation rate was achieved for $\text{Pr}_2\text{Ni}_{0.75}\text{Cu}_{0.2}\text{Fe}_{0.05}\text{O}_4$.

From the literatures, the substitution of Ca, Fe and Zn ions can promote the conducting properties of perovskite oxides. Therefore the purpose of this work is to improve such properties of $\text{La}_{1.6}\text{Sr}_{0.4}\text{NiO}_4$ (LSN), $\text{La}_{1.6}\text{Sr}_{0.4}\text{Ni}_{0.9}\text{Co}_{0.1}\text{O}_4$ (LSNC) and $\text{La}_2\text{Ni}_{0.9}\text{Co}_{0.1}\text{O}_4$ (LNC) including electrical conductivity and oxygen permeation by substitution of Ca, Fe and Zn ions, for an alternative cathode material in IT-SOFCs.

1.8 The objectives of this thesis

- 1.3.1 To synthesize K_2NiF_4 -type cathode materials substituted with Ca, Fe and Zn as below:
- $(La_{0.8}Sr_{0.2})_{2-x}Ca_xNiO_4$ (LSN- Ca_x , $x=0-0.5$)
 - $(La_{0.8}Sr_{0.2})_{2-x}Ca_xNi_{0.9}Co_{0.1}O_4$ (LSN- Ca_x , $x=0-0.5$)
 - $La_{2-x}Ca_xNi_{0.9-y}Co_{0.1}(Fe,Zn)_yO_4$ (LNCF- Ca_x and LNCZ- Ca_x , $y=0-0.2$, $x=0-0.7$)
- 1.3.2 To characterize the prepared compounds for phase structure, surface morphology and conducting property.
- 1.3.3 To measure the electrochemical performance of the selected compounds which perform good electrical conductivity by single cell test.



CHAPTER II EXPERIMENTAL

The chemicals and experimental procedures including preparation and characterization of materials are described below:

2.1 Chemicals

The chemicals and reagents listed in Table 2.1 were used without further purification.

Table 2.1 Chemicals and reagents for synthesis of materials

Chemicals and reagents	Formula weight	Purity%	Company
$\text{La}(\text{NO}_3)_3 \cdot 6\text{H}_2\text{O}$	433.02	99.0	Himedia
$\text{Ca}(\text{NO}_3)_2 \cdot 4\text{H}_2\text{O}$	236.15	99.0	Analytical
$\text{Sr}(\text{NO}_3)_2$	211.63	99.0	Aldrich
$\text{Ni}(\text{NO}_3)_2 \cdot 6\text{H}_2\text{O}$	290.81	97.0	Ajax
$\text{Co}(\text{NO}_3)_2 \cdot 6\text{H}_2\text{O}$	291.03	≥ 98.0	Ajax
$\text{Fe}(\text{NO}_3)_3 \cdot 9\text{H}_2\text{O}$	404.00	≥ 98.0	Fluka
$\text{Zn}(\text{NO}_3)_2 \cdot 6\text{H}_2\text{O}$	297.48	99.0	Fluka
La_2O_3	325.79	≥ 99.99	Wako
SrCo_3	147.63	≥ 99.9	Aldrich
Ga_2O_3	187.44	≥ 99.99	Aldrich
MgO	40.3	≥ 98.0	Fluka
NiO	74.60	≥ 99.9	Aldrich
$\text{C}_6\text{H}_8\text{O}_7$	192.43	≥ 99.5	Aldrich
HNO_3	63.01	65	Merck
liq. NH_3	35.05	25	Merck



3914990606

2.2 Material preparation

2.2.1 Cathode preparation

Modified citrate method was used for the formation of all cathodes. The abbreviation and composition of the different compounds synthesized are summarized in Table 2.2

Table 2.2 The composition of all prepared cathodes

Composition	Abbreviation
-Substitution La and Sr with Ca in $\text{La}_{1.6}\text{Sr}_{0.4}\text{NiO}_4$	
$\text{La}_{1.6}\text{Sr}_{0.4}\text{NiO}_4$	LSN
$(\text{La}_{0.8}\text{Sr}_{0.2})_{1.9}\text{Ca}_{0.1}\text{NiO}_4$	LSN-Ca _{0.1}
$(\text{La}_{0.8}\text{Sr}_{0.2})_{1.8}\text{Ca}_{0.2}\text{NiO}_4$	LSN-Ca _{0.2}
$(\text{La}_{0.8}\text{Sr}_{0.2})_{1.7}\text{Ca}_{0.3}\text{NiO}_4$	LSN-Ca _{0.3}
$(\text{La}_{0.8}\text{Sr}_{0.2})_{1.6}\text{Ca}_{0.4}\text{NiO}_4$	LSN-Ca _{0.4}
$(\text{La}_{0.8}\text{Sr}_{0.2})_{1.5}\text{Ca}_{0.5}\text{NiO}_4$	LSN-Ca _{0.5}
-Substitution La and Sr with Ca in $\text{La}_{1.6}\text{Sr}_{0.4}\text{Ni}_{0.9}\text{Co}_{0.1}\text{O}_4$	
$\text{La}_{1.6}\text{Sr}_{0.4}\text{Ni}_{0.9}\text{Co}_{0.1}\text{O}_4$	LSNC
$(\text{La}_{0.8}\text{Sr}_{0.2})_{1.9}\text{Ca}_{0.1}\text{Ni}_{0.9}\text{Co}_{0.1}\text{O}_4$	LSNC-Ca _{0.1}
$(\text{La}_{0.8}\text{Sr}_{0.2})_{1.8}\text{Ca}_{0.2}\text{Ni}_{0.9}\text{Co}_{0.1}\text{O}_4$	LSNC-Ca _{0.2}
$(\text{La}_{0.8}\text{Sr}_{0.2})_{1.7}\text{Ca}_{0.3}\text{Ni}_{0.9}\text{Co}_{0.1}\text{O}_4$	LSNC-Ca _{0.3}
$(\text{La}_{0.8}\text{Sr}_{0.2})_{1.6}\text{Ca}_{0.4}\text{Ni}_{0.9}\text{Co}_{0.1}\text{O}_4$	LSNC-Ca _{0.4}
$(\text{La}_{0.8}\text{Sr}_{0.2})_{1.5}\text{Ca}_{0.5}\text{Ni}_{0.9}\text{Co}_{0.1}\text{O}_4$	LSNC-Ca _{0.5}
-Substitution Ni with Fe or Zn in $\text{La}_2\text{Ni}_{0.9}\text{Co}_{0.1}\text{O}_4$	
$\text{La}_2\text{Ni}_{0.9}\text{Co}_{0.1}\text{O}_4$	LNC
$\text{La}_2\text{Ni}_{0.89}\text{Co}_{0.1}\text{Fe}_{0.01}\text{O}_4$	LNC-Fe _{0.01}
$\text{La}_2\text{Ni}_{0.87}\text{Co}_{0.1}\text{Fe}_{0.03}\text{O}_4$	LNC-Fe _{0.03}
$\text{La}_2\text{Ni}_{0.85}\text{Co}_{0.1}\text{Fe}_{0.05}\text{O}_4$	LNC-Fe _{0.05}
$\text{La}_2\text{Ni}_{0.8}\text{Co}_{0.1}\text{Fe}_{0.1}\text{O}_4$	LNC-Fe _{0.1}
$\text{La}_2\text{Ni}_{0.7}\text{Co}_{0.1}\text{Fe}_{0.2}\text{O}_4$	LNC-Fe _{0.2}



3914990606

$\text{La}_2\text{Ni}_{0.89}\text{Co}_{0.1}\text{Zn}_{0.01}\text{O}_4$	LNC-Zn _{0.01}
$\text{La}_2\text{Ni}_{0.87}\text{Co}_{0.1}\text{Zn}_{0.03}\text{O}_4$	LNC-Zn _{0.03}
$\text{La}_2\text{Ni}_{0.85}\text{Co}_{0.1}\text{Zn}_{0.05}\text{O}_4$	LNC-Zn _{0.05}
$\text{La}_2\text{Ni}_{0.8}\text{Co}_{0.1}\text{Zn}_{0.1}\text{O}_4$	LNC-Zn _{0.1}
$\text{La}_2\text{Ni}_{0.7}\text{Co}_{0.1}\text{Zn}_{0.2}\text{O}_4$	LNC-Zn _{0.2}
-Substitution La with Ca in $\text{La}_2\text{Ni}_{0.85}\text{Co}_{0.1}\text{Fe}_{0.05}\text{O}_4$	
$\text{La}_2\text{Ni}_{0.85}\text{Co}_{0.1}\text{Fe}_{0.05}\text{O}_4$	LNCF
$\text{La}_{1.9}\text{Ca}_{0.1}\text{Ni}_{0.85}\text{Co}_{0.1}\text{Fe}_{0.05}\text{O}_4$	LNCF -Ca _{0.1}
$\text{La}_{1.7}\text{Ca}_{0.3}\text{Ni}_{0.85}\text{Co}_{0.1}\text{Fe}_{0.05}\text{O}_4$	LNCF -Ca _{0.3}
$\text{La}_{1.5}\text{Ca}_{0.5}\text{Ni}_{0.85}\text{Co}_{0.1}\text{Fe}_{0.05}\text{O}_4$	LNCF -Ca _{0.5}
$\text{La}_{1.3}\text{Ca}_{0.7}\text{Ni}_{0.85}\text{Co}_{0.1}\text{Fe}_{0.05}\text{O}_4$	LNCF -Ca _{0.7}
-Substitution La with Ca in $\text{La}_2\text{Ni}_{0.85}\text{Co}_{0.1}\text{Zn}_{0.05}\text{O}_4$	
$\text{La}_2\text{Ni}_{0.85}\text{Co}_{0.1}\text{Zn}_{0.05}\text{O}_4$	LNCZ
$\text{La}_{1.9}\text{Ca}_{0.1}\text{Ni}_{0.85}\text{Co}_{0.1}\text{Zn}_{0.05}\text{O}_4$	LNCZ -Ca _{0.1}
$\text{La}_{1.7}\text{Ca}_{0.3}\text{Ni}_{0.85}\text{Co}_{0.1}\text{Zn}_{0.05}\text{O}_4$	LNCZ -Ca _{0.3}
$\text{La}_{1.5}\text{Ca}_{0.5}\text{Ni}_{0.85}\text{Co}_{0.1}\text{Zn}_{0.05}\text{O}_4$	LNCZ -Ca _{0.5}
$\text{La}_{1.3}\text{Ca}_{0.7}\text{Ni}_{0.85}\text{Co}_{0.1}\text{Zn}_{0.05}\text{O}_4$	LNCZ -Ca _{0.7}

- Preparation of powder

Stoichiometric amounts of corresponding metal nitrates were dissolved in deionized water and nitric acid. Subsequently, citric acid in the molar ratio of 2 mol of citric acid to 1 mol of metal ions was added drop wise into the solution with continuous stirring at room temperature. After 3 hours, ammonia solution was slowly added to adjust the pH value of the solution to about 9 and then stirred at room temperature for 2 hours. The obtained solution was dehydrated and slowly heated until self-combustion of the precipitate. The resulting ash was then ground using a mortar pestle and finally calcined at 900°C for 10 hours in an air-muffle furnace.

- Preparation of disc

The calcined powders were finely ground with ethanol by a mortar pestle for 30 minutes. The 1.8 g fine powders were loaded into the cavity of a KBr die to

prepare a round disc (20 mm in diameter). The die having metal oxide powder inside was knocked against table for 2-3 times to evaporate air inside the powder. After the die was completely assembled, the plunger was brought to the surface of the powders gently for final leveling and smoothing surface. After that the pressure was slowly applied about 2 tons for 10 minutes to obtain a disc. Then the disc was sintered at 1350°C for 10 hours in air.

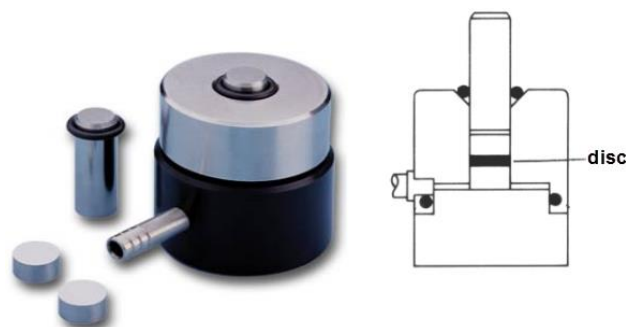


Figure 2.1 KBr die assembly

2.2.2 Anode preparation [36]

The anode used was NiO-Fe₂O₃ (9:1), which synthesized by conventional impregnation technique. Fe(NO₃)₃·9H₂O was firstly dissolved in DI water, followed by the addition of NiO. After that the mixed solution was evaporated and finally the brown powder resulted. The obtained powder was calcined in a furnace at 400°C for 2 hours to get rid of the remaining nitrate and then fired at 1200°C for 6 hours. In order to obtain a fine and uniform particle mixture, the resulting powder was ground in ethanol for 1 hour.

2.2.3 Electrolyte preparation [37]

La_{0.9}Sr_{0.1}Ga_{0.8}Mg_{0.2}O₃ (abbreviated as LSGM) was used as electrolyte in this study. It was synthesized by conventional solid state method. Calculated amounts of La₂O₃, SrCO₃, Ga₂O₃ and MgO were mixed for 1 hour in a mortar pestle and then calcined at 1000°C for 6 hours. The resulting powders were pulverized and pressed isostatically into a disc (20 mm in diameter). The discs were sintered at 1500°C for 5 hours in air and then polished to the thickness of 0.3 mm by a diamond grinding machine.

2.3 Material characterization

2.3.1 X-ray diffractometry (XRD)

The phase formation of the sintered samples was examined by X-ray powder diffraction using a Rigaku Dmax-2200 Ultima⁺ diffractometer with monochromatic Cu K α radiation (40 kV, 30 mA) at Department of Chemistry, Faculty of Science, Chulalongkorn University. The data was collected in the range of 20 to 70 degree with scan speed of 5 degree/min and the lattice parameter were calculated based on the XRD data with Jade software.

2.3.2 Scanning electron microscopy (SEM)

Microstructural characterization of the sample discs was carried out with a JEOL JSM-5800LV scanning electron microscopy with an Oxford Instrument (model Link ISIS series 300) at the Scientific and Technological Research Equipment Center (STREC), Chulalongkorn University.

2.3.3 Density

The Archimedes method was used to measure the bulk density of sintered samples. The sample discs were firstly boiled in deionized water for 5 hours to release air in sample pores and then weighted in dry and wet condition using Precisa Gravimetrics AG (model R 2055M-DR) at Department of Chemistry, Faculty of Science, Chulalongkorn University. The relative density was calculated from the ratio of the measured bulk density to the theoretical density determined by XRD data.

2.3.4 Electrical conductivity measurement

The electrical conductivity of sintered samples was measured by a standard four-probe direct current (DC) technique under air condition. The sintered disc was cut into a rectangular bar with approximate dimensions of 5 mm x 12 mm x 1.5 mm. Four platinum wires were attached to the bar with platinum paste and fired at 950°C for 10 min with a heating rate of 5°C/min to obtain good electric contact as shown in Figure 2.2. The different voltage between two probes was recorded in a tube furnace at various temperatures in the range of 300 to 800°C with a heating rate of 5°C/min. The electrical conductivity was then calculated by following equation:

$$\sigma = (I/V)*(L/(W*T))$$



- where σ is electrical conductivity (S/cm)
- I is fixed current (A)
- V is difference of measured voltage between two probes (V)
- L is distance between two voltage contact points (cm)
- T is thickness of rectangular bar (cm)
- W is width of rectangular bar (cm)

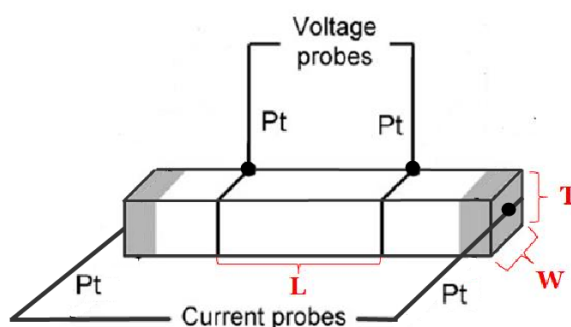


Figure 2.2 schematic diagram of specimen with four platinum (Pt) wire contacts

2.3.5 Oxygen permeation measurement

The discs were used as membranes for measurement of oxygen permeation flux. Each membrane was polished to the thickness of 0.7 mm with a diamond wheel, and then aligned with the two alumina tubes. Between the membrane and the tubes, ring-shaped Pyrex glass was placed as a sealing glass to prevent leakage. A seal was formed when the membrane and part of the alumina tubes were heated to 1000°C. The experimental set-up is shown in Figure 2.3.

Dry air (AR grade) and helium gas (99.999%) at a flow rate of 50 mL/min was fed to the membrane and the oxygen partial pressure gradient was achieved. The oxygen permeation measurement was carried out from high to low temperature in the range of 600 to 1000°C. The mixed gases of helium, used as the sweep gas, and permeated oxygen were then injected into the gas chromatography equipment (VARIAN, CP-3800) equipped with a molecular sieve 13X packed column and a thermal conductivity detector for determining the oxygen content.

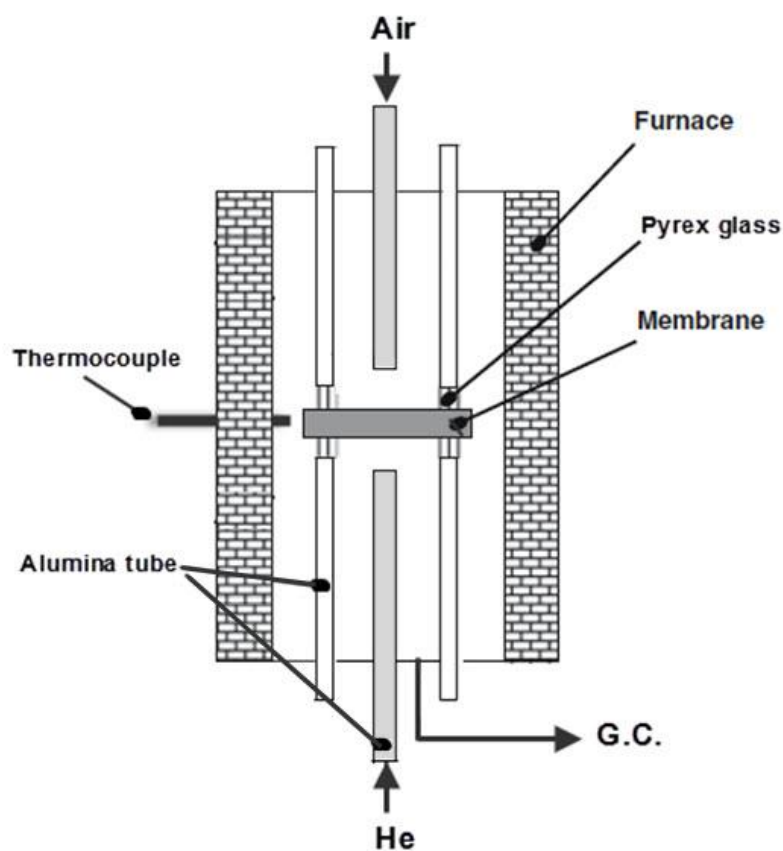


Figure 2.3 Cross-sectional view of the membrane reactor

2.3.6 Electrochemical measurement

Electrochemical performances and AC impedance analyses were evaluated on single cells at temperature between 600 and 800°C.

- Single Cell Performance Test

Single cell performances of various cathodes were evaluated with LSGM electrolyte and Ni-Fe oxide, as an anode precursor. All the electrode powders synthesized were mixed with STD-100 binder in a mass ratio of 1:1 and then painted onto both sides of the electrolyte surface by hand, followed by firing at 1000°C for 30 minutes to remove the organic solvent and complete the interface contact between electrolyte and electrodes. Pt meshes and wires were fabricated to each electrode as current collector. The schematic configuration of the test cell is shown in Figure 2.4.

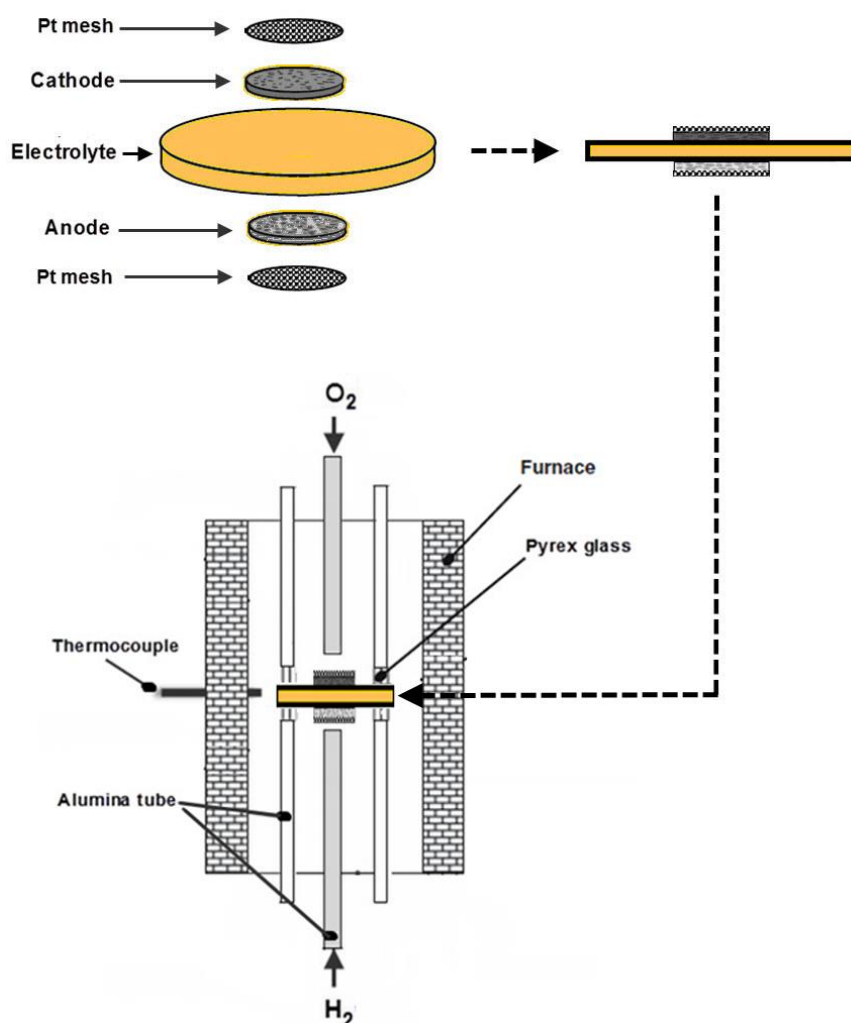


Figure 2.4 Schematic configuration of the single cell performance test set-up

The Ni-Fe anode was reduced to a metallic state at 800°C for 1 hour under H₂ flow before the cell performance measurement. During the operation, H₂ (99.999%) as fuel and O₂ (99.98%) as oxidant were supplied to the cathode and anode, respectively at a rate of 100 mL/min. Current-voltage (I-V) were measured with an AUTOLAB PGSTAT302N instrument using galvanostatic mode.

- AC Impedance Measurement

AC impedance was analyzed in air by a potentiostat having a frequency response analyzer, and the test cell geometry and configuration were same as that used for the single cell performance test. The applied frequency ranged from 0.1 Hz to 10⁶ Hz with voltage amplitude of 10 mV.

CHAPTER III RESULTS AND DISCUSSION

3.1 Tolerance factor

The stability of perovskite structure of all prepared compounds was determined by tolerance factors (t). These factors were calculated based on chemical formulae using ionic crystal radii as tabulated by Shannon and Prewitt (Appendix A). The calculated t values of all prepared oxides are listed in Table 3.1.

Table 3.1 The tolerance factors of all prepared oxides

a) $(\text{La}_{0.8}\text{Sr}_{0.2})_{2-x}\text{Ca}_x\text{NiO}_4$ (LSN- Ca_x)

Compounds	t
LSN	0.891
LSN- $\text{Ca}_{0.1}$	0.891
LSN- $\text{Ca}_{0.2}$	0.890
LSN- $\text{Ca}_{0.3}$	0.889
LSN- $\text{Ca}_{0.4}$	0.888
LSN- $\text{Ca}_{0.5}$	0.887

b) $(\text{La}_{0.8}\text{Sr}_{0.2})_{2-x}\text{Ca}_x\text{Ni}_{0.9}\text{Co}_{0.1}\text{O}_4$ (LSNC- Ca_x)

Compounds	t
LSNC	0.889
LSNC- $\text{Ca}_{0.1}$	0.888
LSNC- $\text{Ca}_{0.2}$	0.887
LSNC- $\text{Ca}_{0.3}$	0.886
LSNC- $\text{Ca}_{0.4}$	0.885
LSNC- $\text{Ca}_{0.5}$	0.884

c) $\text{La}_2\text{Ni}_{0.89-y}\text{Co}_{0.1}\text{M}_y\text{O}_4$ (LNC- Fe_y or LNC- Zn_y)

Compounds	t
LNC	0.883
LNC- $\text{Fe}_{0.01}$	0.882
LNC- $\text{Fe}_{0.03}$	0.882
LNC- $\text{Fe}_{0.05}$	0.881
LNC- $\text{Fe}_{0.1}$	0.879
LNC- $\text{Fe}_{0.2}$	0.875

Compounds	t
LNC	0.883
LNC- $\text{Zn}_{0.01}$	0.883
LNC- $\text{Zn}_{0.03}$	0.882
LNC- $\text{Zn}_{0.05}$	0.882
LNC- $\text{Zn}_{0.1}$	0.881
LNC- $\text{Zn}_{0.2}$	0.879



d) $\text{La}_{2-x}\text{Ca}_x\text{Ni}_{0.85}\text{Co}_{0.1}\text{M}_{0.05}\text{O}_4$ (LNCf-Ca_x or LNCZ-Ca_x)

Compounds	<i>t</i>	Compounds	<i>t</i>
LNCf	0.881	LNCZ	0.882
LNCf -Ca _{0.1}	0.880	LNCZ -Ca _{0.1}	0.881
LNCf -Ca _{0.3}	0.879	LNCZ -Ca _{0.3}	0.880
LNCf -Ca _{0.5}	0.878	LNCZ -Ca _{0.5}	0.879
LNCf -Ca _{0.7}	0.877	LNCZ -Ca _{0.7}	0.878

The perovskite structure is stable when *t* value locate in the range of $0.75 < t < 1.0$ [38]. As *t* tends to 1, the structure is closer to the ideal cubic structure. The cubic structure can be maintained with $0.95 < t < 1.04$, while $0.75 < t < 0.9$ low-symmetry orthorhombic or tetragonal structure will be obtained [19, 39]. It can be seen from Table 3.1 that the *t* values of all prepared oxides vary from 0.877 to 0.891 and they are larger than 0.75 indicating the ability to form stable perovskite structure. However, the tolerance factors are less than 0.95. This means that they do not have a cubic structure. When A-site cation is substituted by Ca²⁺, whose ionic radius is smaller than that of A-site cation (La³⁺ and Sr²⁺) or substitution of B-site cation (Ni²⁺) by larger cation (Fe²⁺ and Zn²⁺), the *t* value decreases. This indicates that the unit cell is distorted resulting in the change of lattice structure from cubic to another structure such as tetragonal structure.

3.2 Synthesis and properties of $(\text{La}_{0.8}\text{Sr}_{0.2})_{2-x}\text{Ca}_x\text{NiO}_4$ (LSN-Ca_x)

LSN-Ca_x (x=0, 0.1, 0.2, 0.3, 0.4 and 0.5) were synthesized and sintered at 1350°C for 10 hours. The obtained samples were characterized for phase structure, surface morphology and conducting property by XRD, SEM and DC 4-probe method, respectively. LSN-Ca_x with the highest electrical conductivity was chosen for testing the single cell performance.

3.2.1 XRD analyses

Figure 3.1 shows the XRD patterns of LSN-Ca_x sintered at 1350°C for 10 hours. All the diffraction peaks can be indexed as K₂NiF₄-type with tetragonal structure (JCPDS 89-8309). It is noticed that the main diffraction peaks of LSN-Ca_x shift to higher values of 2θ compared to the undoped one. This shift is resulted from the shrinkage

of crystal lattice caused by substitution of La^{3+} ($r=1.36 \text{ \AA}$) and Sr^{2+} ($r=1.45 \text{ \AA}$) with Ca^{2+} ($r=1.32 \text{ \AA}$), as explained by Bragg's law in equation 3.1.

$$2d \sin\theta = n\lambda \quad (3.1)$$

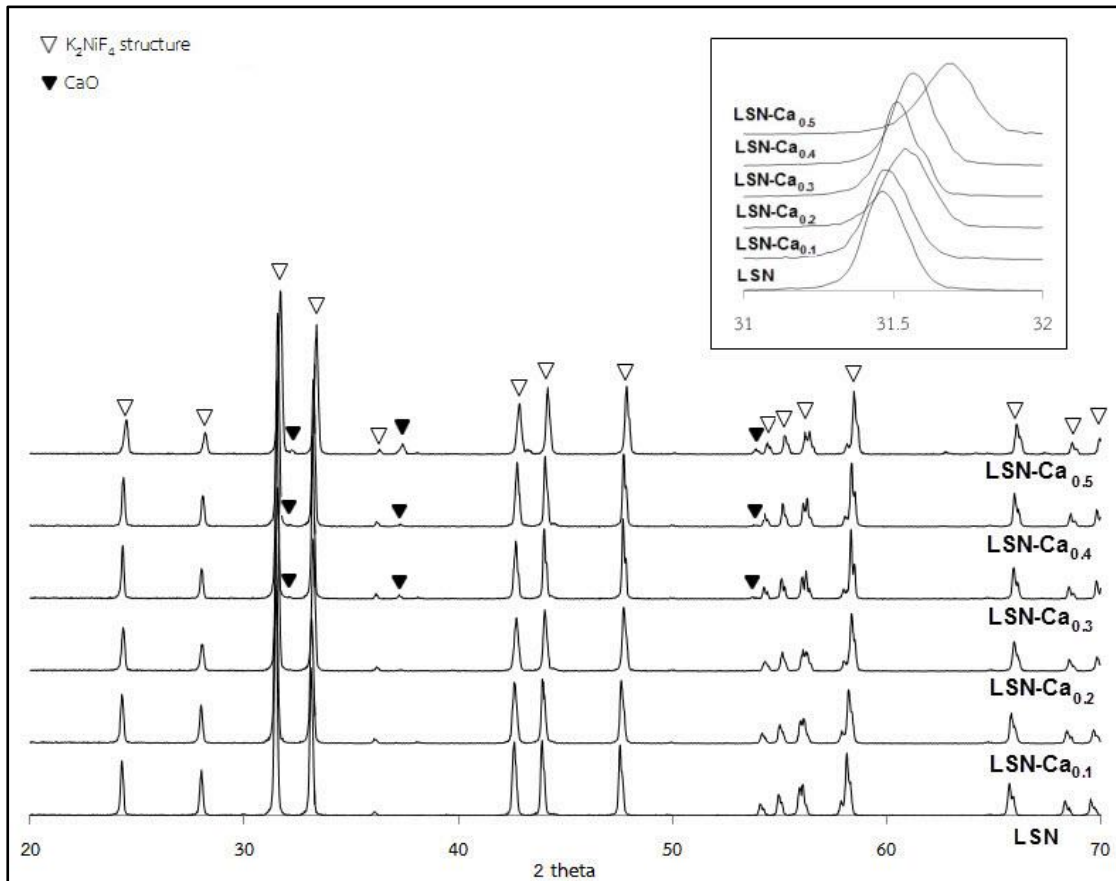


Figure 3.1 XRD patterns of LSN- Ca_x ($x=0-0.5$) discs sintered at 1350°C for 10 hours

The lattice parameters a , c and the unit cell volume decrease with the calcium content as presented in Table 3.2. This shrinkage of lattice parameters can be attributed to two factors. Firstly, the substitution of low valence cations (Ca^{2+}) will induce the oxidation state of B-site cations in the ABO_3 layer from Ni^{2+} , Ni^{3+} to Ni^{4+} due to the electroneutrality condition. From the valence bond theory, in this case the Ni-O bond strength will increase and the bond length decreases [40]. Secondly, the substitution of smaller cations on the A-site will affect the A-O bond in the rock salt layer resulting in the shrinkage of A-O bond [41].

Table 3.2 Lattice parameter and unit cell volume of LSN-Ca_x (x=0-0.5)

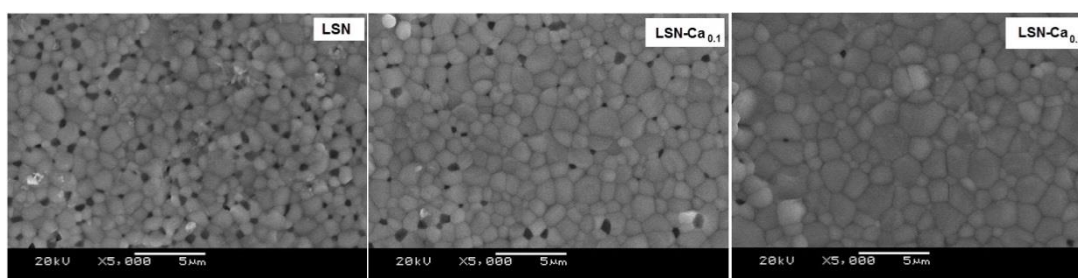
Compound	* Lattice parameter		V (Å ³)
	a (Å)	c (Å)	
LSN	3.819	12.741	185.77
LSN-Ca _{0.1}	3.818	12.719	185.37
LSN-Ca _{0.2}	3.813	12.687	184.46
LSN-Ca _{0.3}	3.816	12.690	184.80
LSN-Ca _{0.4}	3.811	12.684	184.22
LSN-Ca _{0.5}	3.820	12.665	184.78

*The average lattice parameters are calculated from the diffraction peaks of (101), (103), (110), (114) and (200) planes.

In addition, the formation of CaO (JCPDS 48-1467) is observed for x>0.2. At x=0-0.2, there are no secondary phase appeared. Therefore, the limitation of Ca²⁺ addition in LSN is considered to be less than 0.3.

3.2.2 SEM analyses

LSN, LSN-Ca_{0.1} and LSN-Ca_{0.2} discs without impurity phase were chosen to study the surface morphology. The reduction of porosity and the agglomeration of grains were determined by SEM images in Figure 3.2. When LSN is substituted by Ca²⁺ in the A-site, the dense microstructure with few isolated pores and large grain sizes are obtained.

**Figure 3.2** SEM images of LSN-Ca_x (x=0, 0.1 and 0.2) discs

The increase in Ca²⁺ substitution promotes the higher grain size and the large density of materials which is consistent with the result of relative density calculation as shown in Table 3.3.

Table 3.3 Average grain size and relative density of LSN-Ca_x (x=0, 0.1 and 0.2) discs

Sample	Grain size (μm)	Relative density (%)
LSN	0.94	80.60
LSN-Ca _{0.1}	1.42	82.27
LSN-Ca _{0.2}	1.88	95.18

3.2.3 Electrical conductivity analyses

Figure 3.3 shows the Ca-doping level and electrical conductivity of LSN-Ca_x as a function of temperature. Moreover, the data are summarized in Table 3.4.

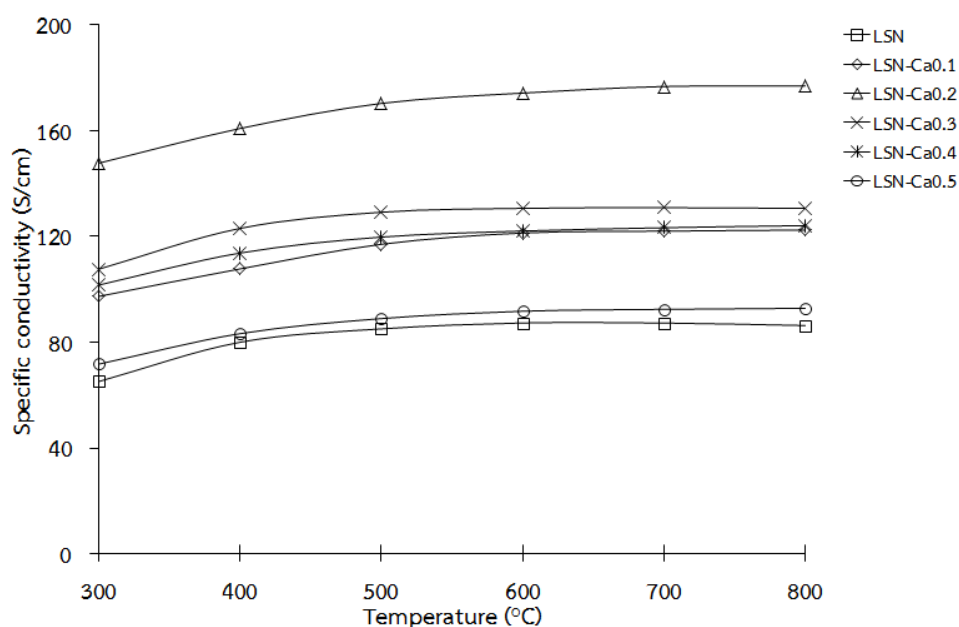


Figure 3.3 Temperature dependence of the specific conductivity (σ) of LSN-Ca_x (x=0-0.5)

The electrical conductivity of all samples shows an identical variation with temperature. It increases with increasing temperature and then remains constant at elevating temperature because at high temperature, phonon concentration increases and causes lattice scattering which lowers the electron mobility. Moreover the loss of lattice oxygen at high temperature results in the generation of oxygen vacancies [42] and the reduction of the number of conductivity carriers as expressed in equation 3.2.



where O_o^x = an oxide ion on an oxide ion lattice site, with neutral charge
 $V_o^{\bullet\bullet}$ = oxygen vacancies

At each temperature, the electrical conductivity increases with calcium content and reaches a maximum value at $x=0.2$, followed by a decrease of electrical conductivity with more Ca-doping ($x=0.3, 0.4$ and 0.5), but it is still higher than the undoped one. The conductivity increases with calcium due to the increasing concentration of electron holes in material as charge compensation of Ca-doping on A-site as described in equation 3.3



where Ca'_{La} = a calcium ion on a lanthanum ion lattice site, with singular negative charge
 Ni_{Ni}^{\bullet} = a nickel ion on a nickel ion lattice site, with singular positive charge
 $V_o^{\bullet\bullet}$ = oxygen vacancies

Based on defect chemistry theory, the electron holes can be obtained by the change in valence state of B-site ions. In this case, the partial replacement of A-site cation with lower valent cation (Ca^{2+}) leads to the change of B-site cation from Ni^{3+} to Ni^{4+} that would introduce electronic conductivity (electron holes by $Ni_{Ni^{3+}}^{4+\bullet}$). Moreover, the increasing of conductivity can be explained by the increased overlapping of the atomic orbits. From previous XRD results, lattice parameters a and c decreased with increasing Ca^{2+} substitution. This was indicated that the bond length of Ni-O-Ni reduced and the overlapping of the atomic orbitals between the adjacent Ni was promoted leading to the fast migration of electron. Therefore the conductivity increases.

The decreased electrical conductivity of samples with $x=0.3, 0.4$ and 0.5 is mainly due to the appearance of impurity (CaO) as recognized by XRD. Moreover it may associate with the distorted unit cells with increasing calcium content causing the small orbital overlap. This will be unfavorable to the charge carrier transfer in materials [43].



Table 3.4 The specific conductivity of LSN-Ca_x (x=0-0.5)

Sample	Specific conductivity (S/cm)						σ_{\max} (T, °C)
	300°C	400°C	500°C	600°C	700°C	800°C	
LSN	65.2	80.0	85.1	87.3	87.2	86.4	87.3 (600)
LSN-Ca _{0.1}	97.4	107.8	117.1	121.3	122.0	122.4	122.4 (800)
LSN-Ca _{0.2}	147.7	160.8	170.3	174.2	176.7	176.9	176.9 (800)
LSN-Ca _{0.3}	107.6	123.1	129.2	130.7	130.9	130.6	130.9 (700)
LSN-Ca _{0.4}	101.6	113.7	119.8	122.1	123.3	124.1	124.1 (800)
LSN-Ca _{0.5}	71.8	83.3	89.0	91.8	92.5	92.9	92.9 (800)

In addition, the relative density has a dramatic effect on the electrical conductivity of materials. The dense microstructure can contribute to an increase of the bulk conductivity. The sample with x=0.2 which density is higher than others offers a maximum electrical conductivity of 176.9 S/cm at 800°C.

The Arrhenius plot for electrical conductivity of samples is shown in Figure 3.4. The linear relationship between $\ln(\sigma T)$ and $1000/T$ demonstrates a semiconducting behavior, which the electrical conduction occurs by thermally activated hopping of small polarons [44]. With increasing temperature, the hopping of small polarons increases. The slope of the linear part of Arrhenius plot can determine the activation energy (E_a) values in Table 3.5.

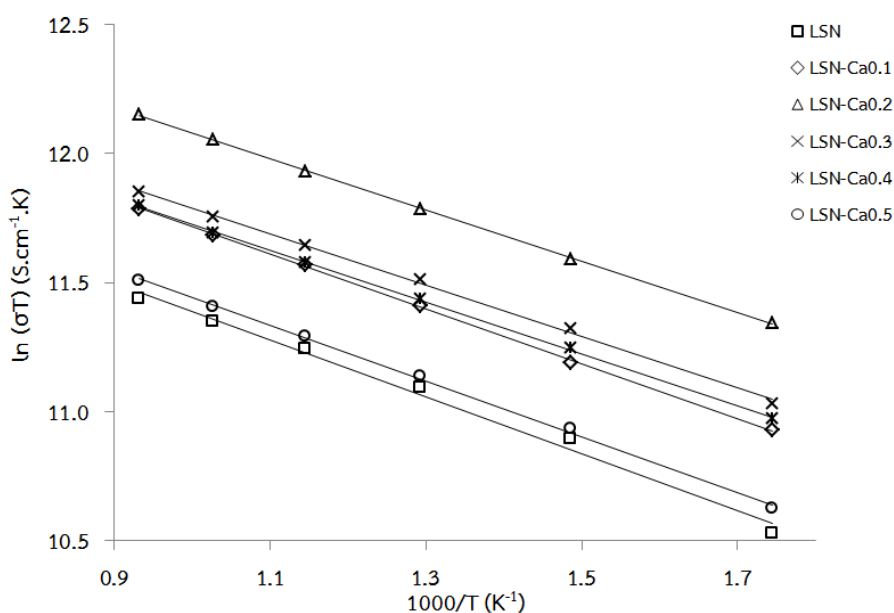
**Figure 3.4** Arrhenius plot of the electrical conductivity of LSN-Ca_x (x=0-0.5)

Table 3.5 Activation energy (E_a) of LSN-Ca_x (x=0-0.5) at 300-800°C

Sample	E_a (kJ/mol)
LSN	9.2
LSN-Ca _{0.1}	8.8
LSN-Ca _{0.2}	8.3
LSN-Ca _{0.3}	8.3
LSN-Ca _{0.4}	8.4
LSN-Ca _{0.5}	9.0

The E_a value is used to determine the electron hopping. The lower the value of E_a , the faster the hopping of electrons. The lowest E_a value was obtained for x=0.2 which corresponds to the highest conductivity of LSN-Ca_{0.2} in this work.

3.3 Synthesis and properties of (La_{0.8}Sr_{0.2})_{2-x}Ca_xNi_{0.9}Co_{0.1}O₄ (LSNC-Ca_x)

LSNC-Ca_x (x=0, 0.1, 0.2, 0.3, 0.4 and 0.5) were synthesized and sintered at 1350°C for 10 hours. The obtained samples were characterized for phase structure, surface morphology and conducting property by XRD, SEM and DC 4-probe method, respectively. LSNC-Ca_x with the highest electrical conductivity was chosen for testing the single cell performance.

3.3.1 XRD analyses

The XRD patterns of LSNC-Ca_x (Figure 3.5) show the similar result with LSN-Ca_x. These patterns reveal the K₂NiF₄-type with tetragonal structure. It is observed that the peaks are slightly shifted to higher angle with increasing the calcium content. It confirms that Ca occupies a part of La and Sr sites in crystal lattice. When A-site cations are substituted by low valence cations, the average oxidation state of B-site cations will increase, causing the change in crystal structure. In this case, Ni²⁺ and Co²⁺ are oxidized to small size cations therefore the lattice parameter is diminished. The lattice parameters a , c and the unit cell volume of LSNC-Ca_x were calculated in Table 3.6.

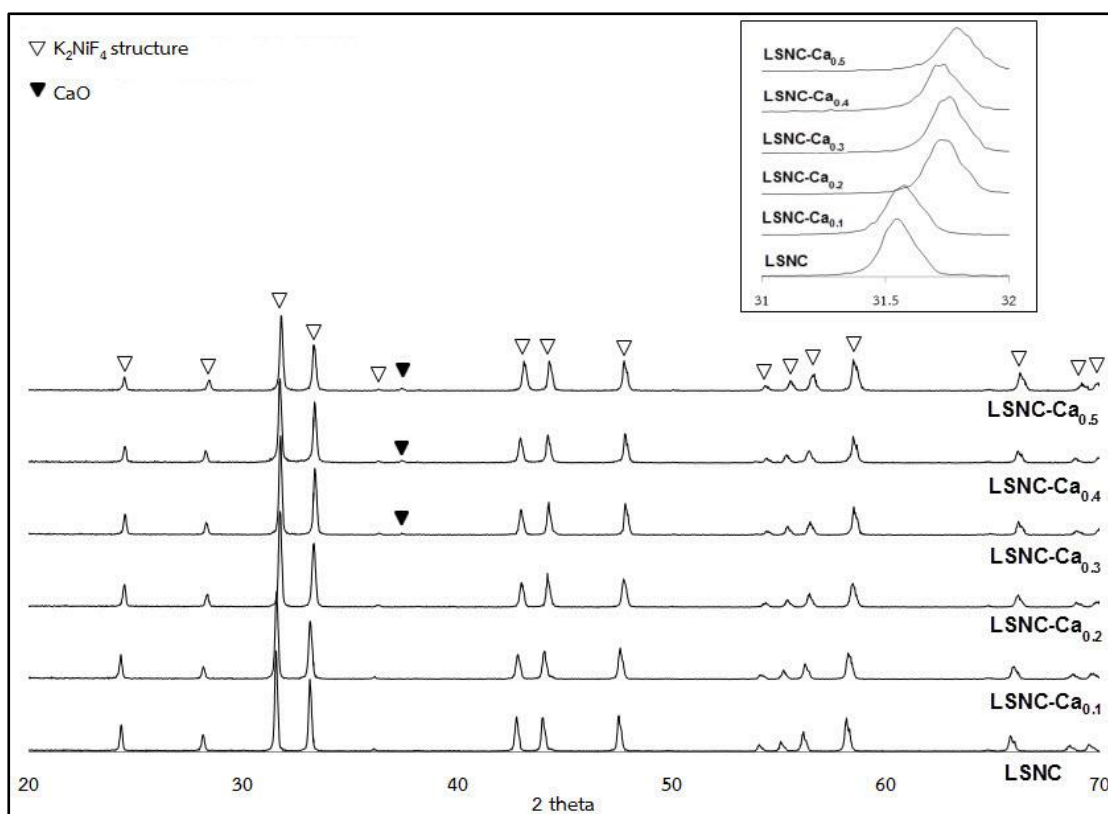


Figure 3.5 XRD patterns of LSNC-Ca_x (x=0-0.5) discs sintered at 1350°C for 10 hours

Table 3.6 Lattice parameter and unit cell volume of LSNC-Ca_x (x=0-0.5)

Compound	* Lattice parameter		V (Å ³)
	a (Å)	c (Å)	
LSNC	3.819	12.741	185.77
LSNC-Ca _{0.1}	3.818	12.719	185.37
LSNC-Ca _{0.2}	3.813	12.687	184.46
LSNC-Ca _{0.3}	3.816	12.690	184.80
LSNC-Ca _{0.4}	3.820	12.665	184.78
LSNC-Ca _{0.5}	3.811	12.684	184.22

*The average lattice parameter is calculated from the diffraction peaks of (101), (103), (110), (114) and (200) planes.

The formation of CaO impurity phase is observed in composition of $x > 0.2$, which is recognized from the main peak at 2θ of 37.5° . Therefore, it is considered that the limitation of Ca addition in LSNC is less than 0.3.

3.3.2 SEM analyses

LSNC, LSNC-Ca_{0.1} and LSNC-Ca_{0.2} discs with pure single phase structure were chosen to study the surface morphology. From SEM images in Figure 3.6, LSNC exhibits porous surface materials. With increasing the calcium substitution, the grain size increases and no porosity are observed in sample with x= 0.2. The average grain size and the calculated relative density were listed in Table 3.7. It is found that the relative density increases from approximately 84% for LSNC to 91% for LSNC-Ca_{0.2}, suggesting that substitution of calcium enhances the density of LSNC-Ca_x in this work.

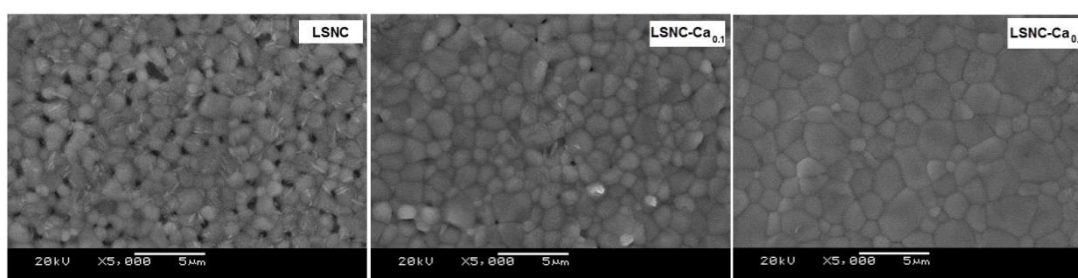


Figure 3.6 SEM images of LSNC-Ca_x (x=0, 0.1 and 0.2) discs

Table 3.7 Average grain size and relative density of LSNC-Ca_x (x=0, 0.1 and 0.2) discs

Sample	Grain size (μm)	Relative density (%)
LSNC	1.02	84.07
LSNC-Ca _{0.1}	1.39	90.69
LSNC-Ca _{0.2}	2.06	91.47

3.3.3 Electrical conductivity analyses

Figure 3.7 represents the temperature dependence of electrical conductivity as a function of Ca-doping concentrations and the data are summarized in Table 3.8.

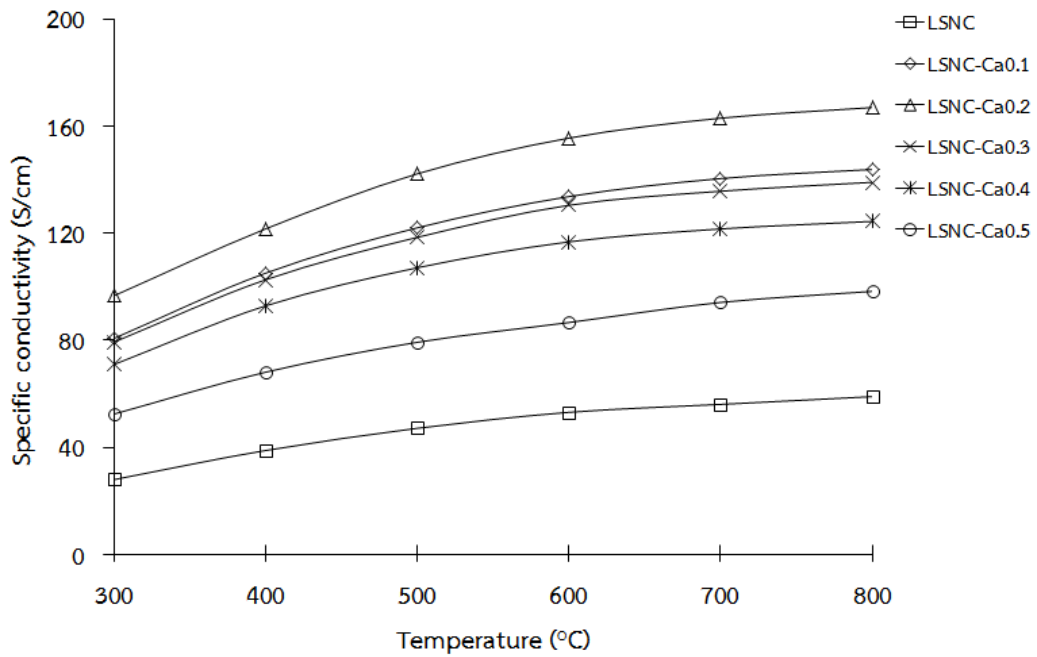


Figure 3.7 Temperature dependence of the specific conductivity (σ) of LSNC-Ca_x ($x=0-0.5$)

It is observed that the electrical conductivity of all LSNC-Ca_x samples exhibits semiconducting behavior. It increases with increasing temperature. Moreover the calcium substitution on A-site in LSNC affects the electrical conductivity. The conductivity increases with the calcium content and reaches a maximum value for sample with $x=0.2$. This result can be explained by the increasing of concentration and mobility of electron holes. The replacement of La³⁺ with Ca²⁺ results in the production of electron holes in Ni site and Co site or the formation of oxygen vacancies [45]. The individual defect equilibrium can be described by equation 3.4.



where Ca'_{La} = a calcium ion on a lanthanum ion lattice site, with singular negative charge

Ni_{Ni}^{\bullet} = a nickel ion on a nickel ion lattice site, with singular positive charge

Co_{Co}^{\bullet} = a cobalt ion on a cobalt ion lattice site, with singular positive charge

$V_o^{\bullet\bullet}$ = oxygen vacancies

The highest electrical conductivity is achieved for LSNC-Ca_{0.2} and the value is 166.9 S/cm at 800°C. The conductivity decreases with the composition of $x > 0.2$. This may be due to the appearance of impurity phase (CaO) which has low electrical conductivity.

Table 3.8 The specific conductivity of LSNC-Ca_x (x=0-0.5)

Sample	Specific conductivity (S/cm)						σ_{\max} (T, °C)
	300°C	400°C	500°C	600°C	700°C	800°C	
LSNC	28.0	38.8	47.2	53.1	56.1	59.0	59.0 (800)
LSNC-Ca _{0.1}	80.7	105.1	122.0	133.7	140.4	143.8	143.8 (800)
LSNC-Ca _{0.2}	96.6	121.6	142.1	155.5	162.9	166.9	166.9 (800)
LSNC-Ca _{0.3}	79.3	102.6	118.4	130.4	135.7	139.0	139.0 (800)
LSNC-Ca _{0.4}	70.9	92.8	107.1	116.8	121.6	124.4	124.4 (800)
LSNC-Ca _{0.5}	52.4	68.1	79.2	86.6	94.2	98.3	98.3 (800)

The activation energy of LSNC-Ca_x calculated from the slope of Arrhenius plot (Figure 3.8) at 300-800°C is summarized in Table 3.9. The linear relationship between $\ln(\sigma T)$ and $1000/T$ indicates the small polaron conducting mechanism [46]. It can be seen that the E_a value decreases with increasing the calcium content until $x=0.2$. This can be explained by substitution of calcium leading to the reduction of Ni-O bond length which may result in an easy jump of electron holes [45]. Therefore activation energy for the hopping of electron holes is decreased. When $x > 0.2$, the E_a value increases but it is still lower than the undoped one. The lowest E_a value was obtained for $x=0.2$ which corresponds to the highest conductivity of LSNC-Ca_x in this work.

Table 3.9 Activation energy (E_a) of LSNC-Ca_x (x=0-0.5) at 300-800°C

Sample	E_a (kJ/mol)
LSNC	14.0
LSNC-Ca _{0.1}	12.2
LSNC-Ca _{0.2}	12.1
LSNC-Ca _{0.3}	12.2
LSNC-Ca _{0.4}	12.1
LSNC-Ca _{0.5}	12.8

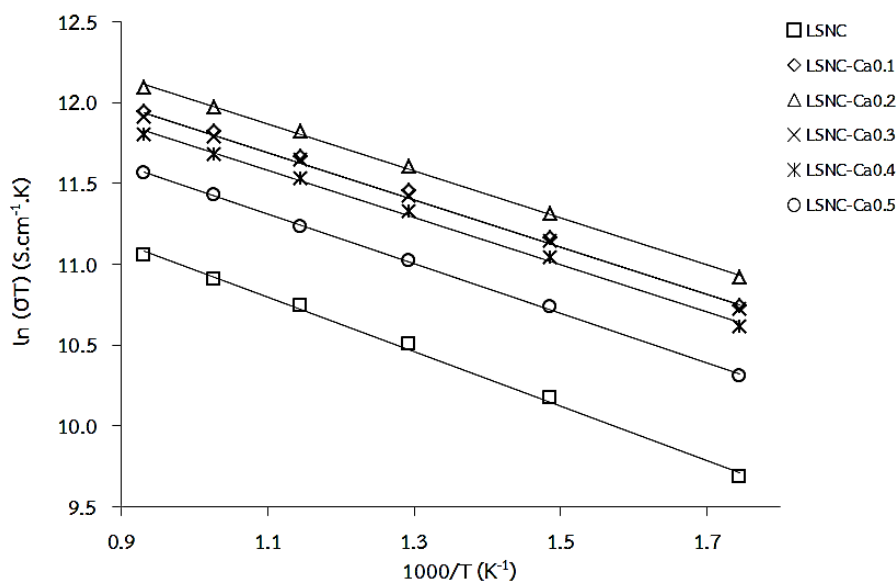


Figure 3.8 Arrhenius plot of the electrical conductivity of LSN-Ca_x (x=0-0.5)

3.4 Synthesis and properties of La₂Ni_{0.9-y}Co_{0.1}M_yO₄ (M=Fe, Zn and y=0-0.2)

LNC-Fe_y and LNC-Zn_y (y=0, 0.01, 0.03, 0.05, 0.1 and 0.2) were synthesized and sintered at 1350 °C for 10 hours. The obtained samples were characterized for phase structure, surface morphology and oxygen permeation. LNC-Fe_y and LNC-Zn_y with the highest oxygen permeation rate was chosen for substitution of Ca in La-site to improve electrical conductivity in the next experiment.

3.4.1 XRD analyses

The XRD patterns of LNC-Fe_y and LNC-Zn_y are illustrated in Figure 3.9 and 3.10, respectively. The phase is identified as K₂NiF₄-type with tetragonal structure (JCPDS 34-0314). The main diffraction peak around 2θ of 31.5 degree shifts to lower angle with the introduction of iron or zinc, corresponding to an increase in the lattice parameters as presented in Table 3.10 and 3.11. This is due to the fact that the substitution with larger cation (Fe²⁺=0.92 Å, Zn²⁺=0.88 Å) causes an expansion in lattice parameters. However, the secondary phase, La₂O₃ (JCPDS 05-0602), is found in the composition of y≥0.1, indicating the limitation of Fe and Zn introduced into the structure. Therefore, LNC-Fe_y and LNC-Zn_y which y<0.1 were selected for further study.

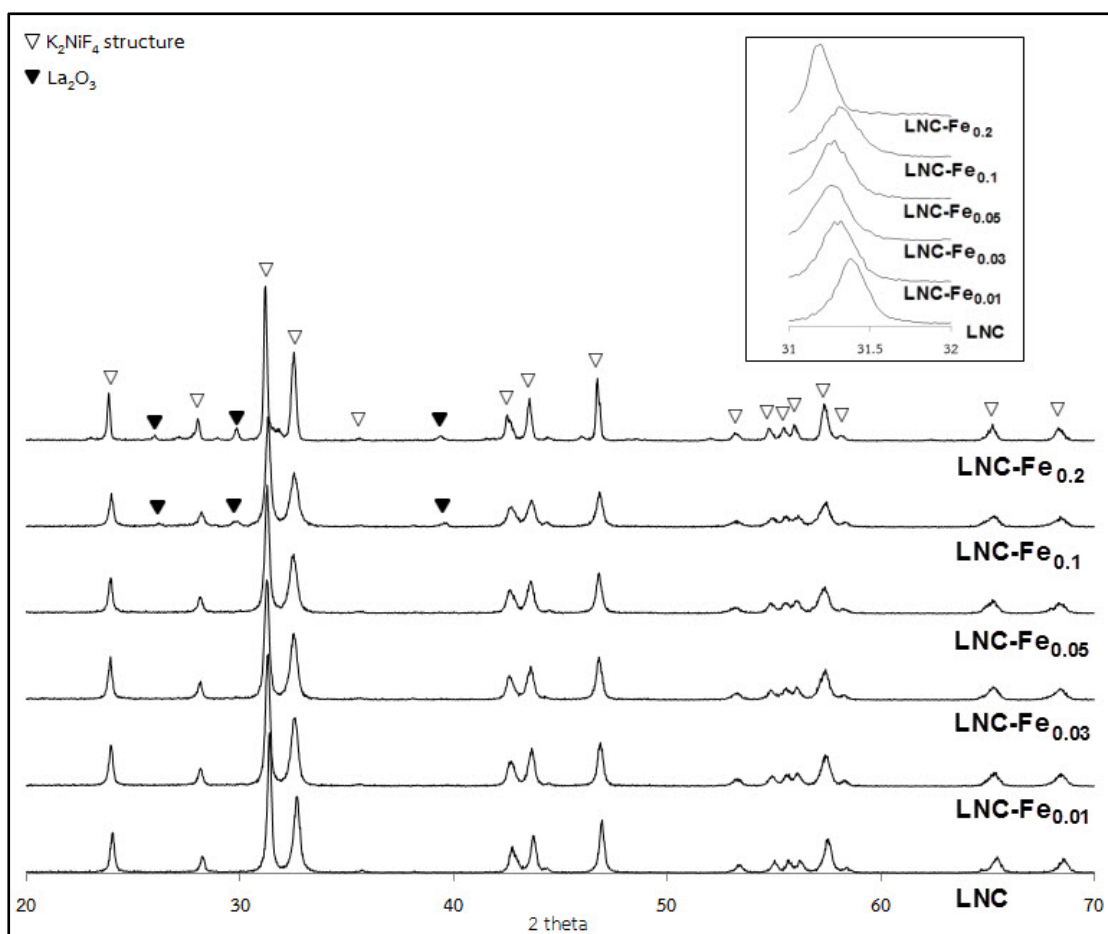


Figure 3.9 XRD patterns of LNC- Fe_y discs sintered at 1350°C for 10 hours

Table 3.10 Lattice parameters and unit cell volume of LNC- Fe_y

Compound	* Lattice parameter		V (\AA^3)
	a (\AA)	c (\AA)	
LNC	3.869	12.646	189.25
LNC- $Fe_{0.01}$	3.881	12.682	190.99
LNC- $Fe_{0.03}$	3.878	12.710	191.14
LNC- $Fe_{0.05}$	3.885	12.682	191.45
LNC- $Fe_{0.1}$	3.879	12.708	191.19
LNC- $Fe_{0.2}$	3.893	12.671	192.05

*The average lattice parameter is calculated from the diffraction peaks of (101), (103), (110), (114) and (200) planes.

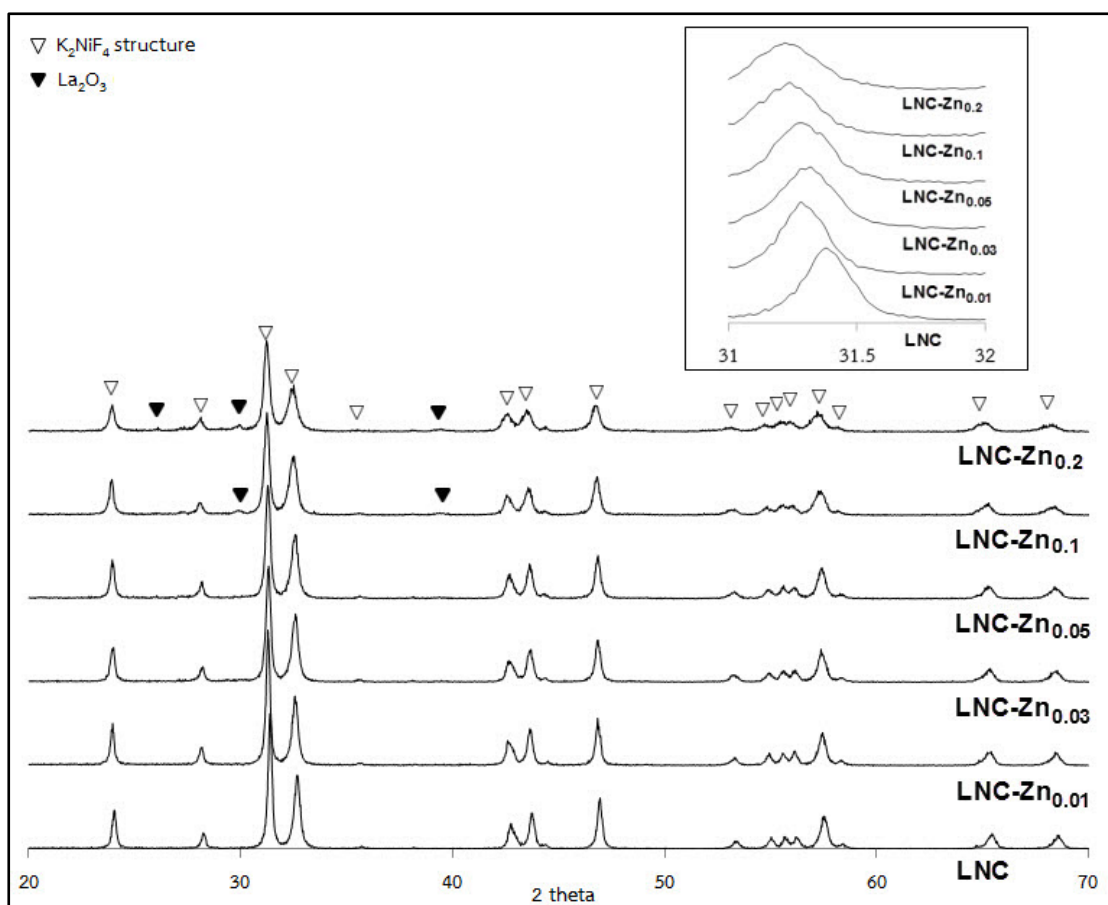


Figure 3.10 XRD patterns of LNC-Zn_y discs sintered at 1350°C for 10 hours

Table 3.11 Lattice parameters and unit cell volume of LNC-Zn_y

Compound	* Lattice parameter		V (Å ³)
	a (Å)	c (Å)	
LNC	3.869	12.646	189.25
LNC-Zn _{0.01}	3.879	12.653	190.35
LNC-Zn _{0.03}	3.873	12.697	190.47
LNC-Zn _{0.05}	3.888	12.719	192.23
LNC-Zn _{0.1}	3.888	12.669	191.53
LNC-Zn _{0.2}	3.887	12.624	190.73

*The average lattice parameter is calculated from the diffraction peaks of (101), (103), (110), (114) and (200) planes.

3.4.2 SEM analyses

Figure 3.11 shows the surface microstructures of LNC-Fe_y and LNC-Zn_y (y=0, 0.01, 0.03, 0.05). Moreover the average grain size and calculated relative density were presented in Table 3.12. All samples reveal good densification and no porosity are appeared. The grain size is between 2.0 and 3.8 μm. It is known that the oxygen permeation measurement requires very dense discs (≈94% of theoretical density) and the absence of open porosity in the sample [47]. It can be seen that the density of all samples in this system is higher than 95% which is sufficient for the requirement of oxygen permeation measurement. However, there is no relationship between the density and the amount of Fe or Zn substitution.

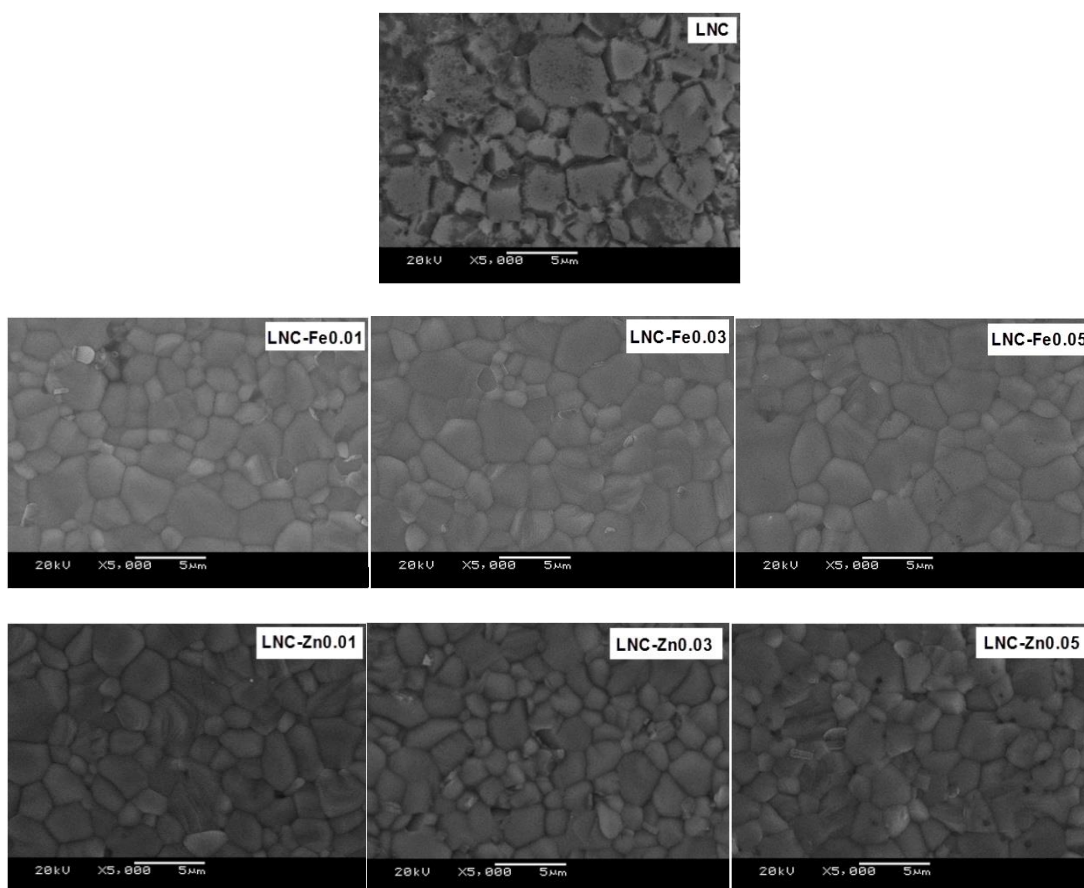


Figure 3.11 SEM images of LNC-Fe_y and LNC-Zn_y (y=0, 0.01, 0.03 and 0.05) discs

Table 3.12 Average grain size and relative density of LNC-Fe_y and LNC-Zn_y (y=0, 0.01, 0.03 and 0.05) discs

Sample	Grain size (μm)	Relative density (%)
LNC	3.8	98.94
LNC-Fe _{0.01}	2.9	96.83
LNC-Fe _{0.03}	3.6	95.98
LNC-Fe _{0.05}	3.8	96.53
LNC-Zn _{0.01}	2.6	95.79
LNC-Zn _{0.03}	2.1	96.98
LNC-Zn _{0.05}	2.0	96.44

3.4.3 Oxygen permeation analyses

The variation of oxygen permeation rate with temperature was measured on LNC-Fe_y and LNC-Zn_y (y=0, 0.01, 0.03 and 0.05) and the results are presented in Figure 3.12 and 3.13, respectively.

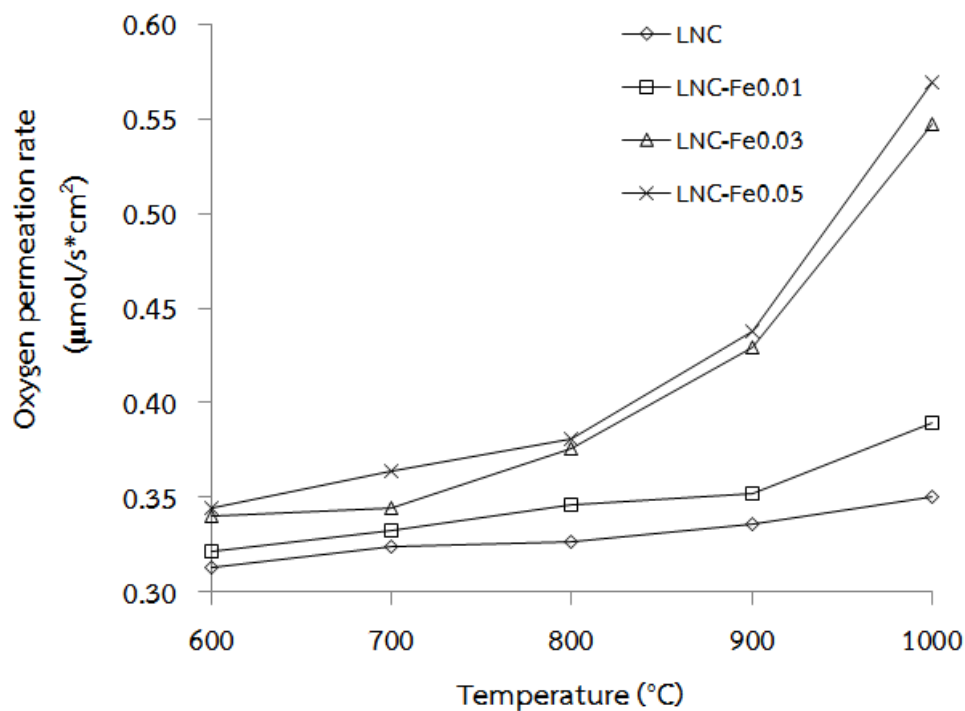


Figure 3.12 Temperature dependence of oxygen permeation for LNC-Fe_y (y=0, 0.01, 0.03 and 0.05)

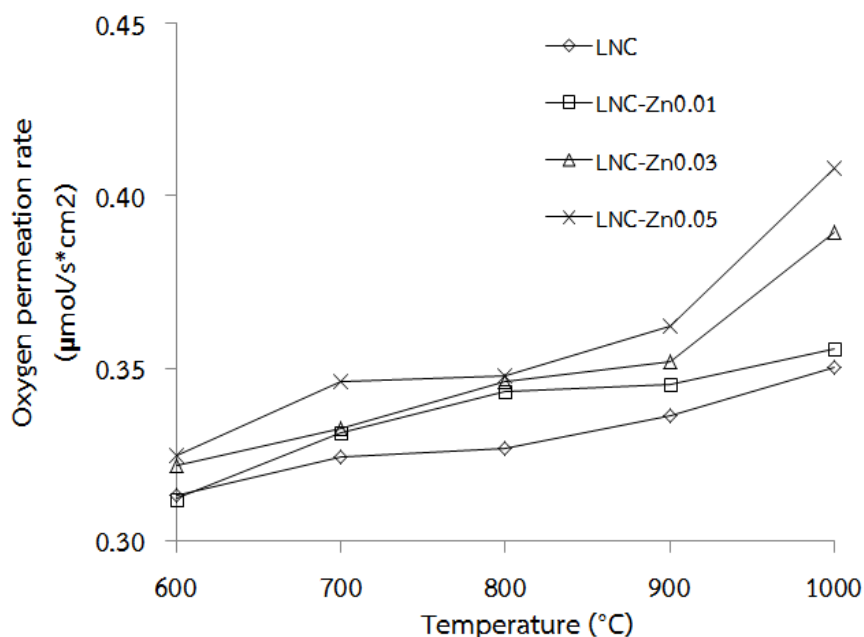


Figure 3.13 Temperature dependence of oxygen permeation for LNC-Zn_y (y=0, 0.01, 0.03 and 0.05)

It is found that the oxygen permeation rate increases with increasing temperature. At high temperature, the loss of lattice oxygen results in the increasing of concentration and mobility of oxide ion [48] and the decreasing of activation energy for the ion mobility and surface exchange [49]. Therefore the oxygen permeation rate increases with temperature. Moreover the partial substitution of B-site cations with Fe or Zn leads to the higher oxygen permeation rate. Substitution with y=0.05 shows the highest oxygen permeation rate in each series. The maximum oxygen permeation rate value is 0.57 and 0.41 $\mu\text{mol/s}\cdot\text{cm}^2$ at 1000°C for LNC-Fe_{0.05} and LNC-Zn_{0.05}, respectively.

The oxygen permeation rate is influenced by many structural factors such as lattice free volume of the unit cell and available channels for mobility oxide ion (saddle point) [50]. Doping B-site cation with large ionic size results in the lattice expansion which providing more space in the structure. Moreover the electrostatic force between cations and oxide ions is also weaker and the saddle point is expanded. Thus, the oxide ions easily move throughout the structure leading to the high oxygen permeation rate.

In addition, the increasing of oxygen permeation can be explained by the increased concentration of oxygen vacancies which facilitate oxide ion mobility via oxygen vacancies [34]. In case of LNC-Zn_y, Zn has a fixed valence state of +2. When doping of this ion, the preferred mechanism of charge compensation is the generation of oxygen vacancies in the structure rather than the formation of electron hole because of its unchangeable oxidation state. Miyoshi [35] reported that for Pr₂Ni_{0.8-x}Cu_{0.2}Fe_xO₄, the enhancement in the oxygen permeation by replacing of Ni with Fe can be explained by the increase in the amount of excess oxygen (interstitial oxygen). Since the stable valence state of Fe is +3, the concentration of Ni³⁺ decreased by substitution with Fe. Therefore the oxygen vacancies increase by the charge neutralization reaction.

The oxygen permeation in K₂NiF₄-type materials is controlled by oxide ion conductivity [51] which related to the diffusion of interstitial oxygen mainly occurring in the rock-salt layer (interstitial mechanism) and the transport of oxide ion via vacancies in the perovskite layer (vacancy mechanism) [52] as displayed in Figure 3.14. Therefore, the highest oxygen permeation rate is associated with both oxygen vacancy and interstitial oxygen.

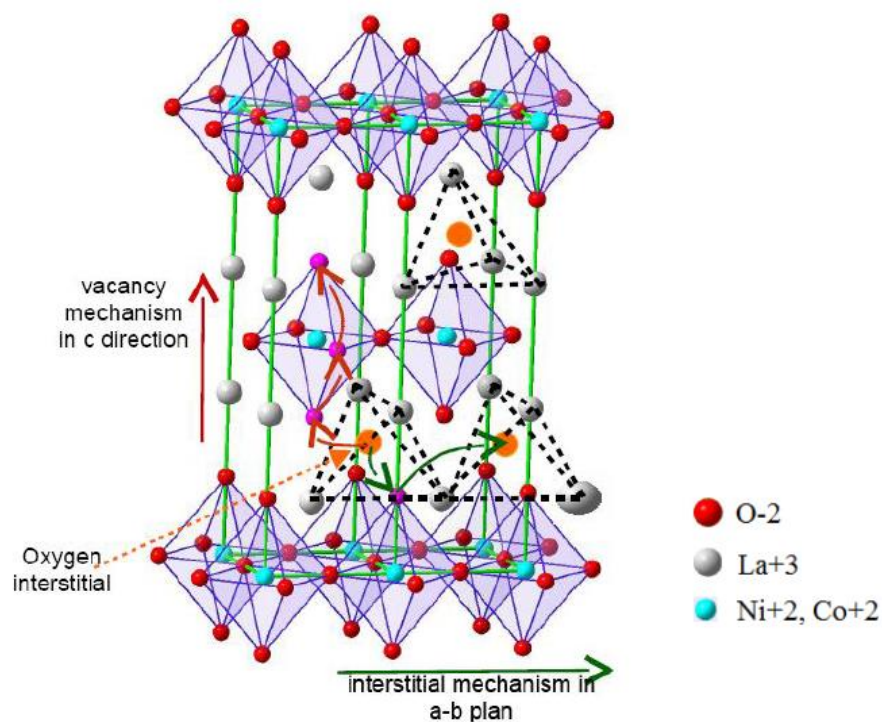


Figure 3.14 Oxygen migration path in the a-b plane and c direction

3.5 Synthesis and properties of $\text{La}_{2-x}\text{Ca}_x\text{Ni}_{0.85}\text{Co}_{0.1}\text{M}_{0.05}\text{O}_4$ (M=Fe, Zn and x=0-0.7)

Based on oxygen permeation results, LNC-Fe_{0.05} and LNC-Zn_{0.05} provide the highest oxygen permeation rate in each series. Therefore calcium was then incorporated into both of them at La-site in order to improve the electrical conductivity.

3.5.1 XRD analyses

The XRD patterns of LNCF-Ca_x and LNCZ-Ca_x (x=0, 0.1, 0.3, 0.5 and 0.7) are presented in Figure 3.15 and 3.16, respectively. The phase is identified as K₂NiF₄-type with tetragonal structure. It is observed that all peaks shift to lower angle with increasing the calcium content compared to the undoped sample, indicating reduced lattice parameters as given in Table 3.10 and Table 3.11. This is due to the fact that substitution with smaller cation causes a reduction in lattice parameters. The samples with x=0-0.5 exhibit a pure phase without any impurity, while with higher Ca content (x=0.7), a small amount of CaO is observed. This suggests that the limitation of Ca addition is less than 0.7. Thus, LNCF-Ca_x and LNCZ-Ca_x which x=0-0.5 were selected for further study.



3914990606

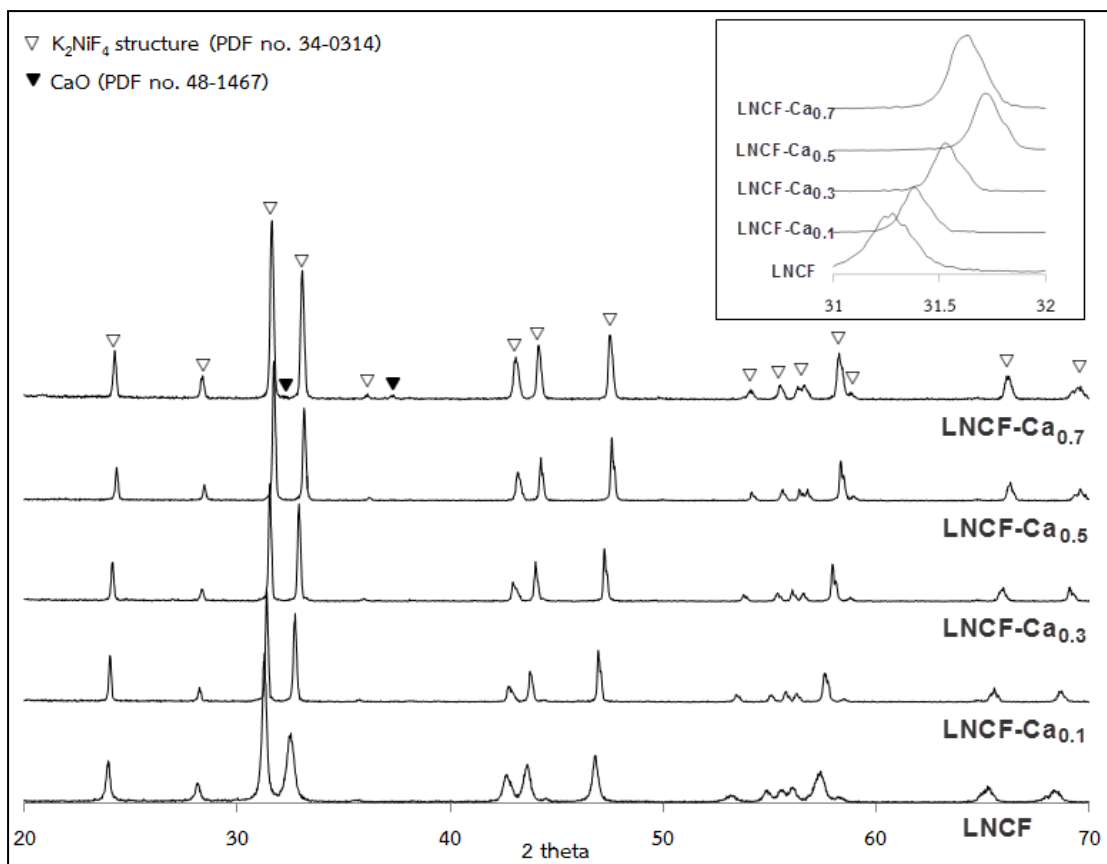


Figure 3.15 XRD patterns of LNCF- Ca_x discs sintered at 1350°C for 10 hours

Table 3.13 Lattice parameters and unit cell volume of LNCF- Ca_x

Compound	* Lattice parameter		$V (\text{\AA}^3)$
	$a (\text{\AA})$	$c (\text{\AA})$	
LNCF	3.885	12.682	191.41
LNCF- $Ca_{0.1}$	3.872	12.558	188.24
LNCF- $Ca_{0.3}$	3.849	12.573	186.24
LNCF- $Ca_{0.5}$	3.819	12.570	183.32
LNCF- $Ca_{0.7}$	3.826	12.496	182.87

*The average lattice parameter is calculated from the diffraction peaks of (101), (103), (110), (114) and (200) planes.

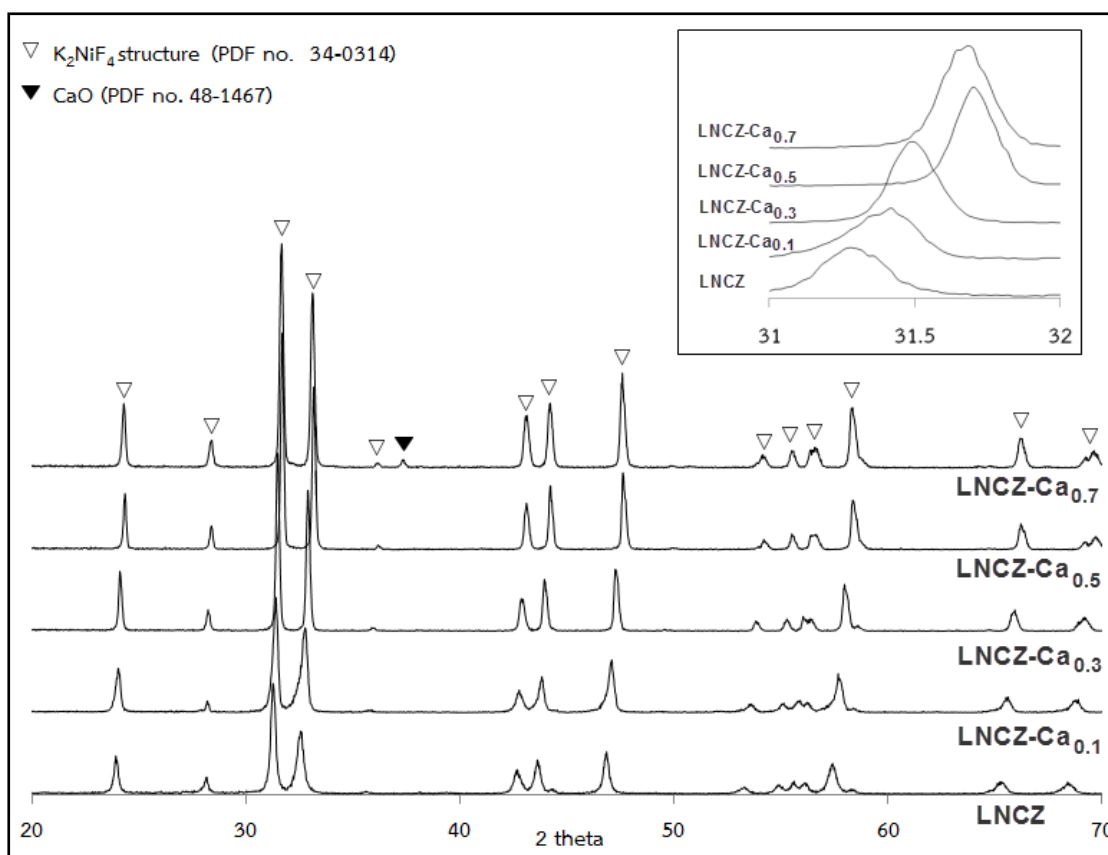


Figure 3.16 XRD patterns of LNCZ-Ca_x discs sintered at 1350°C for 10 hours

Table 3.14 Lattice parameters and unit cell volume of LNCZ-Ca_x

Compound	* Lattice parameter		V (Å ³)
	a (Å)	c (Å)	
LNCZ	3.888	12.719	192.23
LNCZ-Ca _{0.1}	3.871	12.649	189.57
LNCZ-Ca _{0.3}	3.846	12.593	186.28
LNCZ-Ca _{0.5}	3.817	12.510	182.25
LNCZ-Ca _{0.7}	3.823	12.497	182.67

*The average lattice parameter is calculated from the diffraction peaks of (101), (103), (110), (114) and (200) planes.

3.5.2 SEM analyses

Figure 3.17 presents the SEM images of LNCF- Ca_x and LNCZ- Ca_x ($x=0, 0.1, 0.3$ and 0.5). The microstructure of all samples indicates densified membranes. With increasing Ca content, the large grain size is obtained which is consistent with the result of relative density calculation in Table 3.15. The average grain size varies from 2.0 to $6.9 \mu\text{m}$ and the calculated density is over 95% . It can be seen that the grain size of the Ca-doped sample is higher than that of the undoped one, suggesting that the calcium dopant facilitates LNCF and LNCZ to form the dense microstructure.

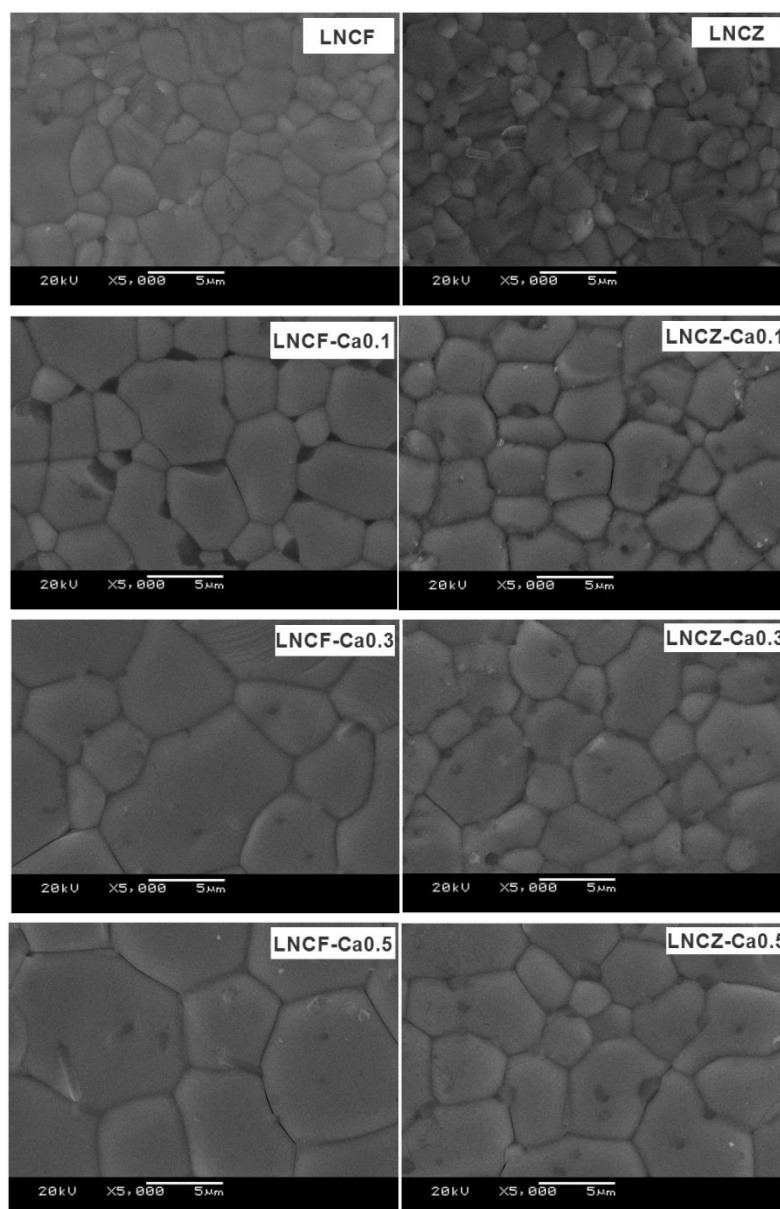


Figure 3.17 SEM images of LNCF- Ca_x and LNCZ- Ca_x ($x=0, 0.1, 0.3$ and 0.5) discs

Table 3.15 Average grain size and relative density of LNCF-Ca_x and LNCZ-Ca_x (x=0, 0.1, 0.3 and 0.5) discs

Sample	Grain size (μm)	Relative density (%)
LNCF	3.8	96.53
LNCF-Ca _{0.1}	4.8	97.21
LNCF-Ca _{0.3}	6.2	98.45
LNCF-Ca _{0.5}	6.9	98.46
LNCZ	2.0	96.44
LNCZ-Ca _{0.1}	4.0	96.78
LNCZ-Ca _{0.3}	4.2	97.45
LNCZ-Ca _{0.5}	5.1	97.69

3.5.3 Electrical conductivity analyses

Figure 3.18 and 3.19 displays the temperature dependence of the electrical conductivity of LNCF-Ca_x and LNCZ-Ca_x (x=0, 0.1, 0.3, 0.5 and 0.7) and the data are summarized in table 3.16 and 3.17, respectively.

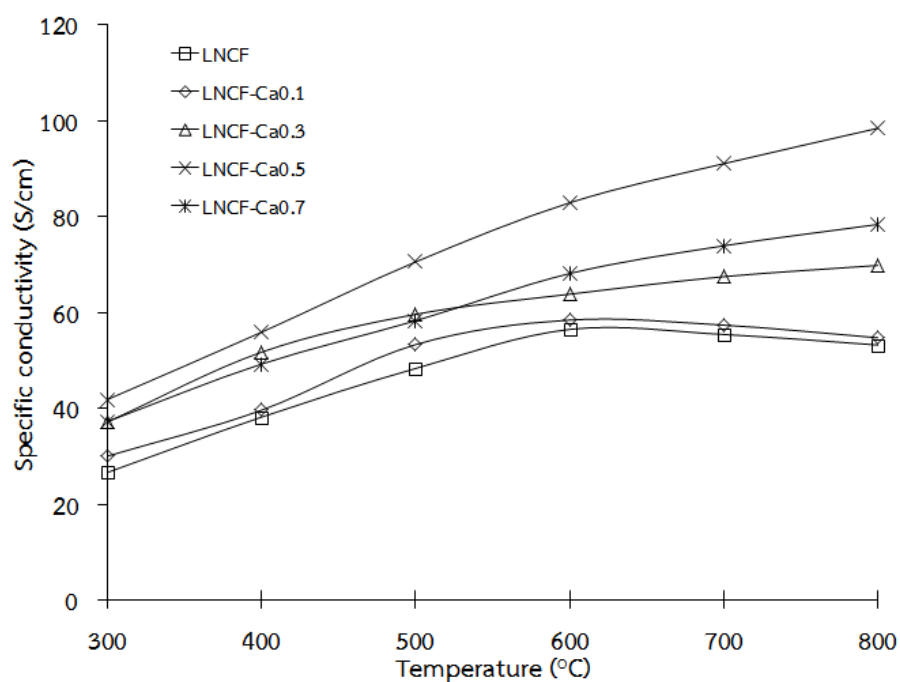
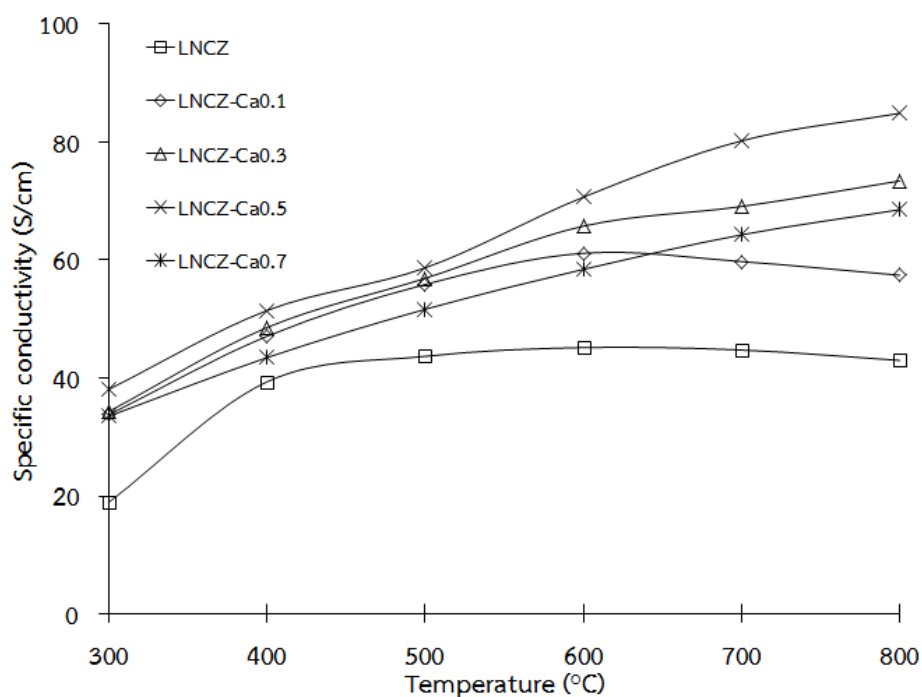


Figure 3.18 Temperature dependence of the specific conductivity (σ) of LNCF-Ca_x (x=0-0.7)

Table 3.16 The specific conductivity of LNCZ-Ca_x (x=0-0.7)

Sample	Specific conductivity (S/cm)						σ_{\max} (T, °C)
	300°C	400°C	500°C	600°C	700°C	800°C	
LNCZ	26.7	38.2	48.4	56.5	55.5	53.3	56.5 (600)
LNCZ-Ca _{0.1}	30.1	39.7	53.3	58.5	57.4	54.8	58.5 (600)
LNCZ-Ca _{0.3}	37.2	51.8	59.7	63.9	67.5	69.9	69.9 (800)
LNCZ-Ca _{0.5}	41.9	55.9	70.6	82.9	91.1	98.4	98.4 (800)
LNCZ-Ca _{0.7}	37.3	49.3	58.3	68.2	73.9	78.5	78.5 (800)

**Figure 3.19** Temperature dependence of the specific conductivity (σ) of LNCZ-Ca_x (x=0-0.7)**Table 3.17** The specific conductivity of LNCZ-Ca_x (x=0-0.7)

Sample	Specific conductivity (S/cm)						σ_{\max} (T, °C)
	300°C	400°C	500°C	600°C	700°C	800°C	
LNCZ	19.0	39.4	43.7	45.2	44.8	43.0	45.2 (600)
LNCZ-Ca _{0.1}	33.8	47.1	55.9	61.2	59.8	57.4	61.2 (600)
LNCZ-Ca _{0.3}	34.4	48.6	56.9	65.8	69.1	73.4	73.4 (800)
LNCZ-Ca _{0.5}	38.1	51.5	58.7	70.7	80.2	84.9	84.9 (800)
LNCZ-Ca _{0.7}	33.6	43.5	51.7	58.4	64.3	68.5	68.5 (800)

Both LNCf-Ca_x and LNCZ-Ca_x have the similar trend of electrical conductivity. For $x > 0.1$ the conductivity increases with temperature which indicates a semiconducting behavior in whole temperature range while for $x = 0$ and 0.1 the conductivity increases to the temperature of 600°C and remains constant afterwards. This suggests the semiconducting behavior only at low temperature. The conductivity do not increase at high temperature because of the reduction of B⁴⁺ to B³⁺ resulting in the creation of oxygen vacancies and the decreased covalency of B-O bonds [53].

In addition with increasing calcium substitution, the conductivity increases and achieves a maximum value at $x = 0.5$, and becomes decreasing with more calcium content ($x = 0.7$). The increased conductivity can be explained by the increase in B⁴⁺ cations caused by substitution of trivalent cation (La³⁺) with bivalent cation (Ca²⁺). On the other hand, the decreased conductivity when $x = 0.7$ may be due to the strain caused by high calcium content substituted into the lattice and the existence of impurity phase, CaO, which introduces scattering effect of the charge carrier [54]. It is observed that the maximum conductivity is 98.4 for S/cm for LNCf-Ca_{0.5} and 84.9 for LNCZ-Ca_{0.5} at 800°C. Therefore LNCf-Ca_{0.5} and LNCZ-Ca_{0.5} were selected to study the electrochemical properties in the next experiment.

3.6 Electrochemical analyses

LSN-Ca_{0.2}, LSNC-Ca_{0.2}, LNCf-Ca_{0.5} and LNCZ-Ca_{0.5} which had the highest electrical conductivity in each series were chosen to investigate the electrochemical properties. However before the electrochemical test, it is necessary to check the possible chemical reaction of cathode materials and electrolyte (LSGM) because the phase reaction occurring at the interface may create an insulating interfacial layer. This layer can block oxygen transfer between the cathode and electrolyte resulting in a decrease in cell performance [55].

3.6.1 Material compatibility

In order to check the compatibility between the cathode and the LSGM electrolyte, cathode materials and LSGM in 1:1 weight ratio were mixed together and then fired at 1000°C for 10 hours in air and determined the phase appeared by XRD technique.



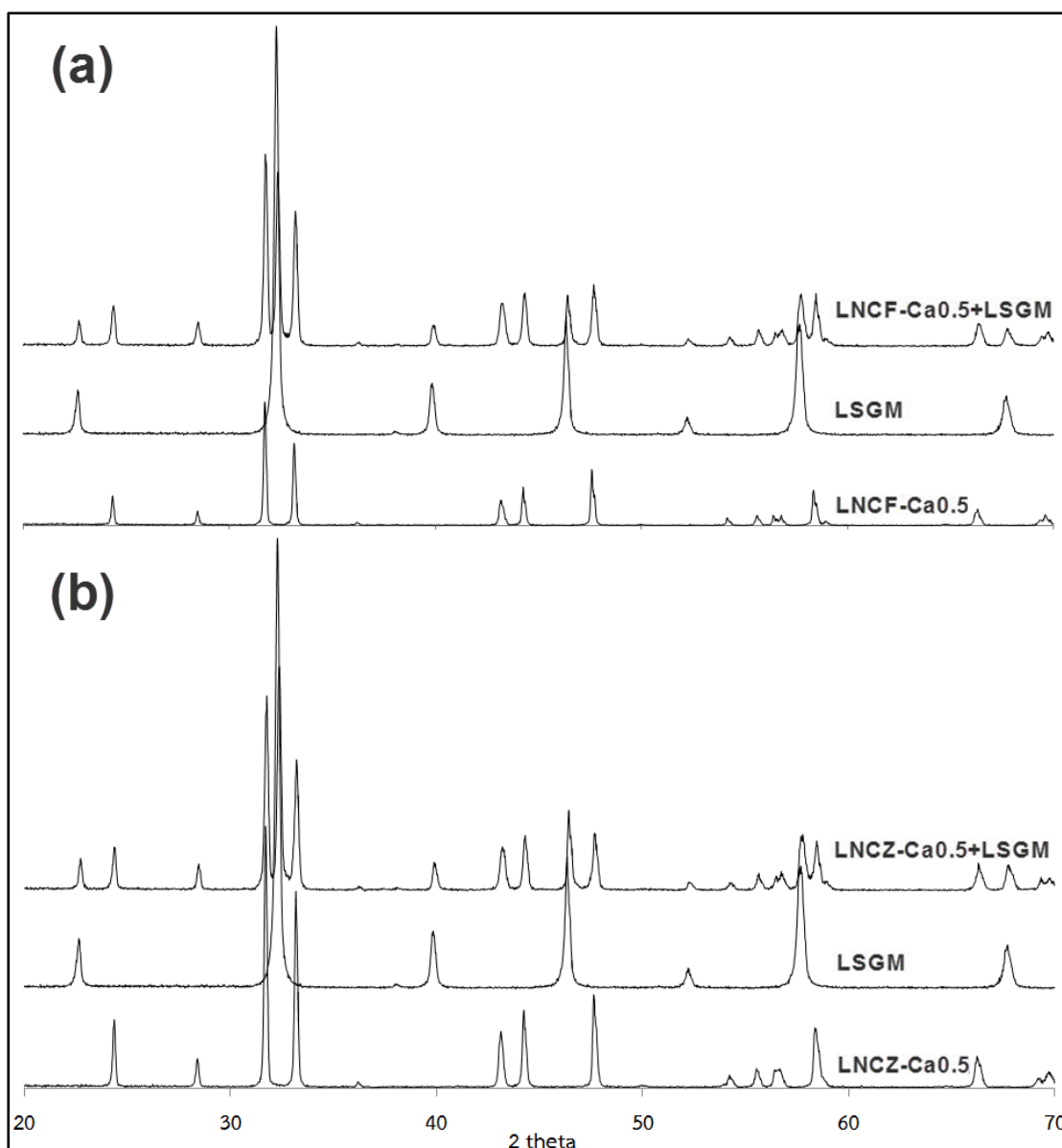


Figure 3.20 XRD patterns of LNCf-Ca_{0.5}-LSGM (a) and LNCZ-Ca_{0.5}-LSGM (b) mixtures after fired at 1000°C for 10 hours

For comparison, the XRD pattern of each cathode, LSGM and mixed cathode-LSGM are shown in Figure 3.20. It can be seen that the structure of the mixture is not changed and no new diffraction peaks are observed in LNCf-Ca_{0.5} and LNCZ-Ca_{0.5} suggesting that there are no serious reaction occurred between them. Therefore it is reasonable to conclude that LNCf-Ca_{0.5} and LNCZ-Ca_{0.5} are stable and do not react with LSGM electrolyte at 1000°C.

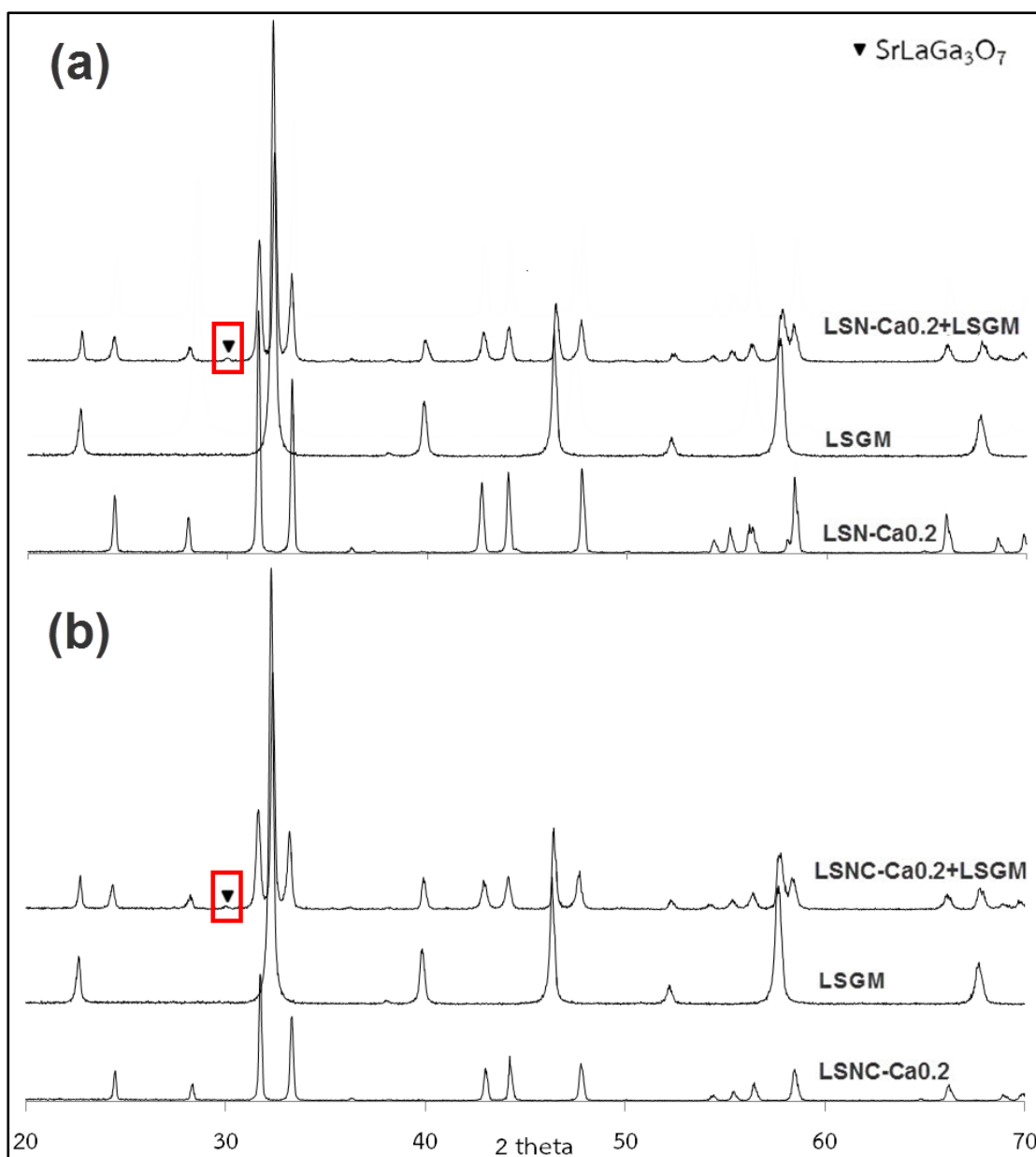


Figure 3.21 XRD patterns of LSN-Ca_{0.2}-LSGM (a) and LSNC-Ca_{0.2}-LSGM (b) mixtures after fired at 1000°C for 10 hours

In case of LSN-Ca_{0.2} and LSNC-Ca_{0.2}, a new small peak is observed at 2θ of 30 degree corresponding to SrLaGa₃O₇ (JCPDS 45-0637), indicating that they react with LSGM electrolyte to form a new phase at 1000°C. The reactivity of these materials leads to the negative effect on the cell performance. Therefore in order to avoid this unwanted phase, the compatibility at 950°C and 900°C was then studied.

XRD patterns of mixed powder of LSN-Ca_{0.2} and LSNC-Ca_{0.2} with LSGM electrolyte at 950°C and 900°C are presented in Figure 3.22-3.23. There is a new peak appeared at 2θ of 30 degree corresponding to SrLaGa₃O₇. It can be concluded that at 950°C and 900°C LSN-Ca_{0.2} and LSNC-Ca_{0.2} are unstable and react with LSGM electrolyte to form a resistance phase.

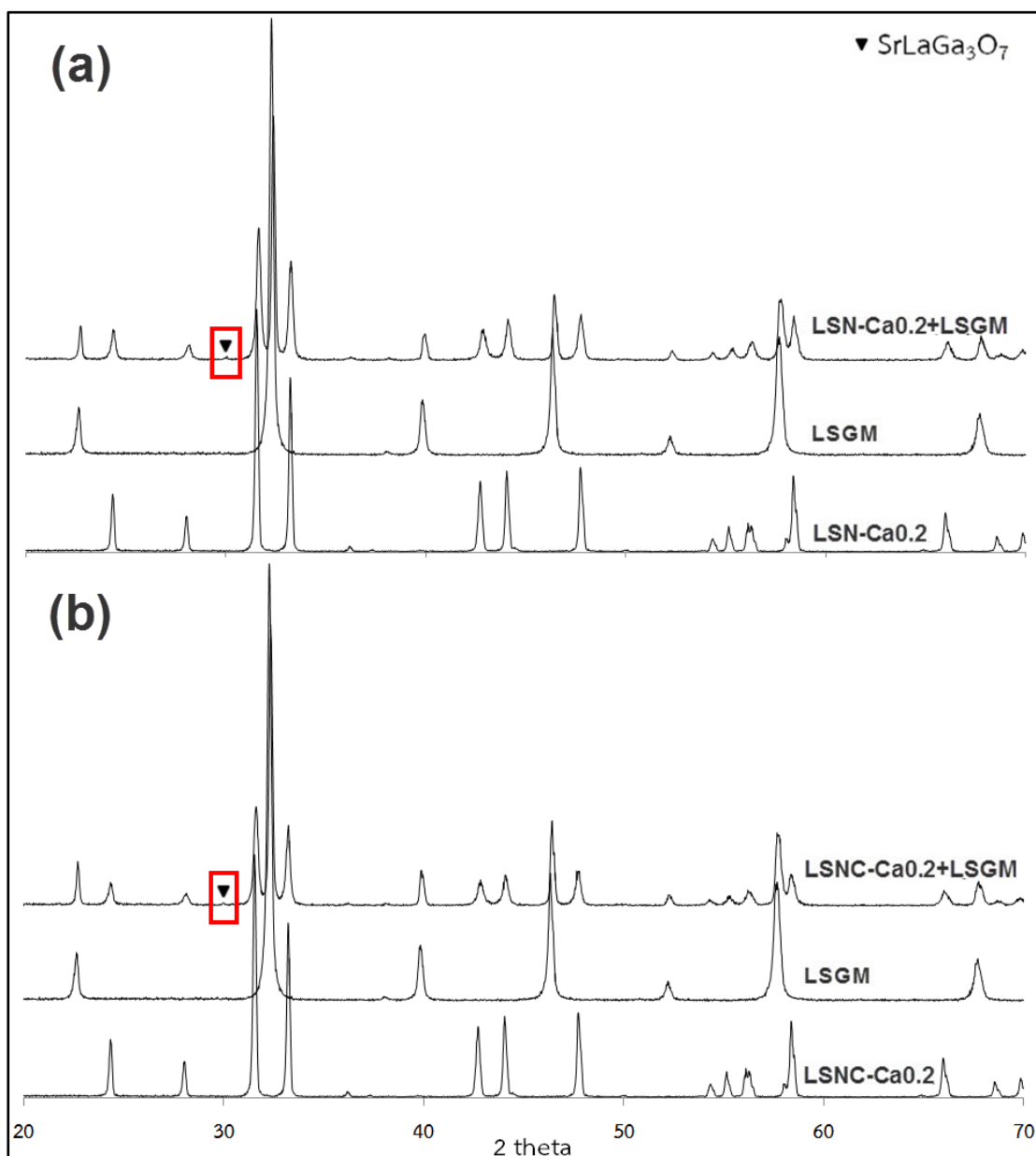


Figure 3.22 XRD patterns of LSN-Ca_{0.2}-LSGM (a) and LSNC-Ca_{0.2}-LSGM (b) mixtures after fired at 950°C for 10 hours

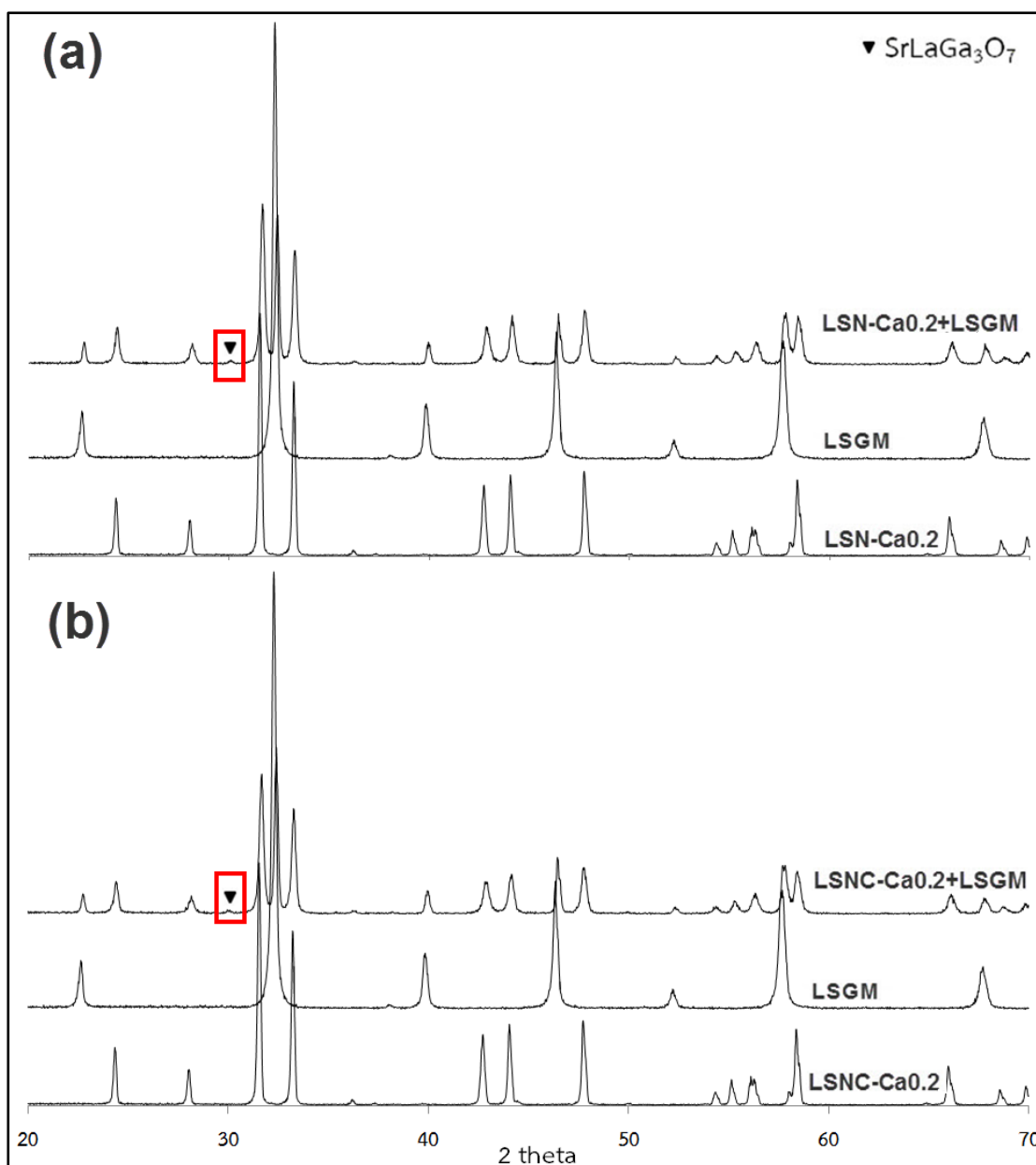


Figure 3.23 XRD patterns of LSN-Ca_{0.2}-LSGM (a) and LSNC-Ca_{0.2}-LSGM (b) mixtures after fired at 900°C for 10 hours

3.6.2 Impedance and single cell performance analyses

LNCF-Ca_{0.5} and LNCZ-Ca_{0.5} were chosen to study the electrochemical property with LSGM-supported single cell because they did not react with LSGM electrolyte at operating temperature. The polarization resistance and single cell performance in SOFC were measured at 800°C and 700°C. The impedance spectra, current-voltage and corresponding power density curves are displayed in Figure 3.24-3.25.

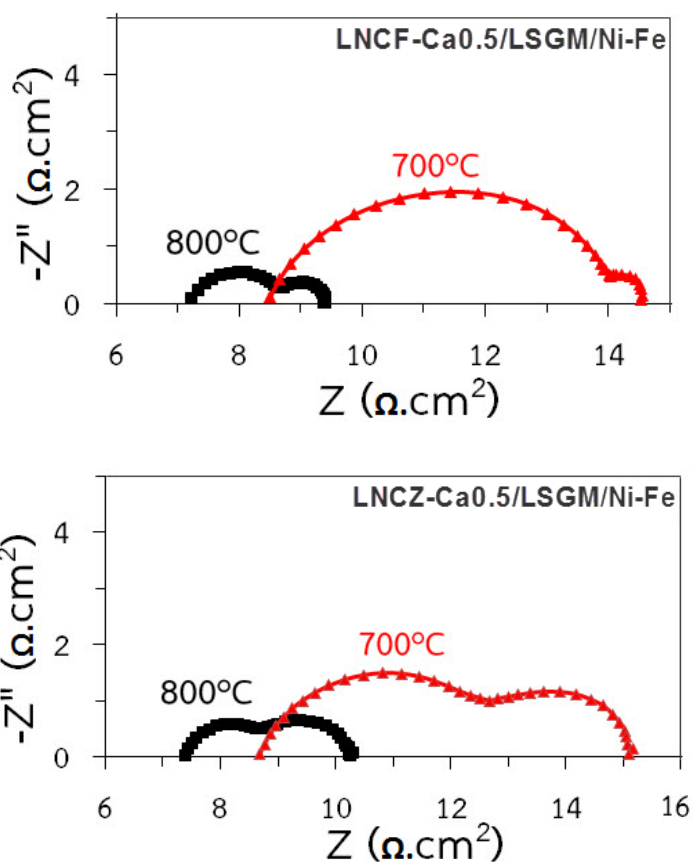


Figure 3.24 The AC impedance spectra of LNCf-Ca_{0.5}/LSGM/Ni-Fe and LNCZ-Ca_{0.5}/LSGM/Ni-Fe

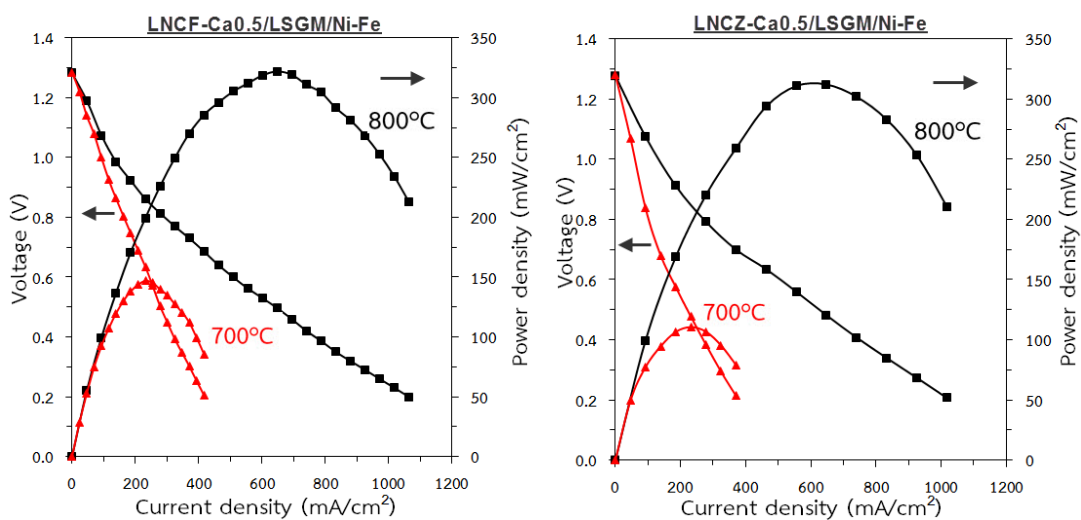


Figure 3.25 I-V curves and corresponding power density curves of LNCf-Ca_{0.5}/LSGM/Ni-Fe and LNCZ-Ca_{0.5}/LSGM/Ni-Fe

From Nyquist plot, it is found that all samples contain two separate arcs in each spectrum. This means that there are at least two electrode processes corresponding to the oxygen reduction reactions over the cell. The first arc at high frequency region is related to charge transfer reaction at electrode/electrolyte interface. While the other arc at low frequency region is related to the diffusion processes namely the oxygen adsorption/desorption on the cathode surface and the diffusion of oxygen ion [56]. The ohmic resistance (R_o) including the electrolyte, electrodes, current collectors and lead wires, is obtained from the intercept value at high frequency region with the real axis. The width between the high and the low frequency intercept is the polarization resistance (R_p) and the sum of R_o and R_p gives the total resistance of the cell [57-59]. For IT-SOFC, the cathode requires low polarization. It is observed that the obtained polarization resistance is in agreement with the data obtained from the cell performance test. The summarized total polarization resistances and power densities of each sample are listed in Table 3.18.

Table 3.18 Polarization resistance and power density of LNCF-Ca_{0.5}/LSGM/Ni-Fe and LNCZ-Ca_{0.5}/LSGM/Ni-Fe

Single cell	800°C		700°C	
	R_p ($\Omega \cdot \text{cm}^2$)	P (mW/cm ²)	R_p ($\Omega \cdot \text{cm}^2$)	P (mW/cm ²)
LNCF-Ca _{0.5} /LSGM/Ni-Fe	2.1	322	6.0	147
LNCZ-Ca _{0.5} /LSGM/Ni-Fe	2.9	312	6.4	111

It can be seen that the polarization resistance decreases with increasing operating temperature. Since at high temperature several processes such as migration of charge, gas transport and electrochemical reaction at TPB sites are enhanced resulting in the reduction of polarization resistance.

The maximum power density of the single cell with LNCF-Ca_{0.5} is slightly higher than LNCZ-Ca_{0.5}. This is possibly due to the fact that LNCF-Ca_{0.5} has the higher oxygen mobility compared to LNCZ-Ca_{0.5}, as seen in oxygen permeation results. With high oxygen diffusion properties, the oxygen rapidly transports through the material resulting in the enhancement of electrocatalytic properties. The maximum power densities of LNCF-Ca_{0.5} and LNCZ-Ca_{0.5} are 322 and 312 mW/cm², respectively. These value are higher than that of 226 mW/cm² at 800°C for La₂NiO₄ electrode on LSGM electrolyte reported by Escudero [29], suggesting that good performance can be

obtained for the single cell using LNCf-Ca_{0.5} and LNCZ-Ca_{0.5} as cathode and LSGM as electrolyte.



CHAPTER IV

CONCLUSION

4.1 Conclusion

The K_2NiF_4 -type oxide including $(La_{0.8}Sr_{0.2})_{2-x}Ca_xNiO_4$ (LSN- Ca_x , $x=0-0.5$), $(La_{0.8}Sr_{0.2})_{2-x}Ca_xNi_{0.9}Co_{0.1}O_4$ (LSNC- Ca_x , $x=0-0.5$) and $La_{2-x}Ca_xNi_{0.9-y}Co_{0.1}(Fe,Zn)_yO_4$ (LNCF- Ca_x and LNCZ- Ca_x , $y=0-0.2$, $x=0-0.7$) were prepared by modified citrate method with the calcination temperature of $900^\circ C$ and sintering temperature of $1350^\circ C$ for 10 hours. The compounds were characterized for phase structure, surface morphology, conducting property, oxygen permeation and electrochemical property.

All LSN- Ca_x and LSNC- Ca_x exhibited K_2NiF_4 -type with tetragonal structure. The pure single phase was obtained only for $x=0-0.2$ while at $x>0.2$ the formation of CaO impurity phase was observed. SEM images of sintered discs revealed that Ca^{2+} substitution promoted the higher grain size and the larger density of materials. Additionally, it resulted in an increase in electrical conductivity. The highest electrical conductivity values of 176.9 and 166.9 S/cm at $800^\circ C$ were achieved for LSN- $Ca_{0.2}$ and LSNC- $Ca_{0.2}$, respectively.

The incorporation of Fe and Zn at Ni-site of $La_2Ni_{0.9-y}Co_{0.1}(Fe,Zn)_yO_4$ (denoted as LNC- Fe_y and LNC- Zn_y) produced the single phase of K_2NiF_4 -type structure when $y\leq 0.05$. At $y>0.05$, La_2O_3 impurity phase was detected. The SEM analysis indicated that Fe and Zn substitution did not affect the grain size and the density of materials. However, it affected the oxygen permeation rate. The oxygen permeation rate increased with increasing Fe and Zn content. LNC- $Fe_{0.05}$ and LNC- $Zn_{0.05}$ showed the highest oxygen permeation rate of 0.57 and 0.41 $\mu mol/s.cm^2$ at $1000^\circ C$, respectively.

When substitution of Ca^{2+} ion at La-site of LNC- $Fe_{0.05}$ and LNC- $Zn_{0.05}$, the single phase of K_2NiF_4 -type structure was obtained at $x=0-0.5$ whereas at $x>0.5$, CaO impurity phase was appeared. The substitution of Ca^{2+} enhanced the material density confirmed by SEM images and increased the electrical conductivity of materials. The highest electrical conductivities were achieved for LNCF- $Ca_{0.5}$ and LNCZ- $Ca_{0.5}$ and the values were 98.4 and 84.9 S/cm, respectively at $800^\circ C$.

Electrochemical performance was determined for LNCF- $Ca_{0.5}$ /LSGM/Ni-Fe and LNCZ- $Ca_{0.5}$ /LSGM/Ni-Fe and the maximum power densities at $800^\circ C$ were 322 and 312, respectively.



3914990606

Based on the results, it can be concluded that substitution of Ca^{2+} ion at A-site and substitution of Fe and Zn at B-site can improve the electrical conductivity and the oxygen permeation of materials in this study. $\text{LNCF-Ca}_{0.5}$ and $\text{LNCZ-Ca}_{0.5}$ are interesting materials for using as cathode in IT-SOFC because of its high single cell performance with LSGM electrolyte.

4.2 Suggestions

- 1) To study the single cell performance of $\text{LSN-Ca}_{0.2}$ and $\text{LSNC-Ca}_{0.2}$ using another electrolyte, with gadolinium- or samarium-doped ceria being an example.
- 2) To study the long-term stability test of the single cell.
- 3) To investigate other properties such as structural property and thermal expansion coefficient (TEC) in order to obtain more details of materials.



REFERENCES

- [1] Song, C. Fuel processing for low-temperature and high-temperature fuel cells Challenges, and opportunities for sustainable development in the 21st century. Catalysis Today 77 (2002): 17-49.
- [2] Haile, S.M. Fuel cell Materials and components. Acta Materialia 51(19) (2003): 5981-6000.
- [3] Brett, D.J., Atkinson, A., Brandon, N.P., and Skinner, S.J. Intermediate temperature solid oxide fuel cells. Chemical Society Reviews 37(8) (2008): 1568-78.
- [4] Jacobson, A.J. Materials for Solid Oxide Fuel Cells. Chemistry of Materials 22(3) (2010): 660-674.
- [5] Cong, L., He, T., Ji, Y., Guan, P., Huang, Y., and Su, W. Synthesis and characterization of IT-electrolyte with perovskite structure. Journal of Alloys and Compounds 348 (2003): 325–331.
- [6] Hayashi, H., et al. Thermal expansion of Gd-doped ceria and reduced ceria. Solid State Ionics 132 (2000): 227–233.
- [7] Raghvendra, Kumar Singh, R., and Singh, P. Synthesis of $\text{La}_{0.9}\text{Sr}_{0.1}\text{Ga}_{0.8}\text{Mg}_{0.2}\text{O}_{3-\delta}$ electrolyte via ethylene glycol route and its characterizations for IT-SOFC. Ceramics International 40(5) (2014): 7177-7184.
- [8] Sammes, N. Fuel cell technology. London: Springer, 2006.
- [9] Sayers, R. and Skinner, S.J. Evidence for the catalytic oxidation of $\text{La}_2\text{NiO}_{4+\delta}$. Journal of Materials Chemistry 21(2) (2011): 414.
- [10] Singhal, S.C. Advances in solid oxide fuel cell technology. Solid State Ionics 135 (200): 305-313.
- [11] Aguadero, A., et al. Materials development for intermediate-temperature solid oxide electrochemical devices. Journal of Materials Science 47(9) (2012): 3925-3948.
- [12] Fergus, J.W. Solid oxide fuel cells: materials properties and performance. Boca Raton: CRC Press, 2009.
- [13] Sharma, I.B. and Singh, D. Solid state chemistry of Ruddlesden-Popper type complex oxides. The Bulletin of Materials Science 21 (1998): 363-374.
- [14] Tarancón, A., Burriel, M., Santiso, J., Skinner, S.J., and Kilner, J.A. Advances in layered oxide cathodes for intermediate temperature solid oxide fuel cells. Journal of Materials Chemistry 20(19) (2010): 3799.



3914990606

- [15] Bhavaraju, S. Electrochemical Intercalation of Oxygen in A_2BO_4 Oxides. Doctoral dissertation, Faculty of the Department of Chemistry University of Houston, 1996.
- [16] Zhang, K., et al. Research progress and materials selection guidelines on mixed conducting perovskite-type ceramic membranes for oxygen production. RSC Advances 1(9) (2011): 1661.
- [17] Xu, N., et al. Dependence of critical radius of the cubic perovskite ABO_3 oxides on the radius of A- and B-site cations. International Journal of Hydrogen Energy 35(14) (2010): 7295-7301.
- [18] Hui, S., et al. A brief review of the ionic conductivity enhancement for selected oxide electrolytes. Journal of Power Sources 172(2) (2007): 493-502.
- [19] Richter, J., Holtappels, P., Graule, T., Nakamura, T., and Gauckler, L.J. Materials design for perovskite SOFC cathodes. Monatshefte für Chemie-Chemical Monthly 140(9) (2009): 985-999.
- [20] Lashtabeg, A. and Skinner, S.J. Solid oxide fuel cells-a challenge for materials chemists? Journal of Materials Chemistry 16(31) (2006): 3161.
- [21] Huang, W. Interconnects for Intermediate Temperature Solid Oxide Fuel Cells. Doctoral dissertation, College of Engineering, Boston university, 2008.
- [22] Barsoukov, E. and Macdonald, J.R. Impedance spectroscopy, theory experiment and applications 2ed. Hoboken, New Jersey: A John Wiley & Sons, 2005.
- [23] Macdonald, J.R. Impedance Spectroscopy. Annals of Biomedical Engineering 20 (1992): 289-305.
- [24] Nakamura, T., Yashiro, K., Sato, K., and Mizusaki, J. Electronic state of oxygen nonstoichiometric $La_{2-x}Sr_xNiO_4$ at high temperatures. Phys.Chem. Chem.Phys. 11 (2009): 3055-3062.
- [25] Ratchaun, C. Preparation of $La_{2-x}Ca_xNi_{1-y}Co_y(Ga,Ti)zO_4$ for Solid Oxide Fuel Cells. Master's Thesis, Department of Chemistry, Faculty of Science, Chulalongkorn University, 2010.
- [26] Cherry, M., Islam, M.S., and Catlow, C.R.A. Oxygen ion migration in perovskite-type oxides. Journal of Solid State Chemistry 118 (1995): 125-132.
- [27] Yang, J., Cheng, J., Jiang, Q., Wang, Y., Wang, R., and Gao, J. Preparation and electrochemical properties of strontium doped Pr_2NiO_4 cathode materials for intermediate-temperature solid oxide fuel cells. International Journal of Hydrogen Energy 37(2) (2012): 1746-1751.



- [28] Zhao, F., Wang, X., Wang, Z., Peng, R., and Xia, C. K_2NiF_4 type $La_{2-x}Sr_xCo_{0.8}Ni_{0.2}O_{4+\delta}$ as the cathodes for solid oxide fuel cells. *Solid State Ionics* 179(27-32) (2008): 1450-1453.
- [29] Shen, Y., Zhao, H., Liu, X., and Xu, N. Preparation and electrical properties of Ca-doped La_2NiO_4 cathode materials for IT-SOFC. *Physical Chemistry Chemical Physics* 12(45) (2010): 15124-31.
- [30] Ding, X., Gao, L., Liu, Y., Zhen, Y., and Guo, L. Thermal expansion and electrochemical properties of $La_{0.7}AE_{0.3}CuO_{3-\delta}$ (AE=Ca, Sr, Ba) cathode materials for IT-SOFCs. *Journal of Electroceramics* 18(3-4) (2007): 317-322.
- [31] Chen, X., Liu, H., Wei, Y., Caro, J., and Wang, H. A novel zincum-doped perovskite-type ceramic membrane for oxygen separation. *Journal of Alloys and Compounds* 484(1-2) (2009): 386-389.
- [32] Park, J., Zou, J., Yoon, H., Kim, G., and Chung, J.S. Electrochemical behavior of $Ba_{0.5}Sr_{0.5}Co_{0.2-x}Zn_xFe_{0.8}O_{3-\delta}$ ($x = 0-0.2$) perovskite oxides for the cathode of solid oxide fuel cells. *International Journal of Hydrogen Energy* 36(10) (2011): 6184-6193.
- [33] Kostogloudis, G.C. and Ftikos, C. Oxygen nonstoichiometry in $Pr_{1-x}Sr_xCo_{0.2}B_{0.8}O_{3-\delta}$ (B=Mn, Fe, $x=0.2, 0.4$) perovskite oxides. *Journal of the European Ceramic Society* 27(1) (2007): 273-277.
- [34] Petitjean, M., Caboche, G., Siebert, E., Dessemond, L., and Dufour, L.C. $(La_{0.8}Sr_{0.2})(Mn_{1-y}Fe_y)O_{3-\delta}$ oxides for ITSOFC cathode materials? *Journal of the European Ceramic Society* 25(12) (2005): 2651-2654.
- [35] Miyoshi, S., Furuno, T., Matsumoto, H., and Ishihara, T. Conductivity and oxygen permeability of a novel oxide $Pr_2Ni_{0.8-x}Cu_{0.2}Fe_xO_4$ and its application to partial oxidation of CH₄. *Solid State Ionics* 177(26-32) (2006): 2269-2273.
- [36] Ishihara, T., Matsuda, H., and Takita, Y. Doped $LaGaO_3$ perovskite type oxide as a new oxide ionic conductor. *Journal of the American Chemical Society* 116 (1994): 3801-3803.
- [37] Ju, Y.-W., Eto, H., Inagaki, T., Ida, S., and Ishihara, T. Preparation of Ni-Fe bimetallic porous anode support for solid oxide fuel cells using $LaGaO_3$ based electrolyte film with high power density. *Journal of Power Sources* 195(19) (2010): 6294-6300.
- [38] Hsieh, T.H., Jhong, F.H., Ray, D.T., and Fu, Y.P. Electrical properties of $(La_{0.9}Ca_{0.1})(Co_{1-x}Ni_x)O_{3-\delta}$ cathode materials for SOFCs. *Ceramics International* 38(3) (2012): 1785-1791.



- [39] Magnone, E., Miyayama, M., and Traversa, E. Some structural considerations on the perovskite-type $A_{1-y}SryCo_{1-x}Fe_xO_{3-\delta}$ solid solution series. Crystal Research and Technology 45(4) (2010): 355-364.
- [40] Li-Ping, S., et al. Synthesis and performance of $Sr_{1.5}La_xMnO_4$ as cathode materials for intermediate temperature solid oxide fuel cell. Journal of Power Sources 196(14) (2011): 5835-5839.
- [41] Ruck, K., Krabbes, G., and Vogel, I. Structural and electrical properties of $La_{2-x}Ca_xNiO_{4+\delta}$ ($0 < x < 0.4$) with regard to the oxygen content Materials Research Bulletin 34 (1999): 1689-1697.
- [42] Riza, F. and Ftikos, C. Influence of A- and B-site doping on the properties of the system $La_2CoO_{4+\delta}$. Journal of the European Ceramic Society 27(2-3) (2007): 571-573.
- [43] Zhao, H., Shen, W., Zhu, Z., Li, X., and Wang, Z. Preparation and properties of $Ba_xSr_{1-x}Co_yFe_{1-y}O_{3-\delta}$ cathode material for intermediate temperature solid oxide fuel cells. Journal of Power Sources 182(2) (2008): 503-509.
- [44] Xiao, G., et al. Synthesis and characterization of Mo-doped $SrFeO_{3-\delta}$ as cathode materials for solid oxide fuel cells. Journal of Power Sources 202 (2012): 63-69.
- [45] Shen, Y., Zhao, H., Xu, J., Zhang, X., Zheng, K., and Świerczek, K. Effect of ionic size of dopants on the lattice structure, electrical and electrochemical properties of $La_{2-x}M_xNiO_{4+\delta}$ ($M = Ba, Sr$) cathode materials. International Journal of Hydrogen Energy 39(2) (2014): 1023-1029.
- [46] Jammali, M., Chaker, H., Cherif, K., and Ben Hassen, R. Investigation on the structural and electrical properties of $NdSrNi_{1-x}Cr_xO_{4+\delta}$ ($0.1 \leq x \leq 0.9$) system. Journal of Solid State Chemistry 183(5) (2010): 1194-1199.
- [47] Boehm, E., Bassat, J., Dordor, P., Mauvy, F., Grenier, J., and Stevens, P. Oxygen diffusion and transport properties in non-stoichiometric $LnNiO$ oxides. Solid State Ionics 176(37-38) (2005): 2717-2725.
- [48] Kharton, V.V., et al. Mixed conductivity, oxygen permeability and redox behavior of K_2NiF_4 -type $La_2Ni_{0.9}Fe_{0.1}O_{4+\delta}$. Journal of Solid State Chemistry 181(6) (2008): 1425-1433.
- [49] Tsipis, E. Oxygen nonstoichiometry and ionic transport in $La_2Ni(Fe)O_{4+\delta}$. Solid State Ionics 179(1-6) (2008): 57-60.
- [50] Lu, H., Tong, J., Deng, Z., Cong, Y., and Yang, W. Crystal structure, oxygen permeability and stability of $Ba_{0.5}Sr_{0.5}Co_{0.8}Fe_{0.1}M_{0.1}O_{3-\delta}$ ($M=Fe, Cr, Mn, Zr$)



- oxygen-permeable membranes. Materials Research Bulletin 41(4) (2006): 683-689.
- [51] Ishihara, T., Nakashima, K., Okada, S., Enoki, M., and Matsumoto, H. Defect chemistry and oxygen permeation property of $\text{Pr}_2\text{Ni}_{0.75}\text{Cu}_{0.25}\text{O}_4$ oxide doped with Ga. Solid State Ionics 179(27-32) (2008): 1367-1371.
- [52] Zhao, H., Li, Q., and Sun, L. Ln_2MO_4 cathode materials for solid oxide fuel cells. Science China Chemistry 54(6) (2011): 898-910.
- [53] Zhou, W., et al. Barium- and strontium-enriched $(\text{Ba}_{0.5}\text{Sr}_{0.5})_{1+x}\text{Co}_{0.8}\text{Fe}_{0.2}\text{O}_{3-\delta}$ oxides as high-performance cathodes for intermediate-temperature solid-oxide fuel cells. Acta Materialia 56(12) (2008): 2687-2698.
- [54] Jiang, S.P., Liu, L., Ong, K.P., Wu, P., Li, J., and Pu, J. Electrical conductivity and performance of doped LaCrO_3 perovskite oxides for solid oxide fuel cells. Journal of Power Sources 176(1) (2008): 82-89.
- [55] Chen, D., Ran, R., Zhang, K., Wang, J., and Shao, Z. Intermediate-temperature electrochemical performance of a polycrystalline $\text{PrBaCo}_2\text{O}_{5+\delta}$ cathode on samarium-doped ceria electrolyte. Journal of Power Sources 188(1) (2009): 96-105.
- [56] Cao, Y., Gu, H., Chen, H., Zheng, Y., Zhou, M., and Guo, L. Preparation and characterization of $\text{Nd}_{2-x}\text{Sr}_x\text{CoO}_{4+\delta}$ cathodes for intermediate-temperature solid oxide fuel cell. International Journal of Hydrogen Energy 35(11) (2010): 5594-5600.
- [57] Li, Q., Zhao, H., Huo, L., Sun, L., Cheng, X., and Grenier, J.-C. Electrode properties of Sr doped La_2CuO_4 as new cathode material for intermediate-temperature SOFCs. Electrochemistry Communications 9(7) (2007): 1508-1512.
- [58] Ding, H., Xue, X., Liu, X., and Meng, G. A novel layered perovskite cathode for proton conducting solid oxide fuel cells. Journal of Power Sources 195(3) (2010): 775-778.
- [59] Li, Q., Zeng, X., Sun, L., Zhao, H., Huo, L., and Grenier, J.-C. Electrochemical performance of $\text{La}_2\text{Cu}_{1-x}\text{Co}_x\text{O}_4$ cathode materials for intermediate-temperature SOFCs. International Journal of Hydrogen Energy 37(3) (2012): 2552-2558.
- [60] Shannon, R.D. Revised effective ionic radii and systematic studies of interatomic distances in halides and chalcogenides. Acta Crystallographica A32 (1976): 751-767.





391 4990606

APPENDICES

APPENDIX A

Tolerance number

The Goldschmidt tolerance numbers were calculated based on equation A.1.

$$t = \frac{(r_A + r_O)}{\sqrt{2} \times (r_B + r_O)} \quad (\text{A.1})$$

where r_A , r_B and r_O represent the ionic crystal radii of A-site cation, B-site cation and oxygen ion, respectively. The example of the tolerance number calculation of La_2NiO_4 was showed as below.

$$\text{Tolerance number of } \text{La}_2\text{NiO}_4 = \frac{[(1.356 \times 2)/2 + 1.26]}{\sqrt{2} (0.83 + 1.26)} = 0.885$$

Table A.1 Ionic crystal radii of concerned metal ions [60]

Metal ion	Ionic charge	Coordination No.	Crystal radius (Å)
La	3+	9	1.356
Sr	2+	9	1.45
Ca	2+	9	1.32
Ni	2+	6	0.83
	3+ (LS)		0.7
	3+ (HS)		0.74
	4+ (LS)		0.62
	4+ (HS)		0.67
Co	2+ (LS)	6	0.79
	2+ (HS)		0.885
	3+ (LS)		0.685
	3+ (HS)		0.75
	4+ (HS)		0.67
Fe	2+ (LS)	6	0.75
	2+ (HS)		0.92
	3+ (LS)		0.69
	3+ (HS)		0.785
	4+		0.725
Zn	2+	6	0.88
O	2-	6	1.26

LS = Low spin configuration, HS = High spin configuration



3914990606

APPENDIX B

Activation energy (E_a)

Arrhenius equation (B.1) is shown below. The plot of $\ln(\sigma T)$ versus $\frac{1000}{T}$ (K) gives a straight line, whose slope can be used to determine the E_a of small polaron conduction.

$$\begin{aligned}\sigma &= \left(\frac{A}{T}\right) e^{\frac{-E_a}{RT}} \\ \ln(\sigma T) &= \ln A e^{\frac{-E_a}{RT}} \\ \ln(\sigma T) &= \ln e^{\frac{-E_a}{RT}} + \ln A \\ \ln(\sigma T) &= \left(\frac{-E_a}{R}\right) \left(\frac{1000}{T}\right) + \ln A \quad (B.1) \\ \downarrow \quad \downarrow \quad \downarrow \quad \downarrow \\ y \quad \text{slope} \quad x \quad \text{in intercept y axis}\end{aligned}$$

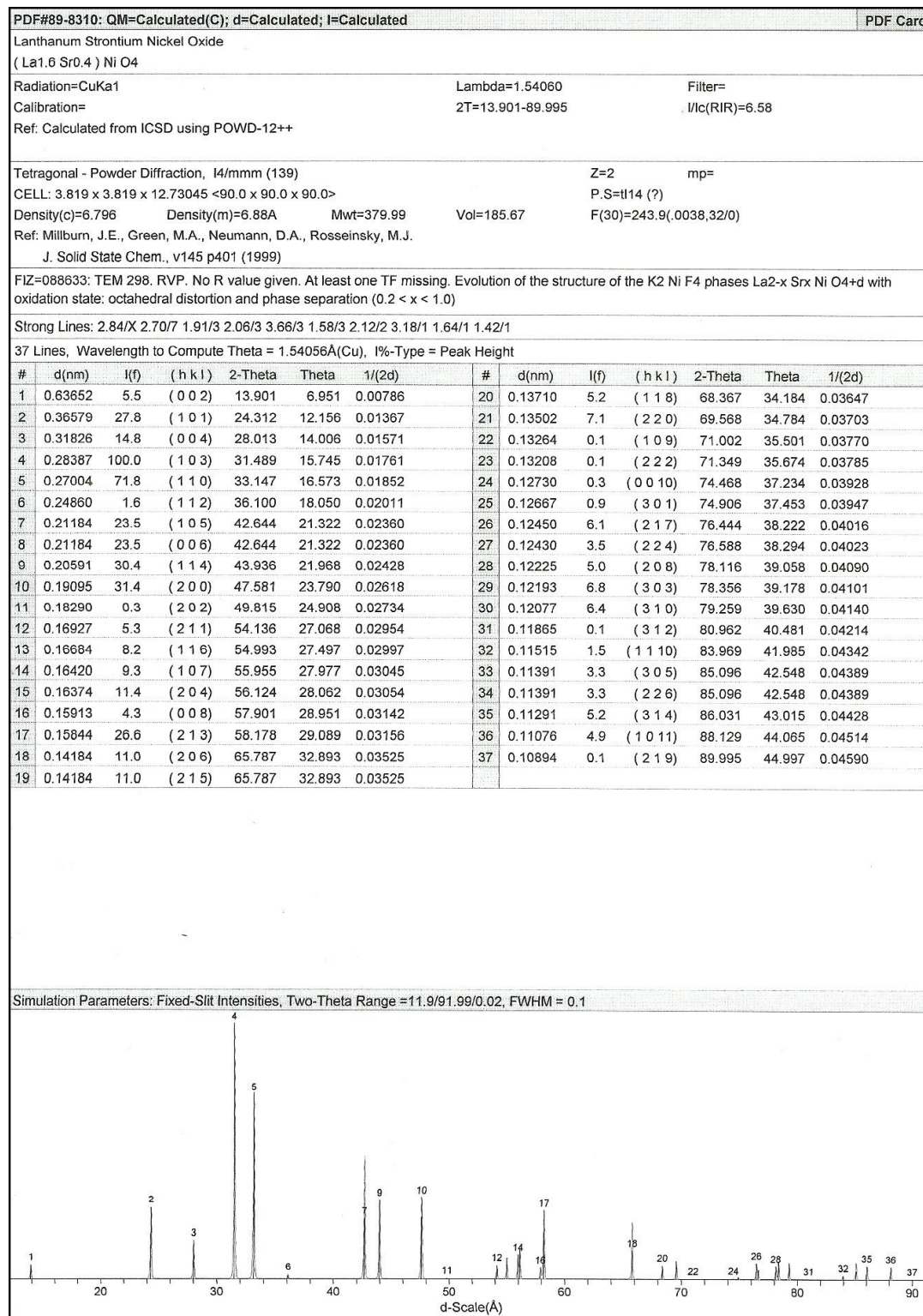
$$\begin{aligned}\left(\frac{-E_a}{R}\right) &= \text{slope of the linear} \\ E_a &= -\text{slope} \times R\end{aligned}$$

Where A = material constant including the carrier concentration term
 σ = specific conductivity (S/cm)
 E_a = activation energy (kJ/mol)
T = temperature (K)
R = gas constant = 8.314472 J/K.mol



APPENDIX C

XRD Data

 $(La_{1.6}Sr_{0.4})NiO_4$ PDF#89-8310

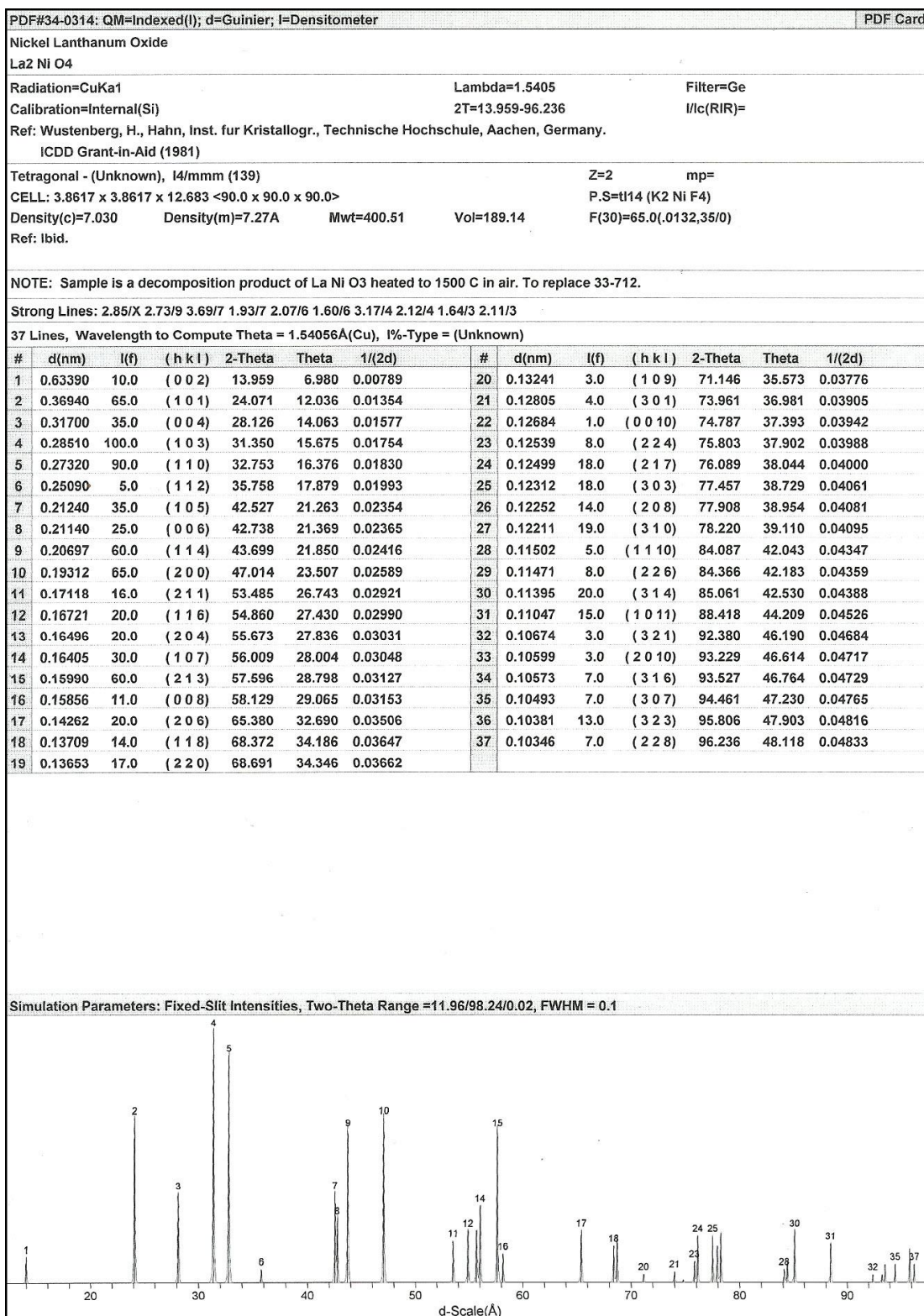
3914990606

CaO PDF#48-1467

PDF#48-1467: QM=Calculated(C); d=Calculated; I=Calculated													PDF Card
Calcium Oxide													(pEXC)
Ca O													
Radiation=CuKa1				Lambda=1.5405981				Filter=					
Calibration=				2T=32.199-147.782				I/c(RIR)=4.45					
Ref: Reardon, B., Hubbard, C., TM-11948.													
Oak Ridge Natl. Lab. Rep. ORNL (U.S.) (1992)													
Cubic - (Unknown), Fm-3m (225)						Z=4		mp=					
CELL: 4.81059 x 4.81059 x 4.81059 <90.0 x 90.0 x 90.0>													
Density(c)=3.345			Density(m)=2.59A			Mwt=56.08		Vol=111.33		F(13)=411.2(.0024,13/0)			
Ref: McMurdie, H.													
Powder Diffraction, v1 p265 (1986)													
NOTE: See also 37-1497.													
Strong Lines: 2.41/X 1.70/5 2.78/4 0.80/2 1.45/2 0.81/2 1.39/1 1.08/1 0.98/1 1.10/1													
13 Lines, Wavelength to Compute Theta = 1.54056Å(Cu), I%-Type = Peak Area													
#	d(nm)	I(f)	(h k l)	2-Theta	Theta	1/(2d)	#	d(nm)	I(f)	(h k l)	2-Theta	Theta	1/(2d)
1	0.27777	40.0	(1 1 1)	32.199	16.100	0.01800	8	0.10757	14.0	(4 2 0)	91.467	45.733	0.04648
2	0.24051	100.0	(2 0 0)	37.359	18.680	0.02079	9	0.09820	11.0	(4 2 2)	103.336	51.668	0.05092
3	0.17008	51.0	(2 2 0)	53.859	26.929	0.02940	10	0.09258	7.0	(5 1 1)	112.616	56.308	0.05401
4	0.14504	17.0	(3 1 1)	64.158	32.079	0.03447	11	0.08504	5.0	(4 4 0)	129.853	64.926	0.05879
5	0.13887	14.0	(2 2 2)	67.378	33.689	0.03601	12	0.08131	15.0	(5 3 1)	142.633	71.316	0.06149
6	0.12026	5.0	(4 0 0)	79.658	39.829	0.04158	13	0.08018	19.0	(4 4 2)	147.782	73.891	0.06236
7	0.11036	7.0	(3 3 1)	88.527	44.263	0.04531							
Simulation Parameters: Fixed-Slit Intensities, Two-Theta Range =30.2/149.78/0.02, FWHM = 0.1													



3914990606

La₂NiO₄ PDF#34-0314

3914990606

La₂O₃ PDF#05-0602

PDF#05-0602: QM=Star(S); d=(Unknown); i=Diffractometer													PDF Card	
Lanthanum Oxide													(cSCR)	
La ₂ O ₃														
Radiation=CuKα1				Lambda=1.5405				Filter=Ni						
Calibration=				2T=26.110-148.312				I/Ic(RIR)=						
Ref: Swanson, Fuyat. Natl. Bur. Stand. (U.S.), Circ. 539, vIII p33 (1954)														
Hexagonal - Powder Diffraction, P-3m1 (164)						Z=1		mp=						
CELL: 3.9373 x 3.9373 x 6.1299 <90.0 x 90.0 x 120.0>						P.S=hP5 (La ₂ O ₃)								
Density(c)=6.573		Density(m)=6.22A		Mwt=325.81		Vol=82.30		F(30)=46.8(.0160,40/0)						
Ref: Ibid.														
NOTE: Sample from Fairmount Chemical Company. Spectroscopic analysis: <0.01% Ca, Mg, Si; <0.001% Al, Cu, Fe, Pb. Pattern taken at 26 C. Sample was annealed at 1200 C for one hour and mounted in petrolatum to prevent reabsorption of C O ₂ + H ₂ O. Merck Index, 8th Ed., p. 608. Opaque mineral optical data on specimen from Nanseke, Uganda: R3R%=14.2, Disp.=Std. VHN100=782-813. Pattern reviewed by Holzer, J., McCarthy, G., North Dakota State Univ., Fargo, North Dakota, USA, ICDD Grant-in-Aid (1990). Validated by calculated pattern except for the following: 2.278 23 102; 1.968 28 110; 1.753 23 103. Calculated pattern indicates that the following reflections might be observable: 6.130 <1 001; 2.043 <1 003; 1.8744 <1 111; 1.4177 <1 113; 1.2260 <1 005.														
Color: Colorless														
Strong Lines: 2.98/X 1.97/6 2.28/6 1.75/5 3.41/3 3.06/3 1.66/2 1.64/2 1.26/1 1.31/1														
39 Lines, Wavelength to Compute Theta = 1.54056Å(Cu), I%-Type = (Unknown)														
#	d(nm)	I(f)	(h k l)	2-Theta	Theta	1/(2d)	#	d(nm)	I(f)	(h k l)	2-Theta	Theta	1/(2d)	
1	0.34100	34.0	(1 0 0)	26.110	13.055	0.01466	21	0.10901	7.0	(2 1 3)	89.920	44.960	0.04587	
2	0.30630	31.0	(0 0 2)	29.130	14.565	0.01632	22	0.10658	4.0	(3 0 2)	92.560	46.280	0.04691	
3	0.29800	100.0	(1 0 1)	29.960	14.980	0.01678	23	0.10220	0.0	(0 0 6)	97.824	48.912	0.04892	
4	0.22780	58.0	(1 0 2)	39.527	19.764	0.02195	24	0.09952	3.0	(2 0 5)	101.428	50.714	0.05024	
5	0.19680	63.0	(1 1 0)	46.084	23.042	0.02541	25	0.09840	3.0	(2 2 0)	103.036	51.518	0.05081	
6	0.17530	52.0	(1 0 3)	52.132	26.066	0.02852	26	0.09787	1.0	(1 0 6)	103.820	51.910	0.05109	
7	0.17050	4.0	(2 0 0)	53.716	26.858	0.02933	27	0.09459	0.0	(3 1 0)	109.043	54.522	0.05286	
8	0.16560	24.0	(1 1 2)	55.439	27.720	0.03019	28	0.09372	3.0	(2 2 2)	110.550	55.275	0.05335	
9	0.16420	17.0	(2 0 1)	55.953	27.977	0.03045	29	0.09345	5.0	(3 1 1)	111.029	55.515	0.05350	
10	0.15320	3.0	(0 0 4)	60.370	30.185	0.03264	30	0.09131	2.0	(3 0 4)	115.042	57.521	0.05476	
11	0.14900	5.0	(2 0 2)	62.258	31.129	0.03356	31	0.09070	2.0	(1 1 6)	116.263	58.131	0.05513	
12	0.13980	2.0	(1 0 4)	66.870	33.435	0.03577	32	0.08883	5.0	(2 1 5)	120.256	60.128	0.05629	
13	0.13090	7.0	(2 0 3)	72.094	36.047	0.03820	33	0.08766	1.0	(2 0 6)	122.975	61.488	0.05704	
14	0.12890	2.0	(2 1 0)	73.393	36.697	0.03879	34	0.08583	4.0	(3 1 3)	127.649	63.825	0.05825	
15	0.12610	12.0	(2 1 1)	75.302	37.651	0.03965	35	0.08480	2.0	(1 0 7)	130.556	65.278	0.05896	
16	0.12090	6.0	(1 1 4)	79.155	39.578	0.04136	36	0.08443	1.0	(4 0 1)	131.659	65.829	0.05922	
17	0.11879	4.0	(2 1 2)	80.848	40.424	0.04209	37	0.08283	2.0	(2 2 4)	136.855	68.427	0.06036	
18	0.11538	4.0	(1 0 5)	83.765	41.882	0.04334	38	0.08050	1.0	(3 1 4)	146.222	73.111	0.06211	
19	0.11396	2.0	(2 0 4)	85.051	42.526	0.04388	39	0.08007	2.0	(2 1 6)	148.312	74.156	0.06245	
20	0.11367	4.0	(3 0 0)	85.320	42.660	0.04399								
Simulation Parameters: Fixed-Slit Intensities, Two-Theta Range =24.11/150.31/0.02, FWHM = 0.1														



3914990606

(La_{0.9}Sr_{0.1}) ((Ga_{0.8}Mg_{0.2}) O_{2.87}) PDF#89-6965

PDF#89-6965: QM=Calculated(C); d=Calculated; I=Calculated											PDF Card		
Lanthanum Strontium Gallium Magnesium Oxide (La _{0.9} Sr _{0.1}) ((Ga _{0.8} Mg _{0.2}) O _{2.87})													
Radiation=CuKα1				Lambda=1.54060				Filter=					
Calibration=				2θ=19.627-89.455				I/Ic(RIR)=4.29					
Ref: Calculated from ICSD using POWD-12++													
Monoclinic - Powder Diffraction, I2/a (15)							Z=4		mp=				
CELL: 7.81603 x 5.5883 x 5.51467 <90.0 x 90.06 x 90.0>							P.S=mC19.48 (?)						
Density(c)=6.685		Density(m)=6.44A		Mwt=240.33		Vol=238.76		F(30)=28.5(0.140,75/0)					
Ref: Slater, P.R., Irvine, J.T.S., Ishihara, T., Takita, Y. J. Solid State Chem., v139 p135 (1998)													
FIZ=051040: ICSD SG: I12/A1 IT is: 15 SG short form: I2/a ATF TEM 298. RVP. ITF TF are of mixed type. TF are converted prior to pattern calculation. ITF High-temperature powder neutron diffraction study of the oxide ion conductor Li _{0.9} Sr _{0.1} Ga _{0.8} Mg _{0.2} O _{2.85}													
Strong Lines: 2.76/X 1.95/3 1.59/2 1.60/2 3.91/2 2.25/1 2.26/1 1.38/1 1.24/1 1.23/1													
64 Lines, Wavelength to Compute Theta = 1.54056Å(Cu), I%-Type = Peak Height													
#	d(nm)	I(f)	(h k l)	2-Theta	Theta	1/(2d)	#	d(nm)	I(f)	(h k l)	2-Theta	Theta	1/(2d)
1	0.45194	0.1	(1 1 0)	19.627	9.813	0.01106	33	0.13237	0.1	(-1 4 1)	71.172	35.586	0.03777
2	0.39081	16.1	(2 0 0)	22.734	11.367	0.01279	34	0.13237	0.1	(1 4 1)	71.172	35.586	0.03777
3	0.39081	16.1	(0 1 1)	22.734	11.367	0.01279	35	0.13217	0.1	(-5 1 2)	71.295	35.648	0.03783
4	0.27645	100.0	(2 1 1)	32.358	16.179	0.01809	36	0.13217	0.1	(3 3 2)	71.295	35.648	0.03783
5	0.27645	100.0	(-2 1 1)	32.358	16.179	0.01809	37	0.13201	0.1	(3 2 3)	71.394	35.697	0.03788
6	0.27573	78.9	(0 0 2)	32.444	16.222	0.01813	38	0.13201	0.1	(5 1 2)	71.394	35.697	0.03788
7	0.23576	0.6	(3 1 0)	38.140	19.070	0.02121	39	0.13184	0.1	(1 1 4)	71.497	35.749	0.03792
8	0.23576	0.6	(1 2 1)	38.140	19.070	0.02121	40	0.13042	0.8	(4 3 1)	72.401	36.201	0.03834
9	0.23532	0.5	(-1 1 2)	38.214	19.107	0.02125	41	0.13042	0.8	(-4 3 1)	72.401	36.201	0.03834
10	0.23532	0.5	(1 1 2)	38.214	19.107	0.02125	42	0.13027	0.9	(0 3 3)	72.497	36.249	0.03838
11	0.22597	8.7	(2 2 0)	39.861	19.930	0.02213	43	0.13027	0.9	(-4 1 3)	72.497	36.249	0.03838
12	0.22519	10.7	(2 0 2)	40.005	20.002	0.02220	44	0.13008	0.9	(2 0 4)	72.623	36.312	0.03844
13	0.22519	10.7	(-2 0 2)	40.005	20.002	0.02220	45	0.13008	0.9	(4 1 3)	72.623	36.312	0.03844
14	0.19541	33.7	(4 0 0)	46.431	23.216	0.02559	46	0.12361	8.0	(6 1 1)	77.091	38.546	0.04045
15	0.19541	33.7	(0 2 2)	46.431	23.216	0.02559	47	0.12361	8.0	(-2 3 3)	77.091	38.546	0.04045
16	0.17970	0.1	(1 3 0)	50.764	25.382	0.02782	48	0.12342	4.7	(0 2 4)	77.233	38.617	0.04051
17	0.17910	0.1	(3 2 1)	50.944	25.472	0.02792	49	0.11931	0.1	(3 4 1)	80.426	40.213	0.04191
18	0.17910	0.1	(3 1 2)	50.944	25.472	0.02792	50	0.11931	0.1	(5 3 0)	80.426	40.213	0.04191
19	0.17472	3.5	(4 1 1)	52.318	26.159	0.02862	51	0.11896	0.1	(3 1 4)	80.707	40.353	0.04203
20	0.17472	3.5	(2 2 2)	52.318	26.159	0.02862	52	0.11896	0.1	(-3 1 4)	80.707	40.353	0.04203
21	0.17447	2.4	(0 1 3)	52.400	26.200	0.02866	53	0.11796	0.8	(2 4 2)	81.535	40.767	0.04239
22	0.15977	17.8	(4 2 0)	57.649	28.825	0.03130	54	0.11796	0.8	(-2 4 2)	81.535	40.767	0.04239
23	0.15977	17.8	(2 3 1)	57.649	28.825	0.03130	55	0.11788	0.7	(-6 0 2)	81.604	40.802	0.04242
24	0.15925	23.3	(2 1 3)	57.852	28.926	0.03140	56	0.11788	0.7	(6 2 0)	81.604	40.802	0.04242
25	0.15925	23.3	(4 0 2)	57.852	28.926	0.03140	57	0.11766	1.1	(-2 2 4)	81.789	40.894	0.04250
26	0.15044	0.1	(5 1 0)	61.594	30.797	0.03323	58	0.11766	1.1	(2 2 4)	81.789	40.894	0.04250
27	0.15044	0.1	(-1 2 3)	61.594	30.797	0.03323	59	0.11299	1.9	(4 4 0)	85.962	42.981	0.04425
28	0.15028	0.1	(1 2 3)	61.672	30.836	0.03327	60	0.11271	2.0	(-4 0 4)	86.227	43.114	0.04436
29	0.13848	3.0	(0 4 0)	67.591	33.796	0.03611	61	0.11259	1.3	(4 0 4)	86.333	43.167	0.04441
30	0.13812	8.6	(4 2 2)	67.792	33.896	0.03620	62	0.10969	0.1	(1 5 0)	89.213	44.606	0.04558
31	0.13812	8.6	(-4 2 2)	67.792	33.896	0.03620	63	0.10946	0.1	(1 3 4)	89.455	44.727	0.04568
32	0.13787	6.4	(0 0 4)	67.934	33.967	0.03627	64	0.10946	0.1	(7 1 0)	89.455	44.727	0.04568
Simulation Parameters: Fixed-Slit Intensities, Two-Theta Range =17.63/91.45/0.02, FWHM = 0.1													



3914990606

SrLaGa₃O₇ PDF#45-0637

PDF#45-0637: QM=Star(S); d=Diffraction; I=Diffraction											PDF Card			
Strontium Lanthanum Gallium Oxide														
Sr La Ga ₃ O ₇														
Radiation=CuKa1			Lambda=1.54056			Filter=Ni								
Calibration=External(Al2O3)			2T=15.540-110.206			I/c(RIR)=7.21								
Ref: Ivanov, S., Zhurov, V., Karpov Inst. of Physical Chemistry, Moscow, Russia.														
ICDD Grant-In-Aid (1994)														
Tetragonal - Powder Diffraction, P-421m (113)						Z=2		mp=						
CELL: 8.0541 x 8.0541 x 5.3325 <90.0 x 90.0 x 90.0>						P.S=tP24 (?)								
Density(c)=5.290		Density(m)=5.240		Mwt=547.68		Vol=345.91		F(30)=298.9(.0030,33/0)						
Ref: Toropov, N., Ismatov, A.														
Dokl. Akad. Nauk SSSR, v183 p609 (1968)														
NOTE: EDS analysis (LINK system) (at.%): Sr 20.1(3), La 19.8(2), Ga 60.1(5). Sample was provided by Kucheiko, S., Moscow State Univ., Russia. Pattern taken at 22 C. Single-crystals of Sr La Ga ₃ O ₇ were grown by Czochralski method. To replace 22-1436.														
Color: Colorless														
Strong Lines: 2.98/X 1.84/3 2.55/2 3.21/2 1.59/2 2.67/1 3.89/1 1.44/1 1.83/1 1.55/1														
101 Lines, Wavelength to Compute Theta = 1.54056A(Cu), I%-Type = Peak Area														
#	d(nm)	I(f)	(hkl)	2-Theta	#	d(nm)	I(f)	(hkl)	2-Theta	#	d(nm)	I(f)	(hkl)	2-Theta
1	0.56975	3.0	(110)	15.540	35	0.15941	15.0	(213)	57.791	69	0.11488	0.0	(622)	84.208
2	0.53334	1.0	(001)	16.608	36	0.15761	2.0	(412)	58.515	70	0.11443	5.0	(523)	84.618
3	0.44469	1.0	(101)	19.950	37	0.15464	7.0	(332)	59.751	71	0.11377	1.0	(542)	85.224
4	0.40264	2.0	(200)	22.058	38	0.15145	2.0	(511)	61.144	72	0.11169	1.0	(640)	87.210
5	0.38930	12.0	(111)	22.824	39	0.15079	2.0	(223)	61.437	73	0.11117	1.0	(404)	87.723
6	0.36023	1.0	(210)	24.694	40	0.14923	2.0	(422)	62.150	74	0.11063	0.0	(720)	88.262
7	0.32137	18.0	(201)	27.736	41	0.14822	1.0	(303)	62.621	75	0.11012	1.0	(414)	88.770
8	0.29848	100.0	(211)	29.911	42	0.14577	1.0	(313)	63.798	76	0.10933	1.0	(641)	89.586
9	0.28474	4.0	(220)	31.390	43	0.14401	10.0	(521)	64.674	77	0.10909	1.0	(334)	89.832
10	0.26665	14.0	(002)	33.581	44	0.14238	2.0	(440)	65.502	78	0.10832	1.0	(721)	90.651
11	0.25471	22.0	(310)	35.206	45	0.13909	1.0	(323)	67.258	79	0.10715	1.0	(424)	91.924
12	0.25309	3.0	(102)	35.438	46	0.13814	1.0	(530)	67.783	80	0.10619	1.0	(613)	93.004
13	0.25120	1.0	(221)	35.714	47	0.13788	1.0	(432)	67.926	81	0.10576	2.0	(730)	93.494
14	0.24147	2.0	(112)	37.204	48	0.13756	1.0	(441)	68.107	82	0.10482	1.0	(115)	94.590
15	0.23976	1.0	(301)	37.479	49	0.13589	0.0	(512)	69.059	83	0.10476	0.0	(712)	94.667
16	0.22987	1.0	(311)	39.156	50	0.13421	4.0	(600)	70.050	84	0.10351	1.0	(623)	96.175
17	0.22230	2.0	(202)	40.547	51	0.13333	3.0	(004)	70.583	85	0.10307	1.0	(205)	96.715
18	0.21431	5.0	(212)	42.129	52	0.13240	0.0	(610)	71.150	86	0.10269	2.0	(543)	97.202
19	0.20605	2.0	(321)	43.905	53	0.13147	4.0	(413)	71.732	87	0.10226	3.0	(215)	97.752
20	0.20133	5.0	(400)	44.989	54	0.13044	1.0	(522)	72.387	88	0.10125	0.0	(651)	99.066
21	0.19534	3.0	(410)	46.449	55	0.12977	2.0	(333)	72.821	89	0.09989	1.0	(740)	100.914
22	0.19465	3.0	(222)	46.623	56	0.12850	1.0	(611)	73.659	90	0.09989	1.0	(225)	100.914
23	0.18985	5.0	(330)	47.875	57	0.12652	0.0	(423)	75.008	91	0.09952	0.0	(524)	101.425
24	0.18922	1.0	(302)	48.043	58	0.12580	0.0	(540)	75.509	92	0.09892	1.0	(801)	102.279
25	0.18837	1.0	(401)	48.275	59	0.12559	1.0	(442)	75.663	93	0.09832	2.0	(732)	103.154
26	0.18417	25.0	(312)	49.447	60	0.12502	1.0	(214)	76.065	94	0.09819	3.0	(811)	103.338
27	0.18342	9.0	(411)	49.662	61	0.12386	1.0	(621)	76.911	95	0.09732	1.0	(444)	104.651
28	0.18010	3.0	(420)	50.643	62	0.12265	1.0	(532)	77.809	96	0.09592	1.0	(534)	106.845
29	0.17884	4.0	(331)	51.026	63	0.12242	2.0	(541)	77.983	97	0.09490	1.0	(660)	108.524
30	0.17121	1.0	(322)	53.474	64	0.12073	1.0	(224)	79.287	98	0.09458	2.0	(643)	109.067
31	0.17064	0.0	(421)	53.667	65	0.11990	3.0	(602)	79.944	99	0.09458	2.0	(604)	109.067
32	0.16969	1.0	(113)	53.993	66	0.11940	1.0	(304)	80.351	100	0.09423	1.0	(405)	109.652
33	0.16262	2.0	(203)	56.544	67	0.11864	0.0	(612)	80.969	101	0.09392	0.0	(723)	110.206
34	0.16068	2.0	(402)	57.290	68	0.11810	6.0	(314)	81.416					
Simulation Parameters: Fixed-Slit Intensities, Two-Theta Range =13.54/112.21/0.02, FWHM = 0.1														



3914990606

VITA

Miss Ratanakorn Teerasarunyanon was born on January 16, 1989 in Nakorn Pathom, Thailand. She graduated with Bachelor's Degree in Chemistry (2nd class honor) from Faculty of Science, Silpakorn University in 2010. She continued the Master's degree in program of Chemistry (Inorganic Chemistry), Faculty of Science, Chulalongkorn University in 2011 and completed in 2013.

PRESENTATIONS

October 21-23, 2013.

Poster Presentation: "Effects of Calcium Doping on Electrical Properties of $\text{La}_{1.6}\text{Sr}_{0.4}\text{Ni}_{0.9}\text{Co}_{0.1}\text{O}_4$ Materials for SOFCs" The 9th congress on science and technology of Thailand (STT39), BITEC Bangna, Bangkok, Thailand.

January 8-10, 2014.

Poster Presentation: "Electrical Conductivity of $\text{La}_{1.6}\text{Sr}_{0.4}\text{Ni}_{0.9}\text{Co}_{0.1}\text{O}_4$ Oxide Doped with Calcium" The 9th Mathematics and Physical Science Graduate Congress at University of Malaya, Malaysia.

Her present address is 44 M.1, Thaplaung sub-district, Muang district, Nakorn Pathom, Thailand 73000. Tel: "+66 81 010 100" E-mail: ratanakornt@gmail.com



